Study of the Υ resonances with the CMS detector

By

Guillermo Breto Rangel

B.S.(Universidad de la Habana, Cuba) 1996

M.S.(San Francisco State University, San Francisco) 2008

DISSERTATION

Submitted in partial satisfaction of the requirements for the degree of

Doctor of Philosophy

in

Physics

in the

OFFICE OF GRADUATE STUDIES

of the

UNIVERSITY OF CALIFORNIA

Davis

Committee in Charge:

Ramona Vogt, Ph. D.

Daniel Cebra, Ph. D.

Manuel Calderón de la Barca Sánchez, Committee Chairperson

2014

ProQuest LLC.
789 East Eisenhower Parkway
P.O. Box 1346
Ann Arbor, MI 48106 - 1346

Abstract

Study of the Υ resonances with the CMS detector

Guillermo Breto Rangel

The present work focuses on detailed studies of the $\Upsilon(n\mathrm{S})$ resonances in lead - lead (PbPb) collisions with the CMS detector. The suppression of the $\Upsilon(3\mathrm{S})$ and $\Upsilon(2\mathrm{S})$ excited states in PbPb collisions, relative to the ground $1S$ state (single ratio) as well as relative to the same ratio in the proton - proton (pp) environment, known as the double ratio, is extensively studied. The study of both single and double ratios is of vital importance because it helps us quantify the suppression of the Υ states which in turn might be indicative of the formation of the Quark-Gluon plasma (QGP) according to several theoretical models. Based on a PbPb dataset of 150 μb^{-1}, the measured double ratio $\Upsilon(2\mathrm{S})/\Upsilon(1\mathrm{S})$ in PbPb relative to pp collisions is found to be $0.21 \pm 0.07\,(\mathrm{stat.}) \pm 0.02\,(\mathrm{syst.})$. No noticeable dependencies are observed on the dimuon rapidity or transverse momentum, within the current statistical precision. No clear centrality dependence of the double ratios can be inferred from the data, while such a dependence is observed when inspecting the individual $\Upsilon(1\mathrm{S})$ and $\Upsilon(2\mathrm{S})$ nuclear modification factors, R_{AA}. The centrality-integrated R_{AA} values for the $\Upsilon(1\mathrm{S})$ and $\Upsilon(2\mathrm{S})$ states are $0.56 \pm 0.08\,(\mathrm{stat.}) \pm 0.07\,(\mathrm{syst.})$ and $0.12 \pm 0.04\,(\mathrm{stat.}) \pm 0.02\,(\mathrm{syst.})$, respectively. The 3S state is not observed prominently in the data, and upper limits on its suppression ratios are set. From the nuclear modification factor R_{AA} for the $\Upsilon(1\mathrm{S})$ a measurement of the initial temperature of the plasma in its most central region yielded a value of $T_0^{central} = 0.56 \pm 0.03\,(\mathrm{syst.})$ GeV which is expected to be above the transition to QGP based on Lattice studies.

Manuel Calderón de la Barca Sánchez

Dissertation Committee Chair

Contents

List of Figures

List of Tables

Chapter 1

Introduction

Bayesians are like Vegans, at some point they become impractical.

Meetup in the Silicon Valley

Quarkonia, bound states of a heavy quark and its antiquark, are very different kinds of hadrons. For the ground state, J/ψ and Υ, the binding energies are around 0.6 and 1.2 GeV, respectively, and thus much larger than the typical hadronic scale $\Lambda \sim 0.2$ GeV; as a consequence, they are also much smaller, with radii of about 0.1 and 0.2 fm. At high temperatures, strongly-interacting matter undergoes a "deconfining" phase transition to a quark-gluon plasma (QGP). This transition is triggered by a rapid increase of the energy and entropy densities as well as the disappearance of hadronic states [1]. According to current lattice calculations at zero net-baryon density, deconfinement occurs at $T_c \sim 165 - 195$ MeV [2, 3, 4, 5, 6, 7, 8, 9, 10, 11] . The QGP is characterized by color screening: the range of interaction between heavy quarks becomes inversely proportional to the temperature. However, given quarkonia much smaller radii in comparison to other hadronic states, it is expected that they can survive in a QGP through some range of temperatures above the critical transition temperature (T_c). Eventually at sufficiently high temperatures it is impossible to produce a bound state between a heavy quark (c or b) and its antiquark.

Since deconfinement is related to colour screening, the critical quantity for dissociation of a bound state is the relation of binding to Debye screening radius. Moreover, the higher excited quarkonium states are less tightly bound and hence larger. We therefore expect that the different quarkonium states have different "dissociation temperatures" in a quark-gluon plasma [12].Hence the spectral analysis of in-medium quarkonium dissociation should provide a QGP thermometer. This hierarchy in dissociation temperatures will be studied in this thesis. In particular, the Υ in heavy-ion collisions was suggested to be a theoretically and experimentally cleaner probe of the deconfined medium due to the larger mass of the bottom quark. For the bottomonium the effects of initial state nuclear suppression are expected to be reduced. Moreover, heavier quarks allow for cleaner theoretical treatments based on potential models because these models rely on taking the non-relativistic limit and the heavier the quark the more reliable the treatment is. Furthermore, since bottom $b\bar{b}$ pair production is relatively rare within the plasma, the probability for regeneration of bottomonium states through recombination is much smaller than for charm quarks.

The study of bottomonium states is of extreme importance in the field of Heavy-Ion Physics.

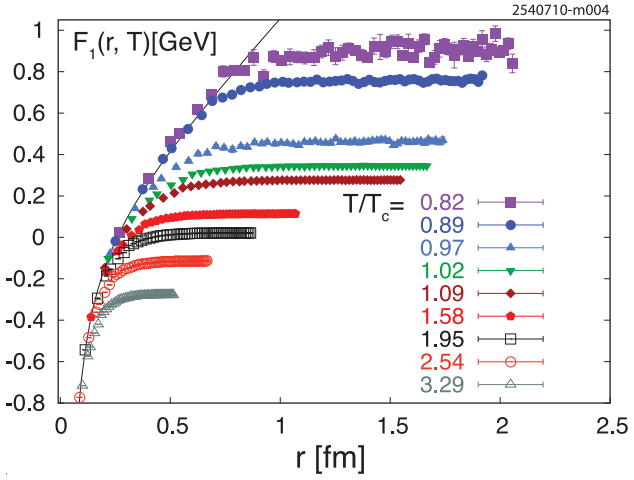

Figure 1.1: Heavy-quark-singlet free energy versus quark separation calculated in 2+1 flavor QCD on $16^3 \times 4$ lattices at different temperatures [14, 22]

1.1 Quantum Chromodynamics on the lattice

The study of the fundamental theory of the strong interaction — Quantum Chromodynamics (QCD) — in extreme conditions of temperature, density and parton momentum fraction (low-x) has attracted increasing experimental and theoretical interest during the last 20 years. Indeed, QCD is not only a quantum field theory with an extremely rich dynamical content — such as asymptotic freedom, infrared slavery, (approximate) chiral symmetry, non-trivial vacuum topology, strong CP violation problem, $U_A(1)$ axial-vector anomaly, color superconductivity, ... — but also the only sector of the Standard Model (SM) whose full *collective* behaviour — phase diagram, phase transitions, thermalisation of fundamental fields — is accessible to scrutiny in the laboratory.

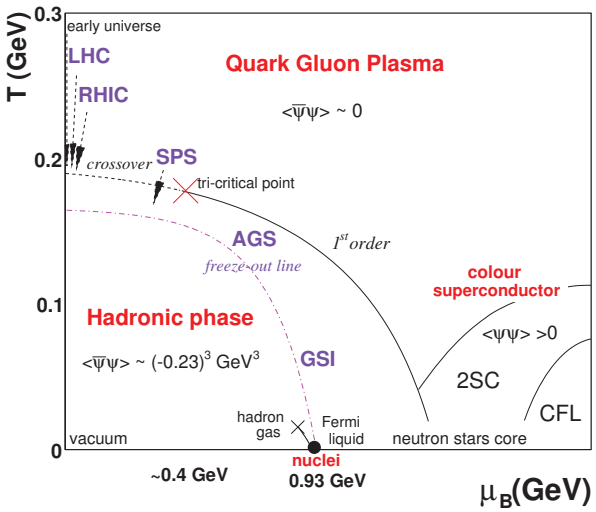

Figure 1.2: QCD phase diagram.Temperature, T, vs Baryon Chemical Potential μ_B

Lattice QCD calculations predict a new form of matter at energy densities (well) above a critical value — $\epsilon_c = (6 \pm 2)T_c^4 \approx 1$ GeV/fm^3 (Fig. 1.3), where $T_c \approx 150$–190 MeV is the critical temperature — consisting of an extended volume of deconfined and current-mass quarks and gluons: the Quark-Gluon Plasma (QGP).

The vanishing of the chiral condensate at T_c and the sudden liberation of quark and gluon degrees of freedom are clearly visible in Fig. 1.3. The scrutiny of this new state of matter — equation-

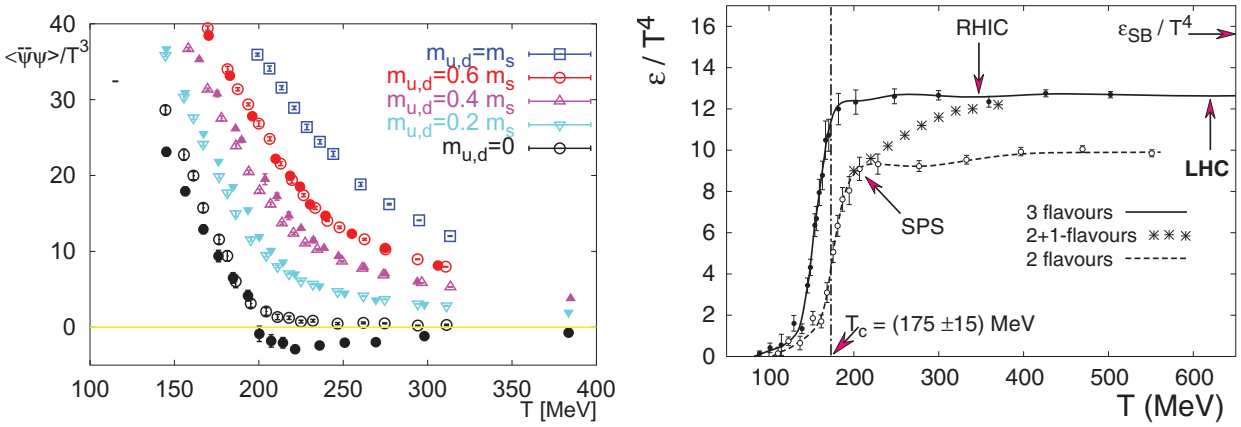

Figure 1.3: Left: The light quark chiral condensate versus the temperature computed in lattice QCD with various number of flavours and values of the u, d, s quark masses. Right: The energy density in QCD with 0, 2 and 3 degenerate quark flavours as well as with two light quarks and one heavier (strange) quarks. The horizontal arrow shows the value of the Stefan-Boltzmann limit for an ideal quark-gluon gas.

of-state (EoS), order of the phase transition, transport properties, etc. — promises to shed light on basic aspects of the strong interaction such as the nature of confinement, the mechanism of mass generation (chiral symmetry breaking, structure of the QCD vacuum) and hadronization, which still evade a thorough theoretical description due to their highly non-perturbative nature.

In order to calculate physical observables from first principles in QCD it is not enough to know the Lagrangian. It is also necessary and important to know the true structure of its ground state. It is just the response of the true QCD vacuum which substantially modifies all the QCD Greens functions from their free counterparts.

In particular, color screening is studied on the lattice by calculating the spatial correlation function of a static quark and antiquark in a color-singlet state which propagates in Euclidean time from $\tau = 0$ to $\tau = 1/T$, where T is the temperature (see [15, 16] for reviews). Lattice calculations of this quantity with dynamical quarks have been reported [17, 18, 19, 20, 21, 22]. The logarithm of the singlet correlation function, also called the singlet free energy, is shown in Fig. 1.1. As expected, in the zero-temperature limit the singlet free energy coincides with the zero-temperature potential. Fig. 1.1 also illustrates that, at sufficiently short distances, the singlet free energy is temperature independent

and equal to the zero-temperature potential. The range of interaction decreases with increasing temperature. For temperatures above the transition temperature, T_c, the heavy-quark interaction range becomes comparable to the bottomonium radius. Again, based on this general observation, one would expect that the bottomonium states not to remain bound at temperatures just above the deconfinement transition.

1.1.1 Cold-nuclear-matter effects

The baseline for quarkonium production and suppression in heavy-ion collisions should be determined from studies of cold-nuclear-matter (CNM) effects. The name cold matter arises because these effects are observed in hadron-nucleus interactions where no hot, dense matter effects are expected. There are several CNM effects. Modifications of the parton distribution functions in the nucleus, relative to the nucleon, (i.e. *shadowing*) and energy loss of the parton traversing the nucleus before the hard scattering are both assumed to be initial-state effects, intrinsic to the nuclear target. Another CNM effect is absorption (i.e. destruction) of the quarkonium state as it passes through the nucleus. Since the latter occurs after the $Q\overline{Q}$ pair has been produced and while it is traversing the nuclear medium, this absorption is typically referred to as a final-state effect. In order to disentangle the mechanisms affecting the produced $Q\overline{Q}$, data from a variety of center-of-mass energies and different phase-space windows need to be studied.

In addition, the inclusive J/ψ yield includes contributions from χ_c and $\psi^{'}$ decays to J/ψ at the 30-35% level [23]. While there is some information on the A dependence of $\psi^{'}$ production, that on χ_c is largely unknown [24].

Even though the contributions to CNM effects may seem rather straightforward, there are a number of associated uncertainties. First, while nuclear modifications of the quark densities are relatively well-measured in nuclear deep-inelastic scattering (nDIS), the modifications of the gluon density are not directly measured. The nDIS measurements probe only the quark and antiquark

distributions directly. The scaling violations in nDIS can be used to constrain the nuclear gluon density. Overall momentum conservation provides another constraint. However, more direct probes of the gluon density are needed. Current shadowing parametrizations are derived from global fits to the nuclear parton densities and give wide variations in the nuclear gluon density, from almost no effect to very large shadowing at low-x, compensated by strong antishadowing around $x \sim 0.1$. The range of the possible shadowing effects is illustrated in Fig. 1.4 by the new EPS09 [25] parametrization and its associated uncertainties, employing the scale values used to fix the J/ψ and Υ cross sections below the open-heavy-flavor threshold [26].

Quarkonium spectral functions and quarkonium potential

In-medium quarkonium properties are encoded in the corresponding spectral functions, as is quarkonium dissolution at high temperatures. Spectral functions are defined as the imaginary part of the retarded correlation function of quarkonium operators. Bound states appear as peaks in the spectral functions. The peaks broaden and eventually disappear with increasing temperature. The disappearance of a peak signals the melting of the given quarkonium state.

The quarkonium spectral functions can be calculated in potential models using the singlet free energy from Fig. 1.1 or with different lattice-based potentials obtained using the singlet free energy as

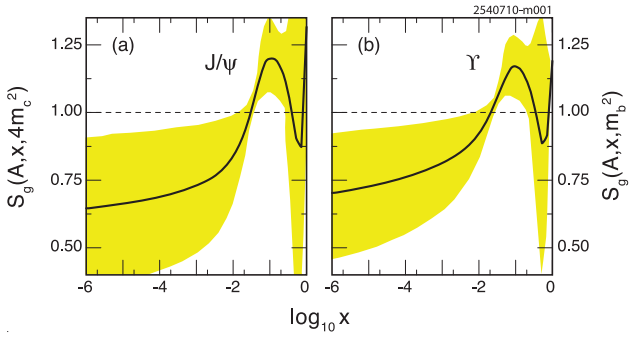

Figure 1.4: The EPS09 gluon-shadowing parametrization [25] at $Q = 2m_c$ and m_b. The central value *(solid curves)* and the associated uncertainty *(shaded band)* are shown

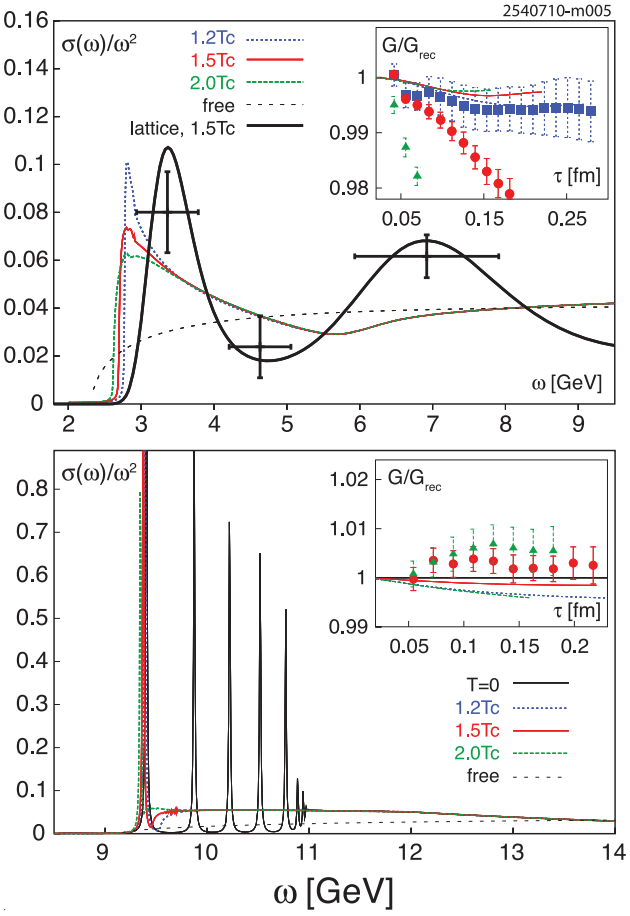

Figure 1.5: The S-wave charmonium (upper) and bottomonium (lower) spectral functions calculated in potential models. Insets: correlators compared to lattice data. The *dotted curves* are the free spectral functions.

an input [27, 28] (see also [29] for a review). The results for quenched QCD calculations are shown in Fig. 1.5 for S-wave charmonium (top) and bottomonium (bottom) spectral functions [27]. All charmonium states are dissolved in the deconfined phase while the bottomonium 1S state may persist up to $T \sim 2T_c$.

Potential model calculations based on lattice QCD, as well as resummed perturbative QCD calculations, indicate that all charmonium states and the excited bottomonium states dissolve in the deconfined medium. This leads to the reduction of the quarkonium yields in heavy-ion collisions compared to the binary scaling of pp collisions. Recombination and edge effects, however, guarantee a nonzero yield.

1.2 Bottomonium

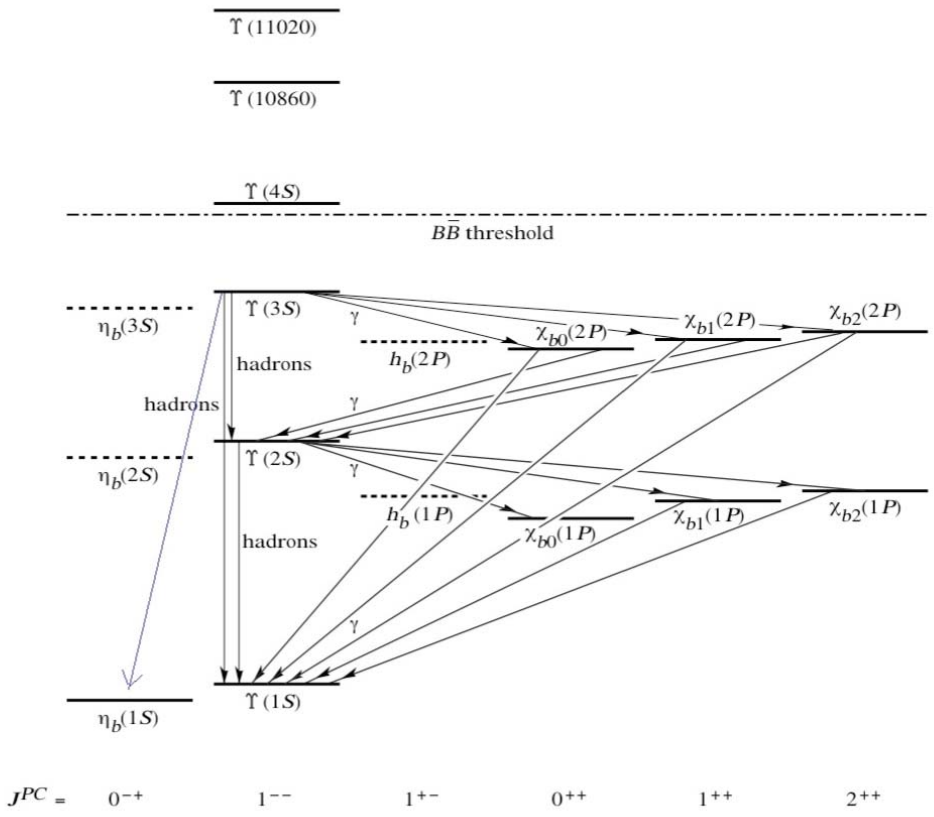

Figure 1.6: The bottomonium family.

As previously mentioned, if a deconfined medium is formed in high-energy heavy-ion collisions, one of its most striking expected characteristics is the suppression of quarkonium states. This takes place as the force between the constituents of the quarkonium state, a heavy quark and its antiquark, is weakened by the color screening produced by the surrounding light quarks and gluons.

The suppression is predicted to occur above a critical temperature of the medium, and sequentially, in the order of the $Q\overline{Q}$ binding energy. Since the Υ(1S) is the most tightly bound state among all quarkonia, it is expected to be the one with the highest dissociation temperature. Such a suppression pattern is expected to further depend on complications arising from additional *hot* and

cold nuclear matter effects phenomena as mentioned before. The work presented here aims at studying in detail the bottomonium family (see fig 1.6) of states in ultra-relativistic heavy-ion collisions. Given the momentum resolution attained, and the capability of the trigger system, CMS is unrivaled in the analysis of the Υ family in the three environements studied (pp, pPb and PbPb), although the work here does not include results in the pPb environment.

Chapter 2

Theoretical Models

In the literature, there are many models which attempt to explain the suppresion of quarkonium states in heavy-ion collisions. Charm and bottom quarks are particularly interesting because, due to their heavy masses, their spectrum of low lying states can be found using potential-based non-relativistic treatments [30]. In early experiments J/ψ was the quarkonium of choice given that the Υ was not as abundant. More recently, with the increase of center of mass energy of the collisions, the Υ resonance has become more available and its study more feasible. There are many advantages to the study of bound states of bottom and anti-bottom quarks (bottomonium) mainly due to its higher mass. Bottom quarks ($m_b \simeq 4.2$ GeV) are more massive than charm quarks ($m_c \simeq 1.3$ GeV) and as a result the heavy quark effective theories underpinning phenomenological applications are on much surer footing. Due to their higher mass, the effects of initial state nuclear suppression are expected to be smaller than for the charmonium states [31]. The masses of bottomonium states ($m_\Upsilon \approx 10$ GeV) are much higher than the temperatures ($T \approx 1$ GeV) generated in relativistic heavy ion collisions. As a result, bottomonium production will be dominated by initial hard scatterings. Since bottom quarks and antiquarks are relatively rare within the plasma, the probability for regeneration of bottomonium states through recombination is much smaller than for charm quarks [32].

Based on potential models, the suppresion can be attributed both to the real and imaginary parts of the potential. In general one finds that the heavy quark potential has real and imaginary parts, $V = \Re[V] + i\Im[V]$. One can determine the real part of the heavy-quark potential in the non relativistic limit from the Fourier transform of the 00-component of the static gluon propagator [33]. If the plasma is formed, quasi-free gluons will interact with the gluons mediating the force between the quark and its antiquark and, as a consequnce, the potential will be weakened. On the other hand, the analytic form of the imaginary part comes from resummed perturbative calculations. The result has been confirmed by multiple groups [34, 35]. Physically, the imaginary part comes from decays due to either (a) a thermal particle hitting the exchanged gluon or (b) a thermal gluon hitting one of the heavy quarks. In the very heavy quark limit (a) dominates and is related to "Landau damping" of the exchange gluon. The Landau damping decay width dominates for bottomonium states. The additional imaginary-valued contribution to the potential coming from singlet to octet transitions has also been computed using the effective field theory approach [36]. These imaginary-valued contributions to the potential are related to quarkonium decay processes in the plasma.

Lattice studies have also shown the imaginary part; however, the uncertainties are too high to parameterize the results, hence resummed analytic perturbative forms are used. However, lattice results are already able to show that the perturbative calculations are not in contradiction with lattice measurements. They see the imaginary part of the binding energy increasing with temperature. Whenever the real part of the potential is of the same order as the imaginary part of the potential the resonance can no longer be considered a bound state. From the spectral function perspective, one can imagine both the height of the potential decreasing (real part) and the the width of the resonance increasing (imaginary part) until the state disappears.

Other models include a kinetic-rate equation approach in a thermally expanding medium. This approach is employed to calculate the evolution of bottomonium distributions in heavy-ion collisions.

The equilibrium properties of the quarkonia are taken from in-medium spectral functions which are schematically constrained by Euclidean correlators from lattice QCD.

Our final results will be compared to some of the theoretical models in chapter 11.5.2.

Chapter 3

Measurements

The LHC allows for the first detailed studies of the bottomonium family of states in ultra relativistic heavy-ion collisions. Given the momentum resolution attained, and the capability of the trigger system, the CMS detector is ideal for this study. The measurement of bottomonium production and suppression is presented in this thesis, based on the dataset collected by the CMS experiment during the 2011 PbPb collision run at $\sqrt{s_{NN}} = 2.76\,\text{TeV}$.

Both charmonium (J/ψ, ψ', χ_c) and bottomonium (Υ(1S), Υ(2S), Υ(3S), χ_b) production studies at the unprecedented medium created at the LHC should help us quantify the temperature of the fireball. In this thesis, the measurements of the production and suppression of the Υ(1S), Υ(2S), and Υ(3S) states are performed.

While all of charmonia as well as excited bottomonia states are expected to be suppressed in the hot and dense medium, the strongly-bound Υ(1S) state is expected to be the last to melt, or more precisely, disassociate in the QGP.

The production of Υ(nS) states is studied by comparing their production rates in PbPb and pp collision data, taken at the same collision energy of $\sqrt{s_{NN}} = 2.76$ TeV. In particular, the yield of the higher-mass states is measured relative to the ground state. In this way, we explore the double ratios – $\Upsilon(2S, 3S)$ vs Υ(1S) and PbPb *vs* *pp* – which allows for a self-calibrating measurement. Several effects

associated to selection, acceptance, and reconstruction mostly cancel, and only remaining factors need to be accounted for, as corrections to the fitted ratio of raw signal yields.

Based on the dataset collected during the first LHC PbPb run, at $\sqrt{s_{NN}} = 2.76\,\text{TeV}$, in 2010, and in the special *pp* run at the same energy in early 2011, CMS published the first results on Υ production and suppression in PbPb collisions. These included the first evidence for suppression of the excited Υ states relative to the ground state, at the $2.4\,\sigma$ level [39, 45]. Suppression of the $\Upsilon(1\text{S})$ state, relative to *pp* collisions scaled by the number of binary nucleon-nucleon collisions at the same energy, has also been measured [**?**]. These two measurements were found to be consistent with suppression of only the excited states, which result in reduced feeddown from excited to ground states. These main results may be summarized as follows:

$$
\begin{aligned}
\Upsilon(2S+3S)/\Upsilon(1\text{S})|_{\text{PbPb}} &= 0.24^{+0.13}_{-0.12} \pm 0.02\,, \\
\Upsilon(2S+3S)/\Upsilon(1\text{S})|_{pp} &= 0.78^{+0.16}_{-0.14} \pm 0.02\,, \\
(\chi \equiv) \frac{\Upsilon(2S+3S)/\Upsilon(1\text{S})|_{\text{PbPb}}}{\Upsilon(2S+3S)/\Upsilon(1\text{S})|_{pp}} &= 0.31^{+0.19}_{-0.15} \pm 0.03\,, \\
\frac{\Upsilon(1\text{S})|_{\text{PbPb};\,0-20\%}}{\Upsilon(1\text{S})|_{pp}} &= 0.681 \pm 0.143 \pm 0.119\,.
\end{aligned}
$$

In the 2011 PbPb run, CMS collected a dataset approximately 20 times larger than that gathered in 2010. The quest for better data analyses will continue during the ensuing few years of data taking, in order to extract further novel and precise results. Before we go any further, let's begin by describing the CMS detector capabilities.

Chapter 4

Triggering on hard probes

4.1 Introduction

The central feature of the CMS detector is a superconducting solenoid of $6m$ internal diameter, providing a magnetic field of 3.8T. Within the field volume are the silicon pixel and strip tracker, the crystal electromagnetic calorimeter, and the brass/scintillator hadron calorimeter.

Muons are detected in the range $|\eta| < 2.4$, with detection planes based on three technologies: drift tubes, cathode strip chambers, and resistive plate chambers. Because of the strong magnetic field and the fine granularity of the tracker, the muon p_{T} measurement based on information from the tracker alone has a resolution between 1 and 2% for a typical muon in this analysis.

Quarkonia are identified through their dimuon decay. The silicon pixel and strip tracker measures charged-particle trajectories for the range $|\eta| < 2.5$. The tracker consists of 66M pixel and 10M strip detector channels, providing a vertex resolution of ~ 15 μm in the transverse plane. Muons are detected for the $|\eta| < 2.4$ range, with detection planes based on three technologies: drift tubes (DT), cathode strip chambers (CSC), and resistive plate chambers (RPC). CMS is therefore very well suited to measure dimuons. In pp, the mass resolution obtained measuring Υ(1S) in $|y| < 0.5$ is 67 MeV/c^2

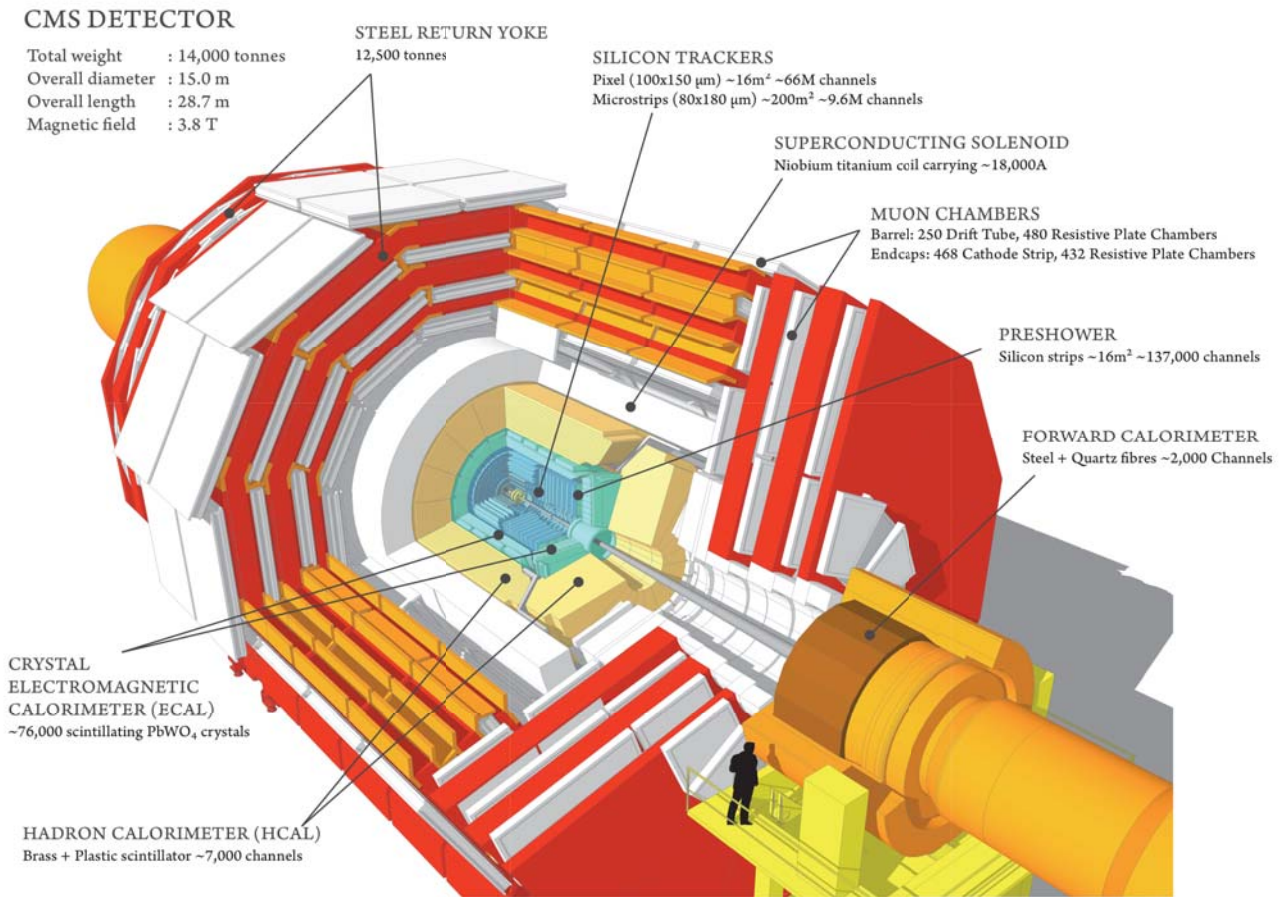

Figure 4.1: Sectional view of the CMS detector. The LHC beams travel in opposite directions along the central axis of the CMS cylinder colliding in the middle of the CMS detector.

for $|\eta^{\mu}| < 1$. Since the mass difference between the 2S and 3S states is $\sim$ several hundred MeV/c^2, with a resolution below 100 MeV/c^2 we can easily separate all three states.

The layout of one quarter of the CMS muon system is shown in (Fig. 4.1). In the Muon Barrel (MB) region, four stations of detectors are arranged in cylinders interleaved with the iron yoke. The segmentation along the beam direction follows the five wheels of the yoke. In each of the endcaps, the CSCs and RPCs are arranged in four disks perpendicular to the beam, and in concentric rings, three rings in the innermost station, and two in the others. In total, the muon system contains of order 25000 m^2 of active detection planes, and nearly 1 million electronic channels.

Muons are reconstructed by matching tracks in the muon detectors and silicon tracker. The same offline reconstruction algorithm and selection criteria are applied to the *PbPb* and *pp* data samples.

The muon candidates are required to have a transverse (longitudinal) distance of closest approach to the event vertex smaller than 3 (15)cm. Muons are only kept if the part of their trajectory in the tracker has 11 or more hits and the χ^2 per degree of freedom of the combined and tracker-only fits are lower than 20 and 4, respectively. Pairs of oppositely charged muons are considered dimuon candidates if the χ^2 fit probability of the tracks originating from a common vertex exceeds 5%. This removes background arising primarily from the displaced, semileptonic decays of charm and bottom hadrons.

Only muons with $p_T > 4$ GeV/c and $|\eta| < 2.4$ are considered, as in Ref. [39]. The dimuon p_{T} distribution of the selected candidates extends down to zero and has a mean of about 6 GeV/c, covering a dimuon rapidity range of $|y| < 2.4$.

In order to trigger on these muons, CMS has a modular Level 1 trigger (L1) based on hardware ASICS and FPGA with constant latency of ~ 3.0 μs as well as a High Level Trigger (HLT) which is based on regional software algorithms with a latency of a few seconds.

4.2 Muon Reconstruction and Identification

In the standard CMS reconstruction, tracks are first reconstructed independently in the inner tracker (tracker track) and in the muon system (standalone-muon track). Based on these objects, two reconstruction approaches are used: *Global Muon reconstruction (outside-in)* and *Tracker Muon reconstruction (inside-out)* (Fig. 4.2).

For the former case, for each standalone-muon track, a matching tracker track is found by comparing parameters of the two tracks propagated onto a common surface. A global-muon track is fitted combining hits from the tracker track and standalone-muon track, using the Kalman-filter technique. For the latter case, all tracker tracks with $p_T > 0.5$ GeV/c and total momentum $p > 2.5$ GeV/c are considered as possible muon candidates and are extrapolated to the muon system taking

into account the magnetic field, the average expected energy losses, and multiple Coulomb scattering in the detector material, and matched to locally reconstructed segments in muon detectors.

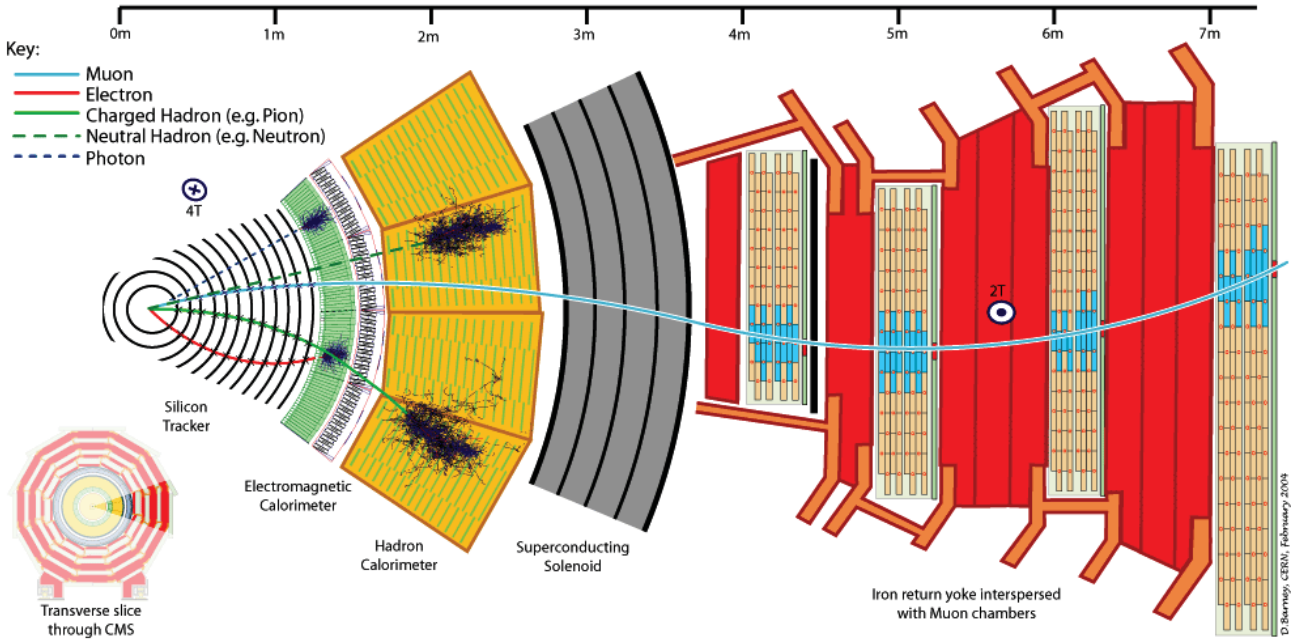

Figure 4.2: A *Global Muon* is reconstructed by combining muon objects from the muon system (standalone muon track) and objects from the inner tracker (tracker track).

The key component for exploiting the CMS capabilities in heavy-ion collisions is the trigger system, which is crucial for accessing the rare probes which yield the most direct insights into the properties of high-density strongly-interacting matter. Examples of such probes are high E_{T} jets and photons, Z^0 bosons, D and B mesons, and high-mass dileptons from quarkonia decays. The unique CMS trigger architecture employs only two trigger levels. The Level-1 trigger is implemented using custom electronics and inspects events at the full bunch crossing rate. All further online selection is performed in the High-Level Trigger (HLT) using a large cluster of commodity workstations (the "filter farm") with a vast computing power (equivalent to 12 000 1.8 GHz CPUs or ∼50 TFlops) running offline reconstruction algorithms on fully-assembled event information.

The design of the CMS trigger system is well suited to application in heavy-ion collisions. The event selection for PbPb collision events uses the Level-1 hardware trigger mainly for rejection of background and beam-gas collision candidates.

4.3 Basic constraints for triggering in heavy-ion collisions

At LHC pp design luminosity, multiple collisions will occur at each bunch crossing with a frequency of 40 MHz. The effective *pp* event output rate to mass storage is limited to 150 Hz, corresponding to an output bandwidth of 225 MByte/s.

Consequently, the trigger system in *pp* running has to select less than 10^{-5} of all collision events for permanent storage while maximising the sensitivity to new physics. The Level-1 selection reduces the event rate by a factor of 400, to 100 kHz. In *pp* running, a reduction of the event rate by a factor of more than 600 in the HLT is required to achieve the design output rate. The fact that a typical *pp* "event" at design luminosity actually consists of $\sim$ 20 superimposed *pp* collisions is also important.

Therefore, even the maximum rate for PbPb collisions is much smaller than the 100 kHz input rate for the HLT in *pp* collisions after Level-1 selection. No significant rejection of PbPb collisions has been performed at Level-1.

The possible gain in physics reach by the HLT, relative to simply collecting minimum bias events, is determined by the ratio between the collision rate and the rate of events written to mass storage. The bandwidth to mass storage of 225 MByte/s translates into an event rate of 10-100 Hz, based on estimates of the heavy-ion event size that will be discussed below. This output rate is not only limited by the available mass storage technology but also by limits on the available offline analysis resources. It is more efficient to invest resources in a high quality online trigger scheme than in offline handling and storage of poorly-selected data.

The flexibility of the HLT system will allow allocation of bandwidth not just to certain trigger channels, but differentially as a function of y and p_{T} of the trigger object, and as a function of collision centrality, thereby maximising the overall physics reach of our measurements.

The basic triggering steps in PbPb running can be summarised as follows. Every PbPb collision in our interaction region, identified by the Level-1 trigger, is sent to the HLT filter farm. In the HLT, the full event information is available for each event. All rejection of PbPb collisions is based on the outcome of HLT trigger algorithms that are identical to the corresponding offline algorithms.

The high granularity of the CMS silicon pixel tracker allows the reconstruction of a large fraction of the produced charged hadrons even in central PbPb collisions.

Muon finder timing

The muon finder consists of three different algorithms. The first part, $L1$, is executed at Level-1 for every event, producing a list of muon candidates. The Level-1 muon selection is based on the corresponding selection for pp, although the cuts have been adjusted to increase acceptance at low p_{T}. The second part of the muon finder, $L2$, is also executed on all events, this time in the HLT. The average execution times for this algorithm are 710, 100, and 10 ms for $b = 0, 9$, and 12 fm, respectively. These numbers are based on simulation Parameterising the execution time as a function of the impact parameter and averaging over all centralities yields an estimated average execution time of $\langle t \rangle = 80 \pm 20$ ms. The error is dominated by the uncertainty in the functional form of the impact parameter dependence, due to the small number of points. Correspondingly, $L2$ execution uses 1 to 5% of the HLT CPU budget, depending on event rate.

The third part of the algorithm, $L3$, is run in the HLT on events with at least two muon candidates found by either $L1$ or $L2$. The $L3$ algorithm extends the tracks found in the muon system to the silicon tracker and provides a significant improvement in momentum resolution and background rejection. This is particularly important for low p_{T} dimuons, which are expected to take up the largest

fraction of the output bandwidth to tape. Averaged over impact parameter, $L3$ will only be called for $2 \pm 1\%$ of all events. However, as $L3$ requires tracking in the silicon detector, its execution time is significantly longer than for the other algorithms mentioned here and shows a very steep dependence on multiplicity. The $L3$ execution time is found to be linear in the number of muon candidates from $L2$. Averaging over the impact parameter distribution of inputs selected by $L2$, we find an execution time for the $L3$ selection of 700 ± 200 ms per $L2$ accepted event, corresponding to about 10 ± 3 s per minimum bias event.

In summary, thanks to the flexibility of the muon triggering system along with its fast, robust and modular design the detection of the dimuons which form the quarkonium state is feasible. The figure (Fig. 4.3) shows a real reconstructed Υ event during a PbPb collision detected by the CMS triggering system.

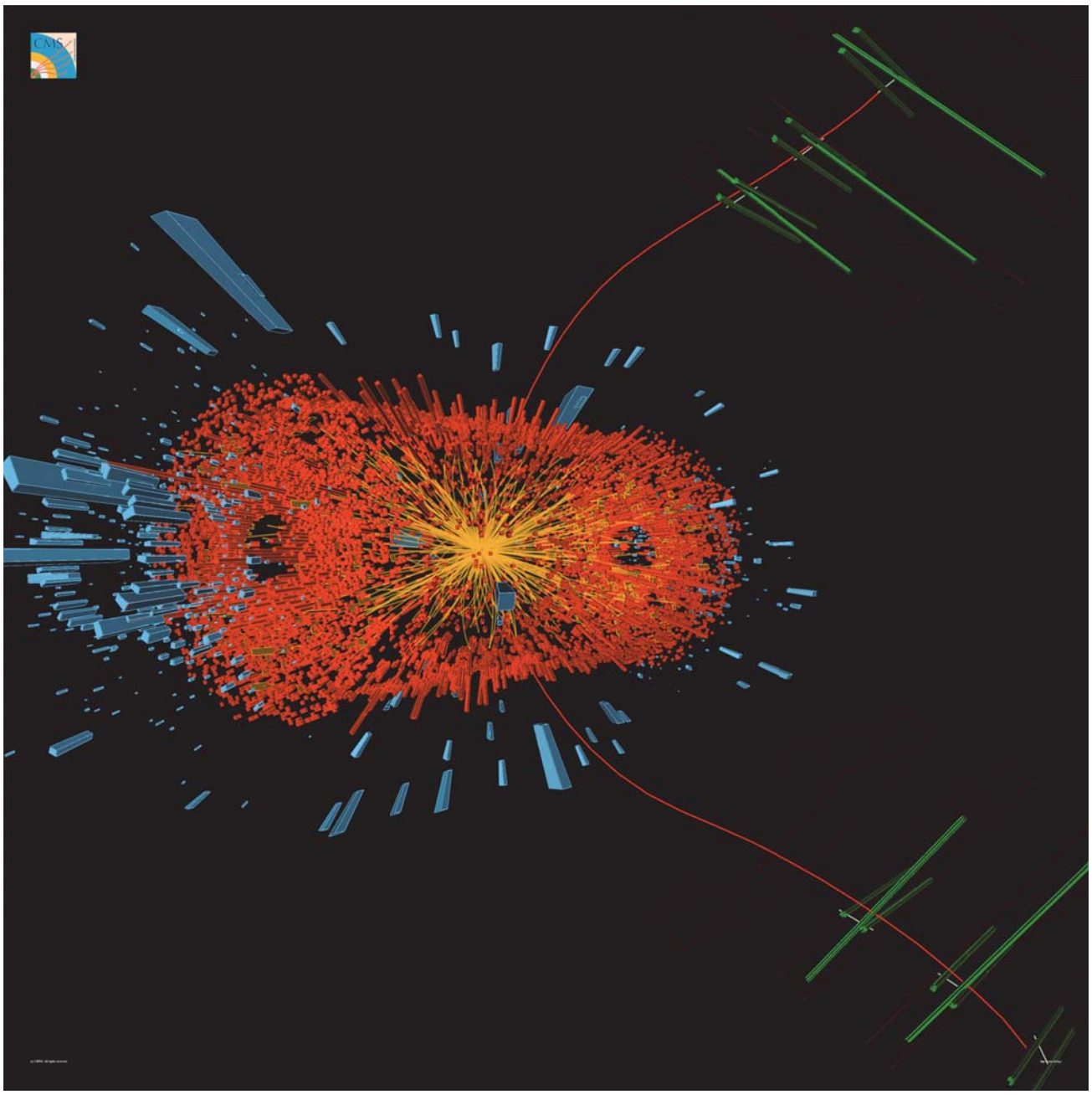

Figure 4.3: Candidate Υ decay to two muons observed in a lead-lead collision at the LHC. The two red lines (tracks) are the two muons, the multiple orange lines are tracks from other particles produced in the collision, whose energy is measured in the electromagnetic calorimeter (red cuboids) and the hadron calorimeter (blue cuboids).

Chapter 5

Datasets

5.1 PbPb dimuon trigger and skim

A primary dataset based on all events selected by the muon trigger has been used for this analysis. The RAW files and the prompt reconstruction files are stored at T1_FR_CCIN2P3. At the Tier-1, they were skimmed for events with two global muons that form a pair with an invariant mass of more than 2 GeV/c^2. All charge combinations have been considered in the pairing. In addition to a muon trigger firing in the event, a coincidence with the minimum bias trigger was required. This minimum bias trigger was defined by the logical OR of the following three triggers, which were not prescaled during the run:

- A bunch crossing signal sent by the beam pick-up timing detector (BPTX) and, two coincident hadronic forward (HF) towers above a certain threshold (set in the firmware) on each side of the detector or at least one beam scintillator counter (BSC) segment (of the 16) giving a signal on each side of the detector :
  L1_HcalHfCoincPmORBscMinBiasThresh1_BptxAND_instance1.

- BSCThreshold1 which requires at least one BSC hit on each side (out of the 32 channels). 'NotBsc2' is always 'True' so it can be ignored.

- Coincidence of two HF towers on each side of the detector.

Signal candidates are required to have fired the double muon trigger path. This trigger was not prescaled during the whole run. It is based solely on L1 decisions and requires the presence of two L1 muon objects with quality > 4, without any constraint on their momenta. Coincidence with the BPTX trigger is required.

Furthermore, a veto on BSC halo triggers, a reconstructed primary vertex with two or more tracks, and the pixel cluster-length being compatible with the primary vertex to reject previously known as mounsters (PKAM) events (i.e. events with exceptionally high occupancy in the pixel detector) was also required. An additional requirement to remove UPC (ultra peripheral collisions) events was imposed: the offline HF coincidence, requiring at least 3 HF towers on each side of the interaction point with at least 3 GeV energy deposited per tower.

In summary, the events used for this analysis are required to pass the following filters: the BSC halo filter, a reconstructed primary vertex made of at least two tracks, the pixel cluster-length compatibility with the vertex, the requirement of an offline HF coincidence with at least 3 towers on each side of the interaction point in the HF with at least 3 GeV energy deposited per tower, and the high quality double muon trigger.

5.1.1 pp sample

The same *pp* sample as for the 2010 analysis has been used [39, 40, 45]. Signal candidates are required to have fired the trigger path HLT_L1DoubleMu0. The data have been re-reconstructed in the same CMSSW release as the 2011 PbPb data. This is done so that the systematic uncertainties in the tracking and other reconstruction efficiencies cancel in the various ratios.

5.1.2 Monte Carlo samples

Υ(1S) events were simulated in PYTHIA [42] and embedded into HYDJET [43]. For this Υ(1S) were generated with realistic p_{T} and rapidity distributions in several bins of p_{T} (0–3, 3–6, 6–9, 9–12, 12–15, 15–30, and $> 30\,\mathrm{GeV}/c$) to enhance the statistics at high p_{T}. The data analysis starts with the Onia2MuMu skim which contains all pairs of global muons with an invariant mass larger than 2 GeV/c. All charge combinations are considered and all possible combinations within an event are kept. Starting from this skim a TTree is filled with single muons and muon pairs that pass quality criteria to reject the background of fake muons while keeping the efficiency of selecting real muons high.

In order to select good quality muons, different variables were studied. This section describes how the cuts are defined and what is the final set of quality criteria that used in the analysis.

Muon candidates are selected if reconstructed as *global muons*. Muon arbitration requirements are applied, specifically muons must be both global and tracker muons. Muon candidates are accepted if they belong to the kinematic region given by

$$|\eta^{\mu}| < 2.4 \quad \text{and} \quad p_{\mathrm{T}}^{\mu} > 4.0\,\mathrm{GeV}/c\,. \tag{5.1}$$

This region is within acceptance for muon reconstruction.

5.1.3 Optimization procedure

The leading figure of merit employed in the optimization study is the Υ(1S) peak significance, $\mathcal{S}$, defined as

$$\mathcal{S} \equiv \frac{N_{\mathrm{signal}}}{\sqrt{N_{\mathrm{signal}} + N_{\mathrm{background}}}}\,, \tag{5.2}$$

where N_{signal} and $N_{\mathrm{background}}$ are the Υ(1S) signal and background yields, respectively, estimated in a ± 100 MeV/c^2 signal window around the Υ(1S) peak. The signal yields are obtained from the Monte

Carlo sample. The background yields are estimated from the data in the signal window. The starting signal/background level is set from a fit to the data obtained with default cuts. Possible dependencies of the determined significance on the starting default cuts or signal-window size are inspected, and alternative figures of merit are also further explored (see subsection 5.1.5).

The samples used include:

- realistic Υ embedded in HYDJET PbPb background: where the signal efficiency can be studied with the caveat that because one signal is embedded per minimum bias event, the signal over background ratio is greatly over-estimated;
- prompt reconstruction of the data: where the background rejection can be studied.

5.1.4 Track and dimuon quality

The following quantities are studied:

- the number of valid hits within the pixels and the strips (inner tracker) a single muon track has, indicating how good the inner part of the track is;
- the number of pixel layers, with valid hits, crossed by a single muon. There are 2-3% of muons with tracks with 0 pixel hits;
- the χ^2/ndf of the single muon inner track, which indicates the quality of the inner track fit;
- the χ^2/ndf of the single muon global track, which indicates the quality of the global fit;
- the number of valid muon hits;
- the distance between the event vertex and the muon track in the transverse plane, D_{xy}, and the longitudinal plane, D_z, which indicates if the muon comes from a decay in flight or is a prompt muon, and removes cosmics;

- the probability for two tracks to belong to the same decay vertex.

In addition to the significance $\mathcal{S}$, the following factors are also estimated: (i) the efficiency of the signal using the MC sample, defined as the signal fraction measured after applying the cut, relative to the number of signal events found before applying the cut; and (ii) the background rejection, defined as one minus the background fraction estimated after applying the cut, relative to the background yield estimated without the cut. These estimators are evaluated for each variable, applying all other cuts, as a function of the cut threshold value. This is an iterative process, where the standard thresholds of Ref. [41] are used as a first iteration step.

The procedure is applied to several track quality criteria. The aim is to confirm the goodness of the standard thresholds applied, and identify potential gains in significance that could be attained by adjusting the threshold of some of the inspected variables. In general, when only marginal significance improvements would be obtained, we opt to conservatively retain the initial standard cut thresholds; this is true in particular for those variables which could be affected by possible mismatches between data and simulation.

Figures 5.1–5.8 show, for each variable, the variation of the significance $\mathcal{S}$, on the left. On the right hand side, the signal efficiency and background rejection, as functions of the probed cut value, are also displayed. For all variables but the one being studied, the default values are applied.

Figure 5.1 shows that, for the inner track number of valid hits, the significance starts dropping when more than 13 valid hits for the muon inner track are required on the data and the efficiency starts dropping at 12. The cut chosen is mu_innerTrack_Hits>10.

Figure 5.2 shows that for the number of pixel layers, with valid hits, crossed, the significance and the efficiency are flat for 1 or 2 but there is a slight efficiency drop with the requirement of 3 pixel layers to be fulfilled, as does the significance slightly. The cut chosen is mu_pixelLayers> 0.

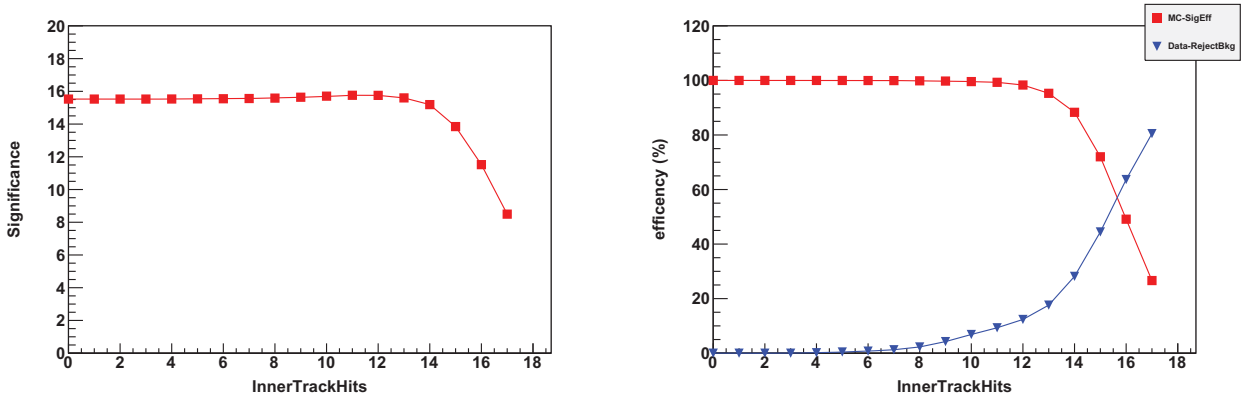

(a) Significance

(b) Signal and background rejection efficiencies

Figure 5.1: Number of muon inner track valid cut study (default: > 10): left, significance on the data and right, efficiency and background rejection on MC. Final cut >10.

Figure 5.3 shows that for the inner track χ^2/ndf, the significance is mostly flat while the efficiency increases until about 2 and then stay maximal. The conservative cut picked is:

mu_innerTrack_chi2NDOF<4.

Figure 5.4 shows that for the global track χ^2/ndf, the significance increases up to above 4 and then is constant. The conservative cut picked is:

mu_globalTrack_chi2NDOF<20.

Figures 5.6 and 5.7 show the significance on data and the efficiency and background rejection on MC for different values of D_{xy} and D_z while applying all other cuts. The final cuts are chosen: mu_dxy<3.0 cm and mu_dz<15.0 cm.

Figures 5.8 show for the vertex probability study, the significance is constant as all other cuts are applied. A reasonable 5% cut for the vertex probability is chosen.

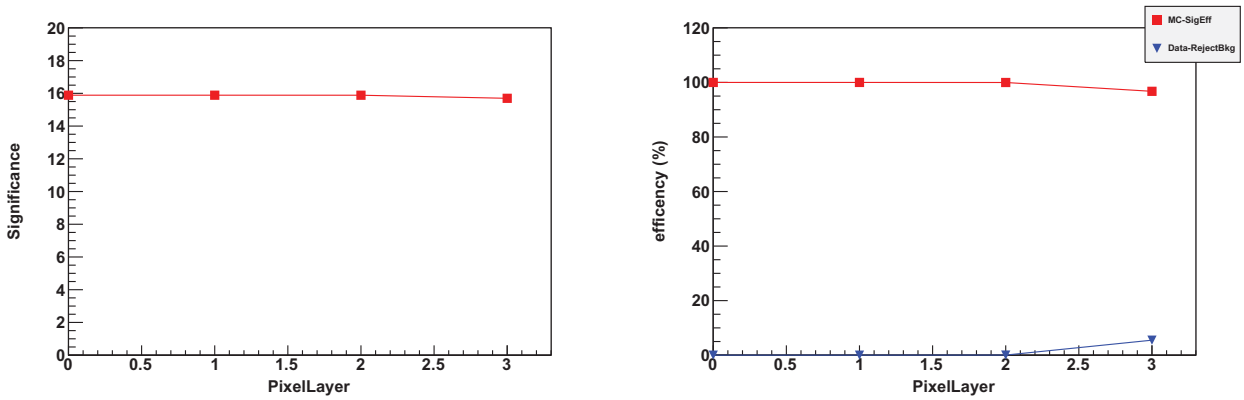

(a) Significance

(b) Signal and background rejection efficiencies

Figure 5.2: Number of muon pixel layers cut study (default: > 0): left, significance on the data and right, efficiency and background rejection on MC. Final cut>0.

5.1.5 Kinematic threshold

The single muon p_{T} cut was chosen according to the optimization procedure described, considering also the effect of the p_{T} cut on the shape of the background.

Statistical optimization

The optimization of the single muon p_{T} cut is based on the 1S peak singificance, as in Eq.(5.2). Similarly to what we have described above, the signal is determined from MC counting the dimuons falling into the $\pm 100\,\mathrm{MeV/c^2}$ mass window around the Υ(1S) peak normalized to the signal in data. The signal yield in data is determined from the simultaneous fit of the Υ(nS) mass peaks and the background, where we take the integral of the 1S peak fit in the same mass window. The background is derived from the mass sidebands, counting the dimuons falling into two $1\,\mathrm{GeV/c^2}$wide intervals placed symmetrically around the Υ(1S) peak. The number of counts then must be normalized to the size of the signal window to estimate the background below the peak.

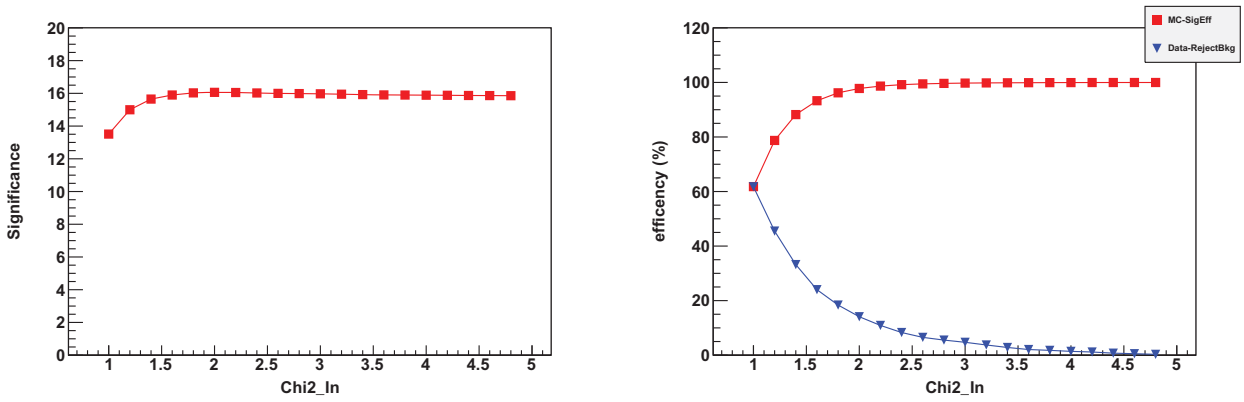

(a) Significance

(b) Signal and background rejection efficiencies

Figure 5.3: Number of muon inner track χ^2/ndf cut study (default: < 4): left, significance on the data and right, efficiency and background rejection on MC. Final cut <4.

The results of the calculation are shown in Fig. 5.9 for three different values of the signal mass-window size. The points show a maximum at the single muon $p_{\mathrm{T}} > 4.0$ GeV/c. The results with a larger mass-window are expected to be more relevant for a better description of the signal. The results with the narrow window could be missing some fraction of the signal. This optimization method indicates the best choice of the cut value to be 4.0 GeV/c.

It is important to note that this optimization procedure finds the single muon p_{T} cut giving the most significant Υ(1S) yield. Beacause one of the main goals of this analysis is the measurement of the relative suppression of Υ excited states with respect to the ground state and pp reference, alternative figures of merit are further investigated. It should be further noted that systematic effects are not accounted for in the procedure.

Background shape sculpting

In the selection of the single muon p_{T} cut, the dependence of the backgtound shape on the choice of the p_{T} cut should be also considered. These effects may be conveniently estimated by

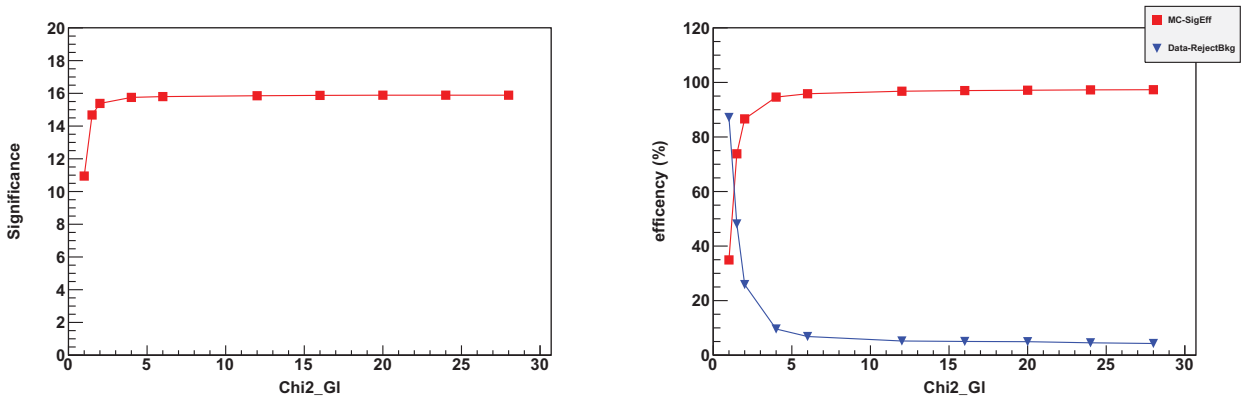

(a) Significance

(b) Signal and background rejection efficiencies

Figure 5.4: Number of muon global track χ^2/ndf cut study (default: < 20): left, significance on the data and right, efficiency and background rejection on MC. Final cut <20.

inspecting the invariant mass spectrum of the same-sign muon pairs. Figure 5.10 shows the same-sign muon-pairs mass spectra, in the vicinity of the $\Upsilon(n\mathrm{S})$ mass region, obtained with different p_{T}^{μ} cut thresholds. The $\Upsilon(n\mathrm{S})$ nominal signal masses are: 9.46 (1S), 10.02 (2S), and 10.36 (3S) GeV/c^2, respectively. In all cases, a peaking background distribution is expected, within the nominal fitting range; the mass value where the maximum occurs increases with the increasing p_{T} cut.

In the previous analysis [39], the cut $p_{\mathrm{T}} > 4\,\mathrm{GeV}/c$ was chosen. In this case, the background displays a peak underneath the Υ(nS) signal mass region. This results in a potentially larger systematic uncertainty associated to the background shape.

In case of the $p_{\mathrm{T}} > 3.5$ GeV/c cut, the peak in the background spectrum is located to the left of the Υ signal region. This should allow a better constraint by the fitter of the background shape under the signal peaks. This argument therefore favors the 3.5 GeV/c cut.

The p_{T} cut dependence of the combinatorial background shape was studied also in pp collisions at $\sqrt{s} = 7$ TeV in data and simulation [37]. A very similar trend is observed in pp collisions with much higher statistics. The kinematic cut removes a large portion of the background in the lower mass region

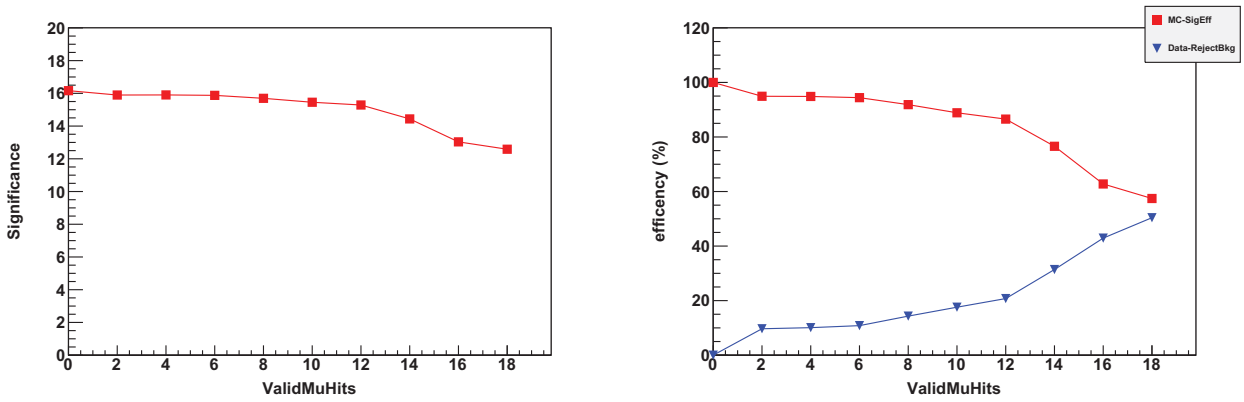

(a) Significance

(b) Signal and background rejection efficiencies

Figure 5.5: Number of valid muon hits cut study (default: ≥ 0).

and produces a step-like shape. For the case of the $p_{\mathrm{T}} > 3.5$ GeV/c cut, this shape is located to the left of the Υ signals; in case of $p_{\mathrm{T}} > 4$ GeV/c cut, it occurs instead well within the signal region, which leads to potential increases of the fit procedure uncertainties.

Alternative figures of merit

Alternative figures of merit were also investigated which aim at optimizing the precision of the ratio measurement (instead of the 1S peak significance).

The first method attempts to minimize the uncertainty on $N(\Upsilon(2\mathrm{S}) + \Upsilon(3\mathrm{S}))/N(\Upsilon(1\mathrm{S}))$, where the ratio is approximately estimated as $2B/(S+B)$. S is the signal counted from the MC $\Upsilon(1\mathrm{S})$ peak and B is the background in the signal window determined from the data sidebands assuming a linear mass shape. The 2S and 3S peaks are approximated by the background hypothesis, that is, assuming the background level overwhelms the signal, which is approximately the case. To normalize the background from data and signal from MC together, the 1S peak in data is fitted and the integral in the given signal window is used as normalization factor.

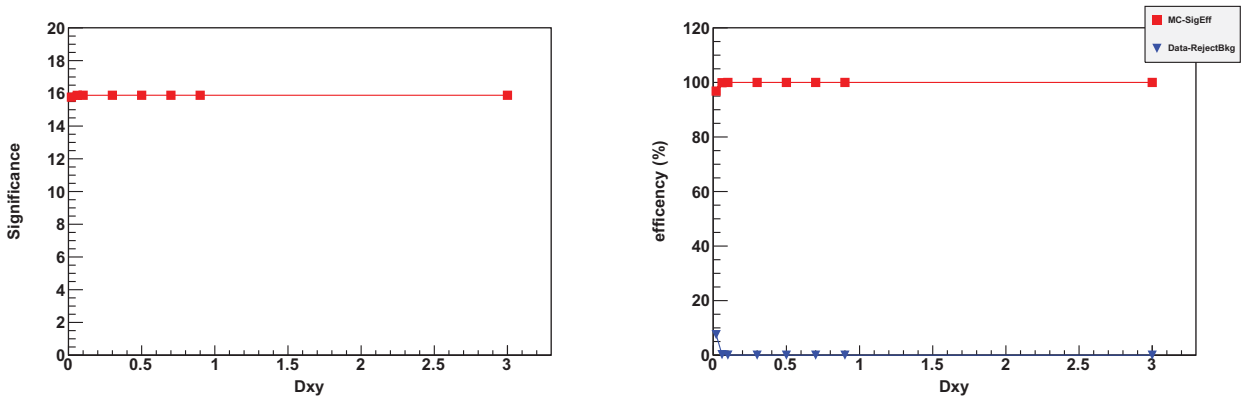

(a) Significance

(b) Signal and background rejection efficiencies

Figure 5.6: D_{xy} cut study (default: < 3).

The uncertainty on the ratio to be minimized is $\frac{2B}{S+B}\sqrt{\frac{1}{2B}+\frac{1}{S+B}}$, as calculated with standard error propagation and using $\sqrt{S}$ and $\sqrt{B}$ as estimates for the uncertainties on S and B. The results of the calculation are shown in Fig. 5.11, for three different values of the signal mass window size. The points reach a minimum at single muon $p_{\mathrm{T}} > 4$ GeV/c independent of the size of the signal window. This optimization method favors a p_{T} cut value at 4 GeV/c.

A third optimization method has also been explored, where we attempt to assess the expected sensitivity on the double ratio directly, by employing pseudo-experiments, generated according to fits performed to the data after each cut. The procedure is as follows. We fit the data sample and then generate 10000 toy MC pseudo data according to parameters in the covariance matrix from the fitting. The double ratio of PbPb /pp is generated at unity in the pseudo-data. The statistics of each sample are fixed to the amount of data we observe. These toys represent the outcome of many CMS experiments assuming nature had no Υ excited state suppression. We plot the distribution of the ratio parameter, χ, measured in each toy experiment. We find the p-value (see Section 11.5) associated to a reference χ

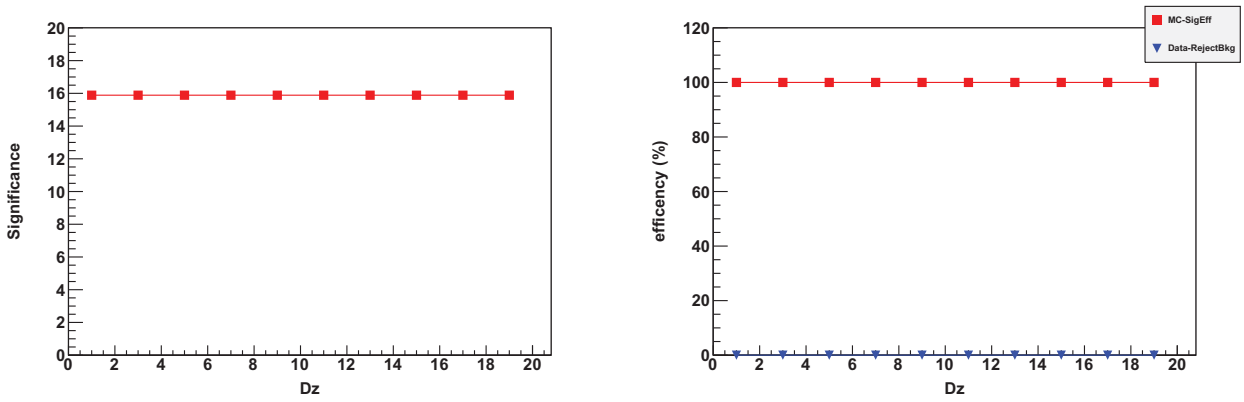

(a) Significance

(b) Signal and background rejection efficiencies

Figure 5.7: D_z cut study (default: < 15).

value, chosen to be 0.5. We repeat the same steps for different selection cuts and identify the best cut the one resulting in the smallest p-value.

The plots for two different single muon transverse momentum thresholds, $p_{\mathrm{T}}^{\mu} > 3.5\,\mathrm{GeV}/c$ and $p_{\mathrm{T}}^{\mu} > 4.0\,\mathrm{GeV}/c$, are shown in Fig. 11.12. The reach of the two cuts is similar with the tighter cut yielding a smaller p-value. This is likely due to the signal to background ratio being better with the tighter cut. However, relevant systematic effects have not been included in the pseudo-experiments study.

Υ(1S) signal p_{T}

If we define the Υ(1S) invariant mass signal region as (9.2, 9.8), the side band region as (8, 8.5) and (12, 14), we can plot the signal p_{T} distribution, side band p_{T} distribution, and side band subtracted p_{T} distribution, as shown in Fig. 5.12. The Υ(1S) signal mean p_{T} is $5.9\,\mathrm{GeV}/c$ after side-band subtraction.

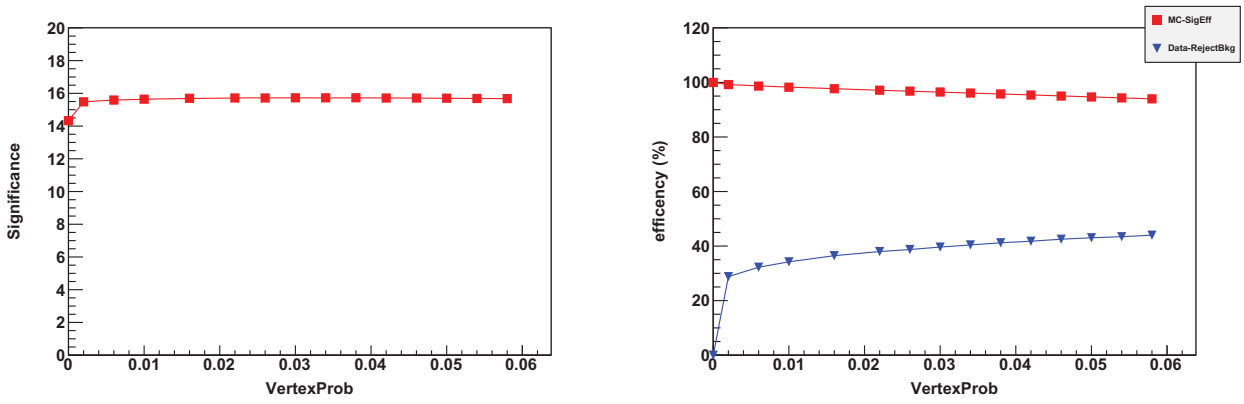

(a) Significance

(b) Signal and background rejection efficiencies

Figure 5.8: Dimuon vertex probability cut study (default: $> 5\%$).

5.1.6 Summary of offline selection

In order to select good quality muons, the effect of different cut thresholds on a variable set was studied. Table 5.1 shows the effect on the significance, as well as signal efficiency and background rejection, when applying all other cuts except the one studied. It gives a further indication of the correlation between the cuts. Once the nominal cut thresholds are applied, variations of a single cut have little impact on the significance.

Table 5.1: Estimated Υ(1S) background rejection in $1-\varepsilon_{\mathrm{Bkg}}$ [%], signal efficiency (from Monte Carlo) and yield significance after applying all other cuts but the one listed.

Cut Variable	real data $1-\varepsilon_{\mathrm{Bkg}}$ [%]	MC $\varepsilon_{\mathrm{Sig}}$ [%]	Significance
InnerTrackHits > 10	51.0	85.0	14.5
PixeLayers > 0	54.1	84.6	14.6
InnerTrackχ^2/ndf <4.	53.2	84.7	14.5
Dxy $<$ 3. cm	54.1	84.6	14.6
Dz $<$ 15. cm	54.1	84.6	14.6
GlobalTrackχ^2/ndf <20	51.8	87.2	15.1
vProb > 0.05	20.2	89.5	13.7
TrackerMuonArbitrated =1	52.7	84.9	14.5
All cuts	54.1	84.6	14.6

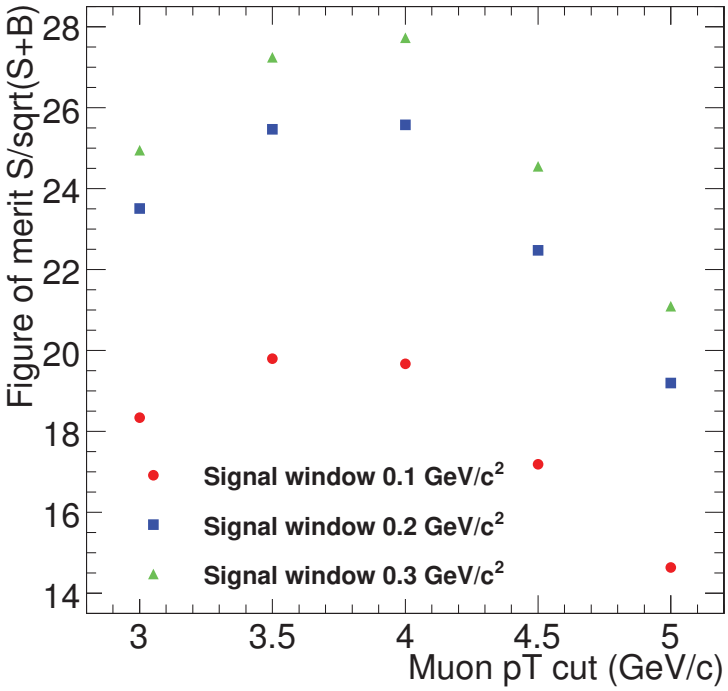

Figure 5.9: Significance of $\Upsilon(1S)$ peak as a function of the single muon p_T cut

The choice of the muon p_{T} cut value involves various considerations. The nominal cut is chosen to be $p_{\mathrm{T}} > 4.0$ GeV/c, which was also used in the previous analysis [39]. This is supported by the outcome of the statistical optimization procedure, employing different heuristic figures of merit; in addition, the systematic effect due to the kinematic background may be controlled, as discussed in Sec. 6.2.

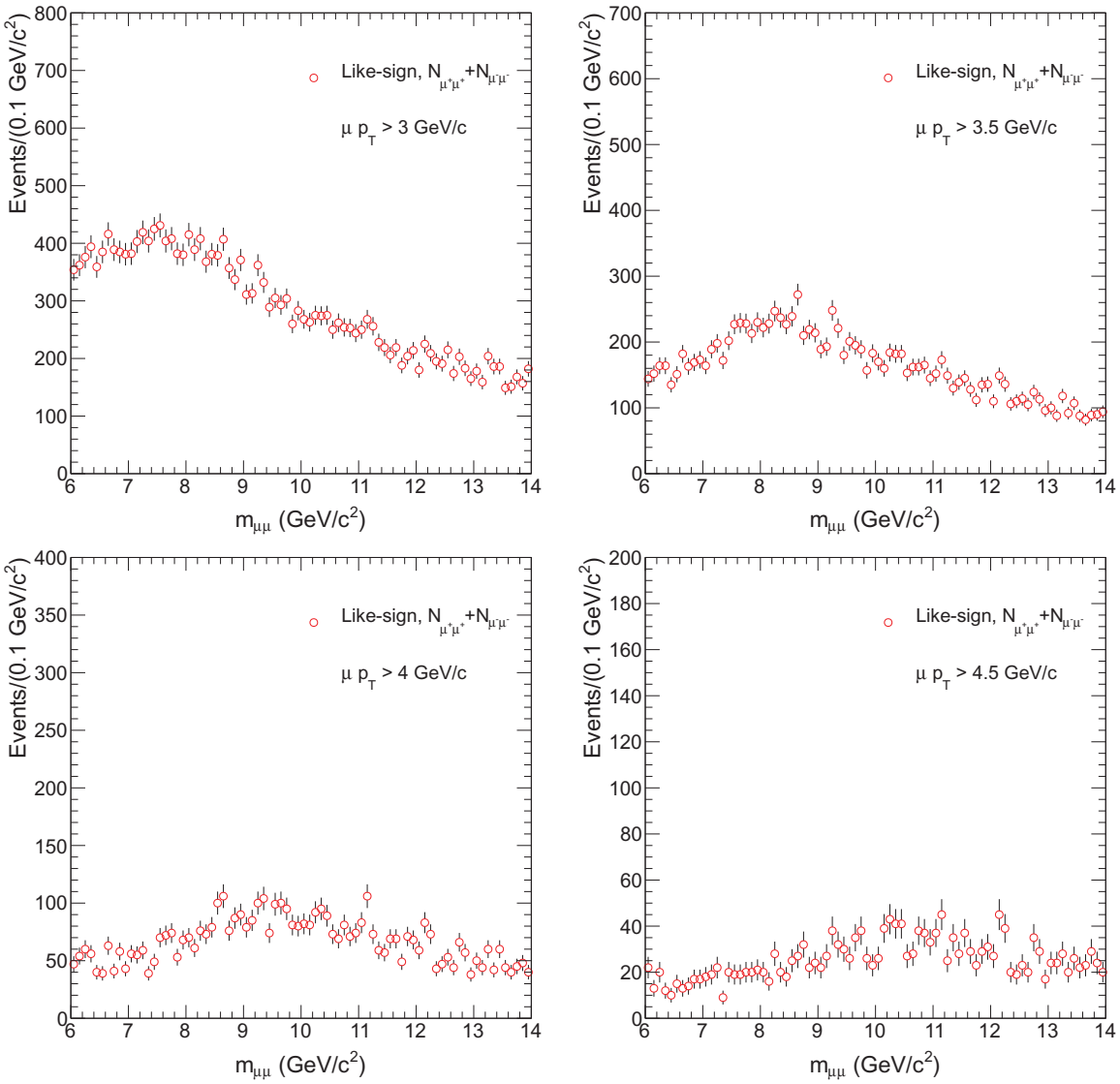

Figure 5.10: Same-sign muon pair invariant mass distribution with different muon p_{T} cuts, in the vicinity of the $\Upsilon(nS)$ mass region.

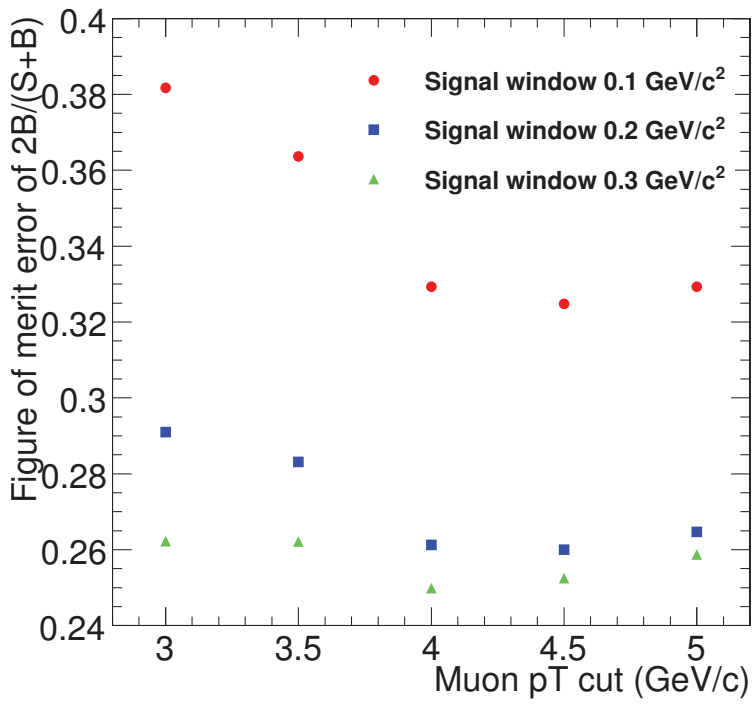

Figure 5.11: Uncertainty on $2B/(S+B)$ as a function of the single muon p_{T} cut.

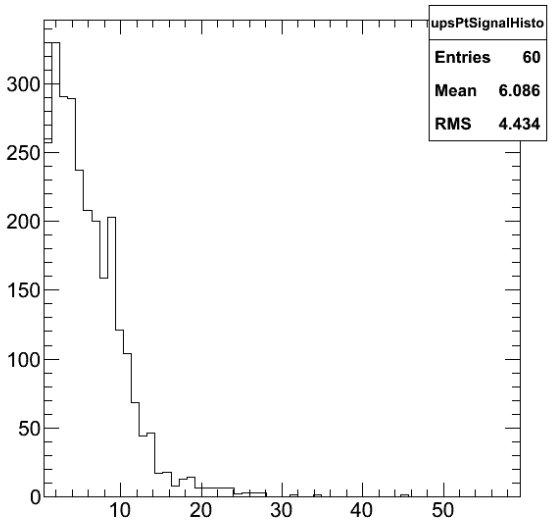

(a) Signal region

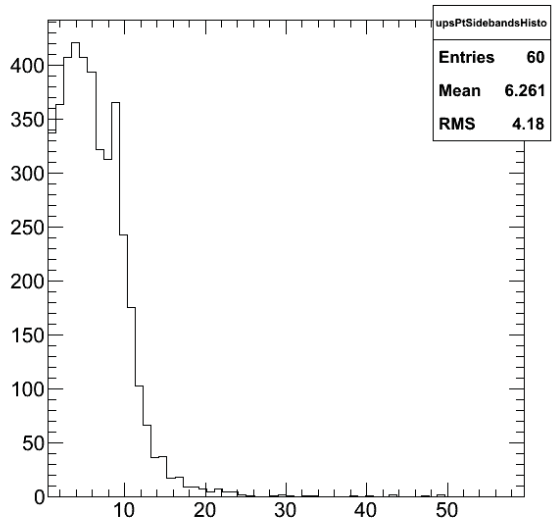

(b) Sideband region

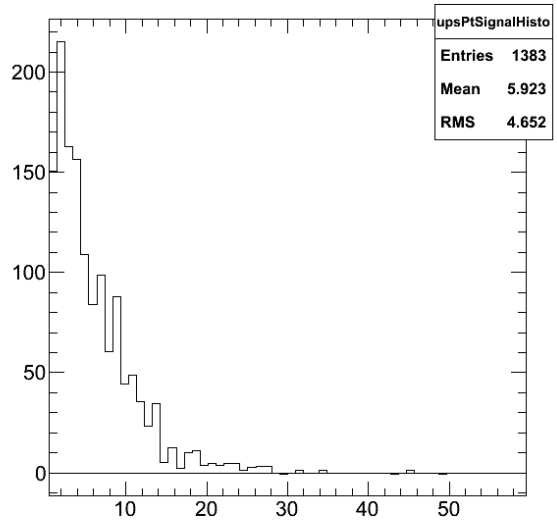

(c) Sideband subtracted

Figure 5.12: Υ(1S) p_{T} distributions.

Chapter 6

Fitting the dimuon spectra

The parameters of interest are extracted from the data samples via an extended unbinned maximum likelihood fit to the dimuon invariant mass spectra. In this section, the fitter study is carried out for two selected p_T^{μ} cuts, 3.5 and 4.0 GeV/c. The final results in Section 11.3 are given with the nominal 4.0 GeV/c cut only. The baseline fitting model is improved relative to the publication using the 2010 dataset. We explored complementary approaches for background modeling (e.g. employing like-sign parameterizations, track-rotation).

The baseline fitting model is inspired in that used in [41, 46]. Each of the Υ(nS) signals is modeled via a crystal-ball shape (CB), which consists of a Gaussian function with the low-side tail replaced with a power law describing final-state radiation (FSR). The crystal-ball function is given by:

$$f(x;\alpha,n,\bar{x},\sigma) = N \cdot \begin{cases} \exp(-\frac{(x-\bar{x})^2}{2\sigma^2}) & \text{for } \frac{x-\bar{x}}{\sigma} > -\alpha \\ A \cdot (B - \frac{x-\bar{x}}{\sigma})^{-n} & \text{for } \frac{x-\bar{x}}{\sigma} \leq -\alpha\,, \end{cases} \tag{6.1}$$

where

$$A = \left(\frac{n}{|\alpha|}\right)^n \cdot \exp\left(-\frac{|\alpha|^2}{2}\right),$$
$$B = \frac{n}{|\alpha|} - |\alpha| .$$

The CB function is parameterized by four parameters – the mass mean $\bar{x}$ and resolution σ, and the tail parameters α and n – which are constrained for the three signal peaks in the following way: the tail parameters are assumed to be the same for all three resonances; the resolution forced to scale with the resonance mass; the differences of the mass means are fixed to their PDG values.

In the previous iteration of the analysis [39], based on the 2010 dataset, the signal PDF shape parameters were fixed from MC simulation: $\alpha = 1.6$, $n = 2.3$, $\sigma_{1S} = 92$ MeV/c^2. In view of the larger dataset currently available, such constraints have been relaxed. Specifically, the following signal shape parameters are free in the fit: the Υ(1S) mass mean and resolution and the tail parameter α. Note that, given that α and n are strongly correlated, the constraint $n = 2.3$ is kept in the fit.

The p_{T} threshold applied for muon selection induces a sculpting of the mass background distribution. The background parameterization adopted corresponds to an exponential function (exp), multiplied by an error function (Erf), where the latter describes the induced kinematic shoulder and is defined as:

$$\mathrm{Erf}(x) = \frac{2}{\sqrt{\pi}} \int_0^x e^{-t^2}\, dt \tag{6.2}$$

The variable x in equation 6.2 is $(m - m_0)/\sqrt{2} * \sigma$. The background model is thus described by three parameters: the exponential decay constant, and the turn-on mean (m_0) and width (σ). All background parameters are left free.

The nominal fit results to the PbPb data are shown in Fig. 6.1.

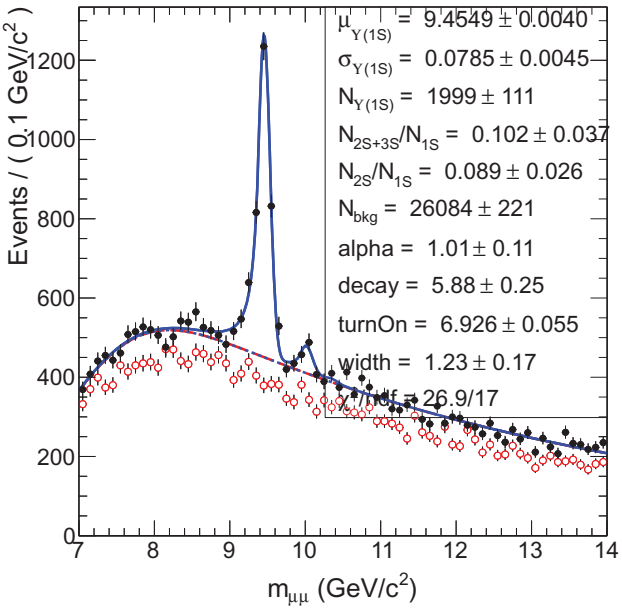

(a) $p_{\mathrm{T}}^{\mu} > 3.5\,\mathrm{GeV}/c$

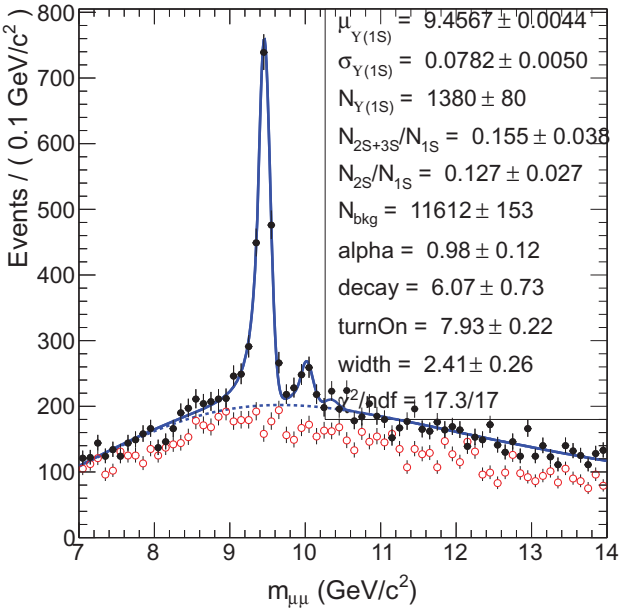

(b) $p_{\mathrm{T}}^{\mu} > 4.0\,\mathrm{GeV}/c$

Figure 6.1: Fit to the dimuon invariant mass distributions for the PbPb sample. ($150\,\mu b^{-1}$)

6.1 Signal model studies

6.1.1 Final state radiation model

We first estimate the CB tail from a Monte Carlo simulation of final state radiation. The MC sample is first split in multiple (about 50) sub samples, of statistics comparable to data. These samples are fitted in turn, and the average parameter values are determined. This is shown in Fig. 6.2.

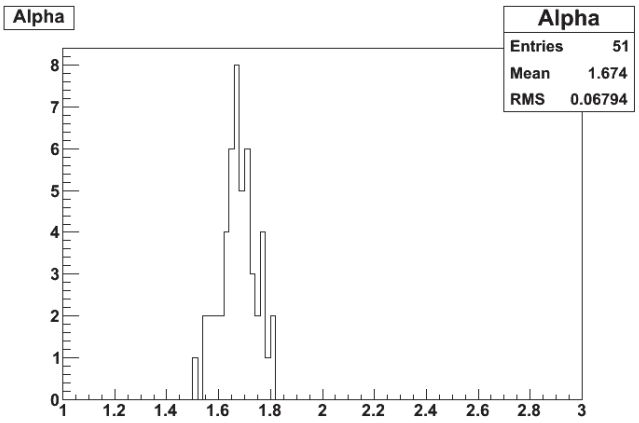

(a) fixed: $\sigma = 92$ MeV/c^2, $n = 2.3$; float: α

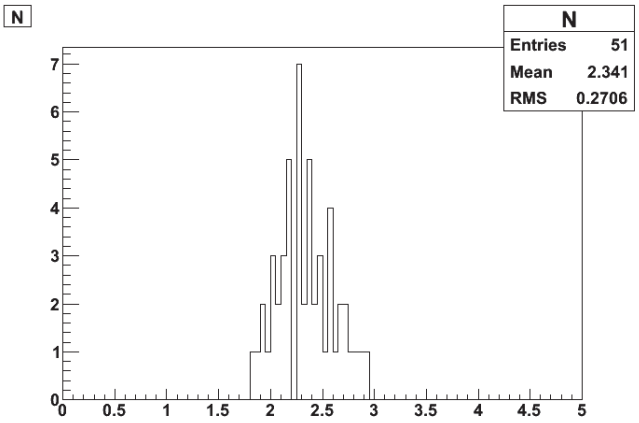

(b) fixed: $\sigma = 92$ MeV/c^2, $\alpha = 1.674$; float: n

Figure 6.2: FSR parameter estimation from MC.

To estimate the CB tail from data, the fit is performed after subtracting the like-sign dimuon mass distribution. This procedure results in a mostly flat remaining background. In this way, the (binned) fit to the subtracted data is able to better constrain the background shape from the mass side-bands, allowing also a more reliable determination of the CB tail. Fit examples are shown in Fig. 6.3.

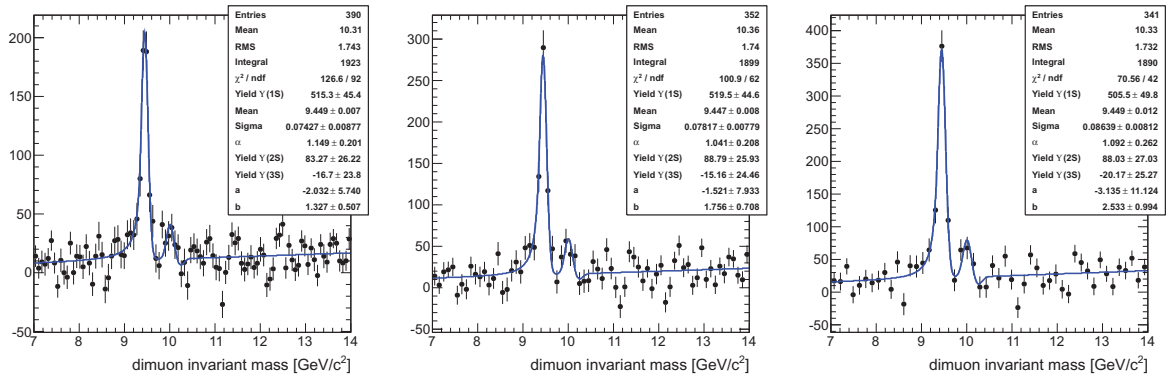

(a) bins:100 (b) bins:70 (c) bins:50

Figure 6.3: FSR parameter estimation from like-sign subtracted data.

Table 6.1 summarizes the CB tail parameter estimations achieved from simulation and data. It illustrates the level of variations that may be attained. In the nominal configuration, the CB α parameter is determined from a nominal fit to the data where α is left free.

Table 6.1: Final state radiation and resolution parameter values.

	α	n (fixed)	σ (MeV/c^2)
Monte Carlo	1.67	2.3	90
pp 7 TeV data	1.4 ± 0.1	2.3	62 ± 2
like-sign subtracted PbPb data	1.0 ± 0.3	2.3	$73 - 87$
PbPb data (nominal fit)	0.98 ± 0.2	2.3	78.2 ± 0.5
PbPb and *pp* data (nominal simul. fit)	1.12 ± 0.13	2.3	79.4 ± 0.4

6.2 Background model studies

We explore alternative estimations and parameterizations of the background, with respect to the nominal model.

6.2.1 Like-sign dimuon spectrum

Here we carry out fits to the Υ data by constraining the background model utilizing information from the like-sign dimuon spectrum. The like-sign dimuon combinations contain no signal component and provide a useful handle to estimate the combinatorial background shape in the mass region under the signal peaks. The like-sign spectrum is not expected to match *exactly*, in shape and normalization, the combinatorial opposite-side spectrum: different, small contributions may arise from Drell-Yan and open heavy flavor sources. This residual component is expected to be smooth and contains no peak, and is accommodated by allowing an extra polynomial component in the fit to the (oppositely charged dimuon) data.

The like-sign dimuon mass distribution is employed to define a PDF component, in the following two ways:

- **Like-sign dataset smoothing.** RooFit is implemented via the class RooKeysPdf [44], which implements a one-dimensional kernel estimation PDF which models (smoothens) the distribution as a superposition of Gaussian kernels, one for each data point, each contributing 1/N to the total integral of the PDF.

- **Like-sign parameterized fit.** We fit the like-sign distribution utilizing an Erf $\times$ Exp model. The high-mass spectrum is well described by an exponential, describing random track combinations. To describe the acceptance turn-on shape induced by the single muon kinematic threshold, the exponential is multiplied by an error function. Tested variations of the turn-on function parameters gave negligible deviations of the extracted yields.

The shape of the like-sign distribution matches well that of the mass sidebands in the opposite-sign sample. The fit to the opposite-sign signal sample is performed employing a linear combination of the like-sign extracted PDF, along with an extra polynomial component. The latter is included in order to allow for potential discrepancies that might arise between the like-sign and opposite-sign mass

spectra. The fit results are displayed in Fig. 6.4 and demonstrate a good description of the data. Notice that for the 3.5 GeV/c p_{T} cut the luminosity is not the full luminosity from the nominal cut of 4.0 GeV/c.

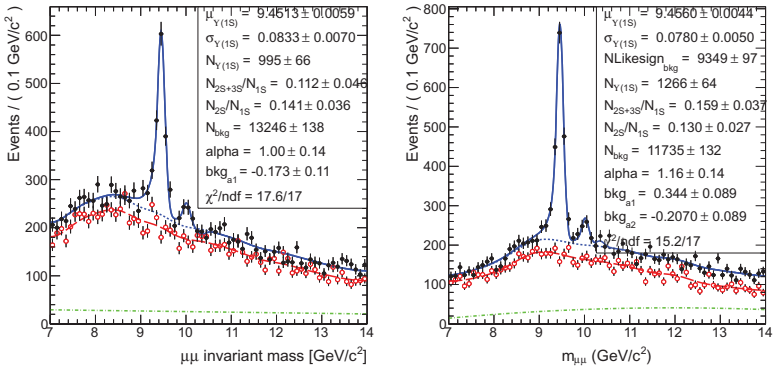

(a) $p_{\mathrm{T}}^{\mu} > 3.5\,\mathrm{GeV}/c$, rookeyspdf, $70\,\mu b^{-1}$

(b) $p_{\mathrm{T}}^{\mu} > 4.0\,\mathrm{GeV}/c$, rookeyspdf, $150\,\mu b^{-1}$

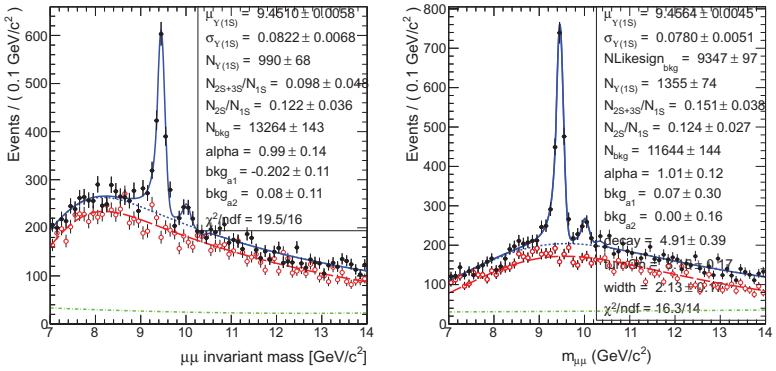

(c) $p_{\mathrm{T}}^{\mu} > 3.5\,\mathrm{GeV}/c$, Exp*Erf, $70\,\mu b^{-1}$

(d) $p_{\mathrm{T}}^{\mu} > 4.0\,\mathrm{GeV}/c$, Exp*Erf, $150\,\mu b^{-1}$

Figure 6.4: Mass fits, with background constrained from like-sign dimuon spectrum.

6.2.2 Track-rotation method

We explore an independent method to estimate the combinatorial background. This is normally referred to as "track-rotation method" and consists of the following steps: (i) all like-sign muon pairs (or the unlike-sign muon pairs) in the event are formed, (ii) for each pair, one of the muons is

randomly selected, and (iii) its ϕ coordinate is rotated by 180° (π). In this way we obtain an uncorrelated sample of tracks, extracted directly from the data and thus matching the data kinematics, from which the combinatorial mass distribution can be estimated.

Having extracted the combinatorial background PDF, the same fitting strategy as described in Sec. 6.2.1 for the like-sign case is employed when fitting the oppositely charged dimuon data. The track-rotation PDF is normalized to like-sign yield. The results are shown in Fig. 6.5 for like-sign, in Fig. 6.6 for unlikesign. They display a good description of the data. A comparison of like-sign pairs shape, track-rotation pairs shape, and unlike-sign pairs shape is shown in Fig. 6.7. We conclude that the model of the error function times exponential accurately describes the mass sidebands in the opposite-sign muon signal sample as well as the alternative estimates of the shape of the combinatorial background obtained from like-sign muon pairs or via a track-rotation method. Hence this is the nominal model used to describe the background.

6.3 Fits to the pp data

The *pp* 2.76 TeV dataset is the same as employed in the previous measurement [39]. The same background fitting model employed therein is adopted as nominal for the *pp* case: a second order polynomial.

To probe statbility of the fit, the same fitting model as devised for the PbPb dataset is applied to the *pp* dataset as well. Fit results are shown in Fig. 6.8 for the nominal background model (error function times exponential), and in Fig. 6.9 for fits utilizing like-sign information. The results are displayed for the $p_{\mathrm{T}}^{\mu} > 3.5\,\mathrm{GeV}/c$ and $p_{\mathrm{T}}^{\mu} > 4.0\,\mathrm{GeV}/c$ selections, and for the cases where the signal shape parameters are left floating and are fixed to the PbPb results. Despite the large number of parameters of the background model, when applied to the limited-statistics *pp* dataset, the fit results show a fair stability. The background model chosen for the *pp* dataset, given that there

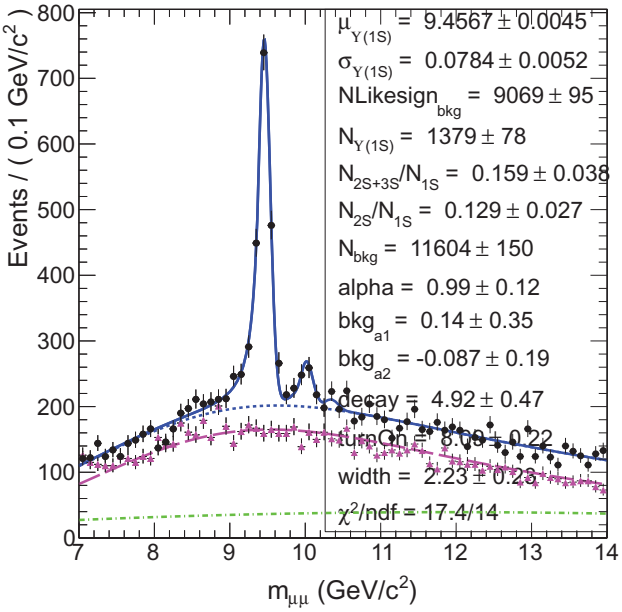

(a) Erf*Exp + pol.2

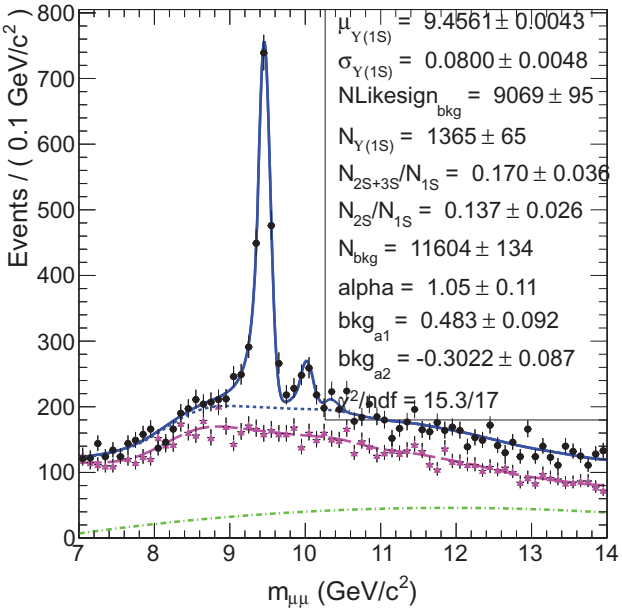

(b) keysPdf + pol.2

Figure 6.5: Mass fit to the invarinat mass distribution, with background constrained from the track-rotated like-sign dimuon spectrum shown in dashed "magenta curve" ($p_{\mathrm{T}}^{\mu} > 4.0\,\mathrm{GeV}/c$, $150\,\mu b^{-1}$).

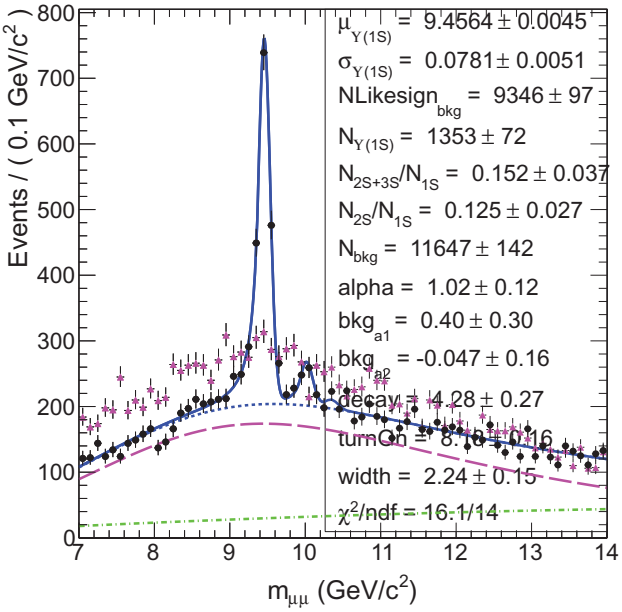

(a) Erf*Exp + pol.2

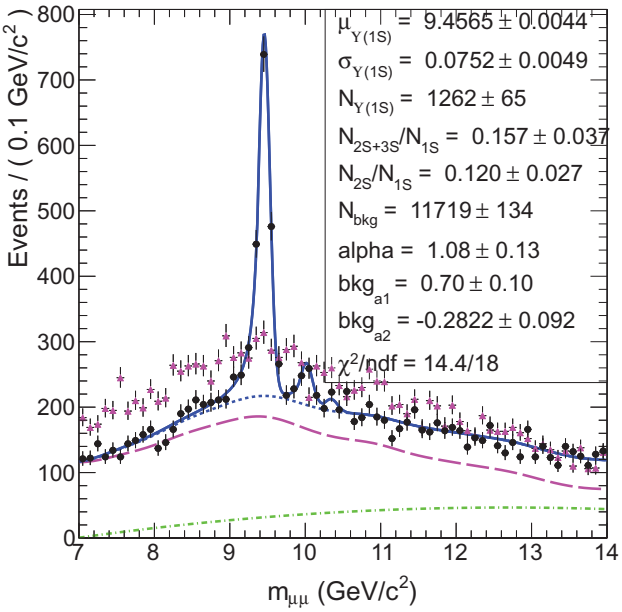

(b) keysPdf + pol.2

Figure 6.6: Mass fit to the invariant mass distribution, with background constrained from the track-rotated unlike-sign dimuon spectrum shown in dashed "magenta curve". The magenta curve is normalized to like-sign pairs yield.

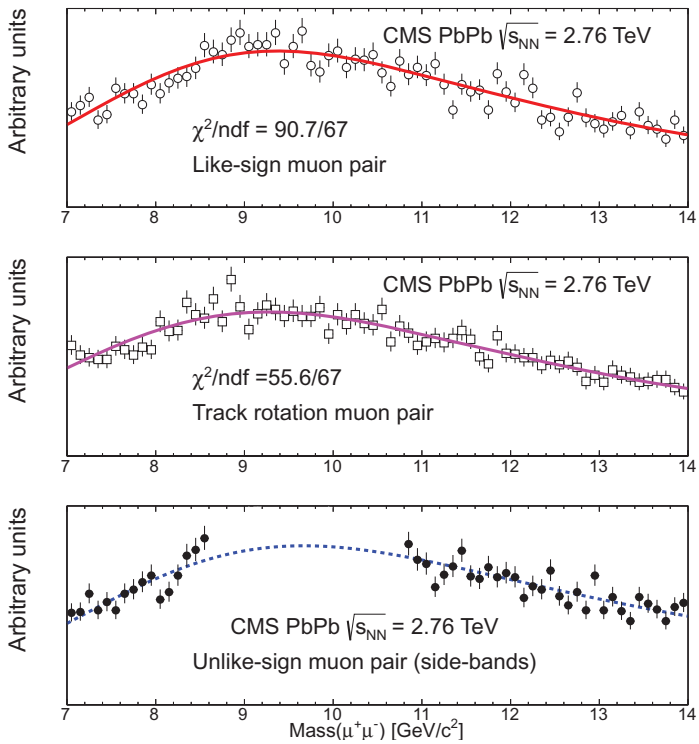

Figure 6.7: Comparison of the like-sign, track-rotation, and unlike-sign pairs

was not a signinficant difference amongst the different background models studied, was a second-order polynomial.

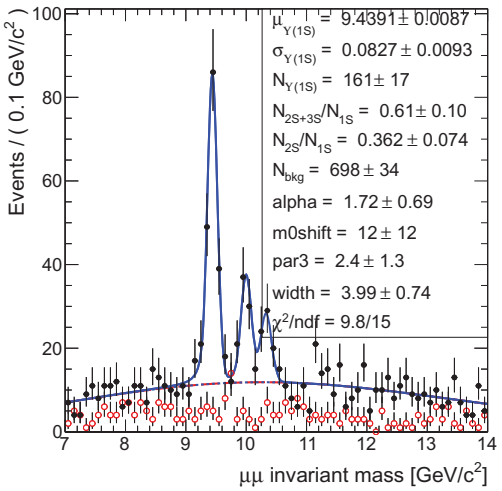

(a) $p_{\mathrm{T}}^{\mu} > 3.5\,\mathrm{GeV}/c$

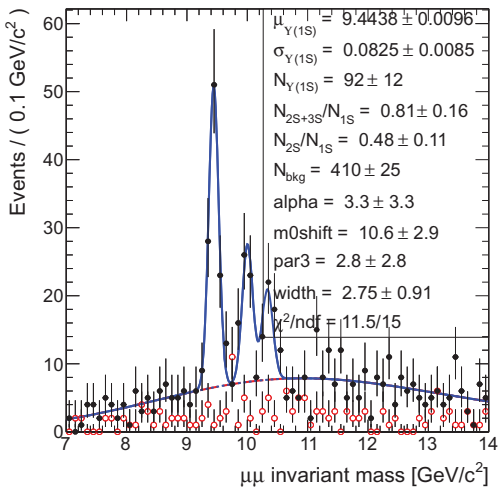

(b) $p_{\mathrm{T}}^{\mu} > 4.0\,\mathrm{GeV}/c$

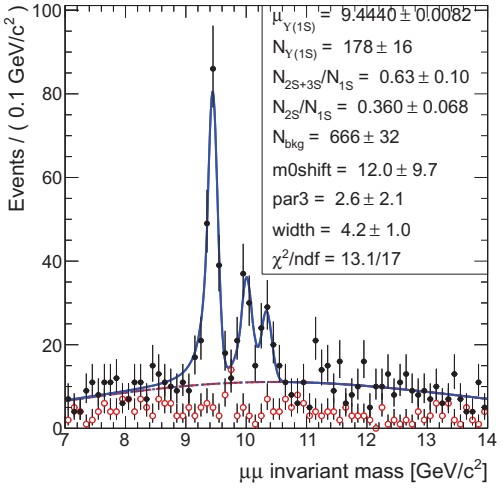

(c) $p_{\mathrm{T}}^{\mu} > 3.5\,\mathrm{GeV}/c$; signal shape fixed to PbPb

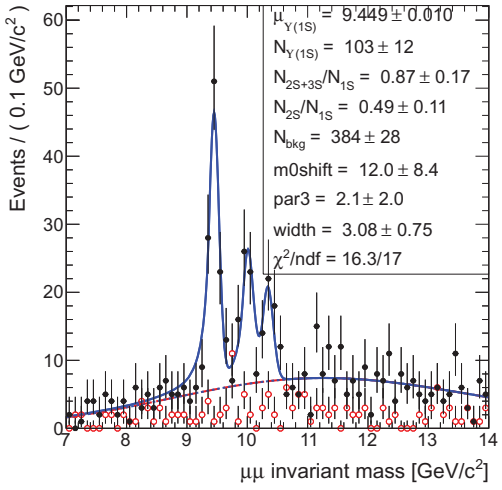

(d) $p_{\mathrm{T}}^{\mu} > 4.0\,\mathrm{GeV}/c$; signal shape fixed to PbPb

Figure 6.8: Mass fits to the pp data ($231\,nb^{-1}$). Figs 6.8(a), 6.8(b): signal shape parameters are left floating; Figs 6.8(c), 6.8(d): signal shape parameters are fixed to the PbPb results.

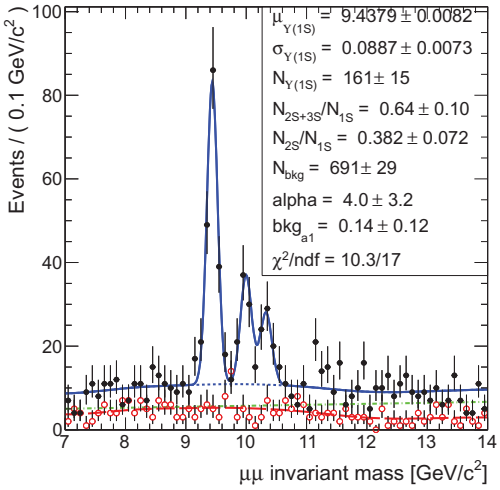

(a) $p_{\mathrm{T}}^{\mu} > 3.5\,\mathrm{GeV}/c$

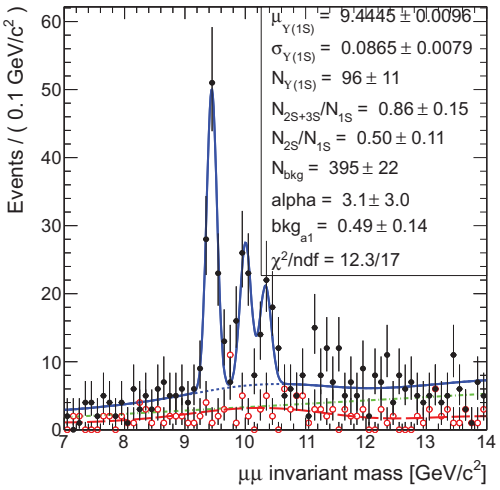

(b) $p_{\mathrm{T}}^{\mu} > 4.0\,\mathrm{GeV}/c$

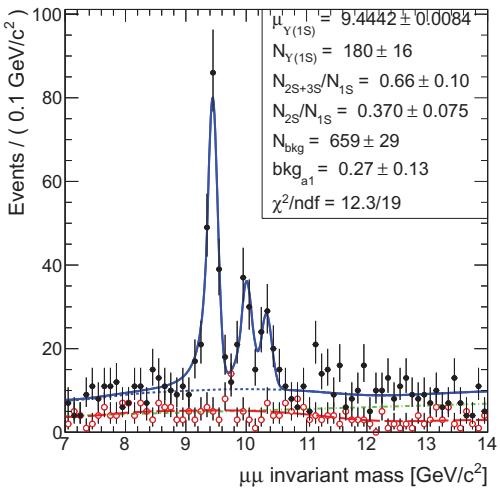

(c) $p_{\mathrm{T}}^{\mu} > 3.5\,\mathrm{GeV}/c$; signal shape fixed to PbPb

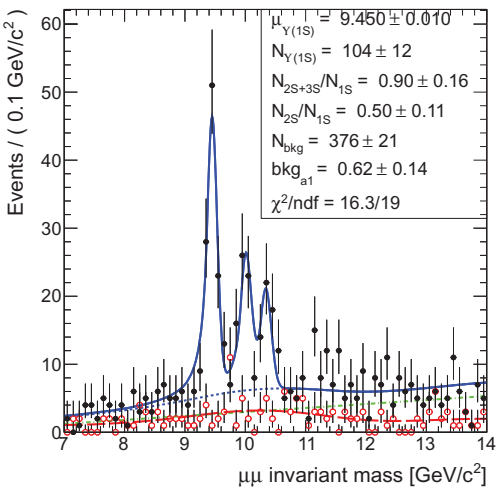

(d) $p_{\mathrm{T}}^{\mu} > 4.0\,\mathrm{GeV}/c$; signal shape fixed to PbPb

Figure 6.9: Mass fits to the pp data ($231\,nb^{-1}$), using like-sign information in red. Figs 6.9(a), 6.9(b): signal shape parameters are left floating; Figs 6.9(c), 6.9(d): signal shape parameters are fixed to the PbPb results.

Chapter 7

Efficiencies

The signal reconstruction efficiencies may differ for the individual $\Upsilon(n\mathrm{S})$ states reconstructed in the *pp* and PbPb data. These are expected to cancel to first order in the double ratio. In this section, these efficiencies and their residual differences are estimated, based on Monte Carlo simulation. In particular, in order to estimate the corresponding corrections required for the double ratio, the reconstruction efficiency is calculated as a function of centrality for the $\Upsilon(1\mathrm{S})$ and $\Upsilon(2\mathrm{S})$ states.

The following ratios of observed yields of Υ excited states relative to the ground state are studied:

$$R_{23} \equiv \frac{N\left(\Upsilon(2\mathrm{S}) + \Upsilon(3\mathrm{S})\right)}{N(\Upsilon(1\mathrm{S}))}, \tag{7.1}$$

$$R_{2} \equiv \frac{N\left(\Upsilon(2\mathrm{S})\right)}{N(\Upsilon(1\mathrm{S}))}, \tag{7.2}$$

$$R_{3} \equiv \frac{N\left(\Upsilon(3\mathrm{S})\right)}{N(\Upsilon(1\mathrm{S}))}. \tag{7.3}$$

known as the single ratios as well as,

$$\chi_{23} \equiv \frac{R_{23|\mathrm{PbPb}}}{R_{23|pp}} = \frac{[N(\Upsilon(2S)+\Upsilon(3S))/N(\Upsilon(1S))]_{\mathrm{PbPb}}}{[N(\Upsilon(2S)+\Upsilon(3S))/N(\Upsilon(1S))]_{pp}}, \quad (7.4)$$

$$\chi_{2} \equiv \frac{R_{2|\mathrm{PbPb}}}{R_{2|pp}} = \frac{[N(\Upsilon(2S))/N(\Upsilon(1S))]_{\mathrm{PbPb}}}{[N(\Upsilon(2S))/N(\Upsilon(1S))]_{pp}}, \quad (7.5)$$

$$\chi_{3} \equiv \frac{R_{3|\mathrm{PbPb}}}{R_{3|pp}} = \frac{[N(\Upsilon(3S))/N(\Upsilon(1S))]_{\mathrm{PbPb}}}{[N(\Upsilon(3S))/N(\Upsilon(1S))]_{pp}}. \quad (7.6)$$

known as the double ratios.

7.0.1 Monte Carlo estimations

In order to make the comparison for the reconstruction (including online and offline selections) efficiency for the $\Upsilon(1S)$ and $\Upsilon(2S)$ in PbPb and *pp* collisions, Monte Carlo events are used, where an Υ is produced and decays via the $\mu^+\mu^-$ channel. We use $\varepsilon = N_{\mathrm{reco}}/N_{\mathrm{gen}}$, where N_{gen} is the number of events that fall within our acceptance conditions ($|\eta| < 2.4$, $p_T > 4\,(3.5)$ GeV/c for each of the muons), and N_{reco} is the number of dimuons that are reconstructed, match the trigger, pass the quality cuts presented in Section 5.1.6, and fall within an invariant-mass window of [9.0,10.0] GeV/c^2 for $\Upsilon(1S)$ and [9.5,10.5] GeV/c^2 for $\Upsilon(2S)$. Yields were estimated by counting and, alternatively, fitting the MC mass spectrum to account for backgrounds.

Tables 7.1 and 7.2 show the reconstruction efficiencies of $\Upsilon(1S)$ and $\Upsilon(2S)$ in various centrality bins with two different single muon p_{T} cuts. It is observed, in Fig. 7.1 and Fig. 7.2 , that the ratio of $\Upsilon(1S)$ and $\Upsilon(2S)$ efficiencies in PbPb collisions is flat with respect to the centrality bins used in the analysis.

Figure 7.3 shows the centrality dependence of the $\Upsilon(1S)$ and $\Upsilon(2S)$ total efficiencies in PbPb, compared with the same in *pp*. The efficiency, for either $\Upsilon(1S)$ or $\Upsilon(2S)$ in PbPb, is shown to decrease as a function of the event centrality (being smallest for the highest multiplicity events, or lowest centrality percentile). This is expected, due to the effect of larger tracking reconstruction inefficiencies for the

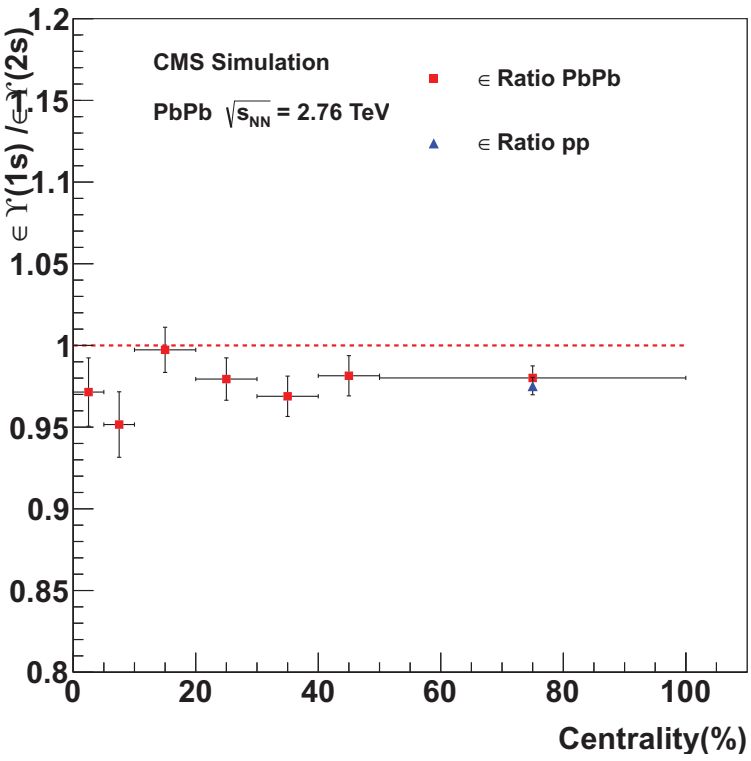

(a) $p_{\mathrm{T}}^{\mu} > 3.5\,\mathrm{GeV}/c$

Figure 7.1: Ratios of total efficiencies ϵ, as a function of centrality, comparing PbPb and *pp* for single muon $p_{\mathrm{T}} > 3.5$ GeV/c.

higher track multiplicities which characterize the more central collisions. The slightly larger efficiency for Υ(2S) than Υ(1S) arises from the softer muon distribution from Υ(1S) decays.

The comparison between *pp* and PbPb events, shown as the rightmost bins in Fig. 7.3, indicates a larger efficiency for PbPb peripheral than *pp*, which is not readily expected. This is clarified in Fig. 7.4. It shows a decrease of efficiency for very peripheral ($> 80\%$) events, induced by the primary vertex selection requirement. As seen in Fig. 7.4(b), the primary vertex selection efficiency is flat in PbPb for centralities up to about 80% and is larger than for *pp*: $99.7 \pm 0.4\%$ (PbPb) vs $96.5 \pm 0.1\%$ (*pp*). For peripheral PbPb as well as for *pp* collisions, which are characterized by small track multiplicities, the primary vertex selection induces inefficiencies. It is shown, finally in Fig. 7.4(a), that

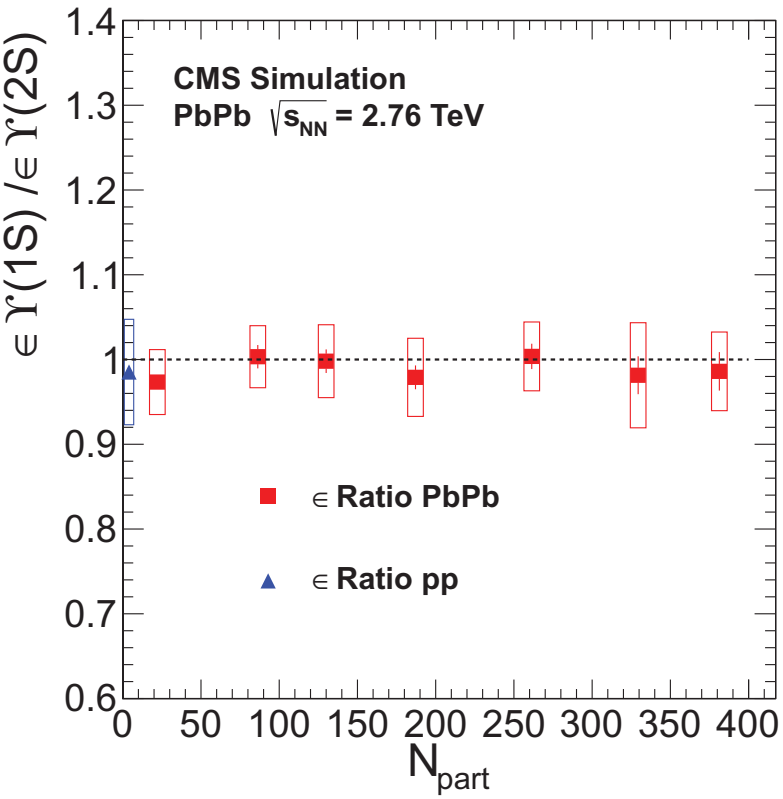

(a) $p_{\mathrm{T}}^{\mu} > 4\,\mathrm{GeV}/c$

Figure 7.2: Ratios of total efficiencies ϵ, as a function of centrality, comparing PbPb and *pp* for single muon $p_{\mathrm{T}} > 4$ GeV/c.

the efficiencies for *pp* and most peripheral events coincide. In addition to these verifications in MC, the primary vertex selection efficiency was estimated directly in the *pp* minbias dataset as well: the fraction of events found to satisfy this selection requirement is $95.9 \pm 0.8\%$, in agreement with the *pp* value estimated in MC quoted above ($96.5 \pm 0.1\%$).

Figure 7.1 shows the centrality dependence of the Υ(1S)/Υ(2S) ratio of total efficiencies in PbPb, compared with the same in *pp*. In order to estimate possible efficiency corrections to the double ratio observable, we calculate the double ratio of efficiencies:

Table 7.1: Reconstruction efficiency for Υ(1S) and Υ(2S) embedded in MB HYDJET sample. An acceptance cut of single muon $p_T > 4.0$ GeV/c is applied for these values.

	Centrality	Υ(1S)	Υ(2S)
PbPb	$[0-100\%]$	$48.6 \pm 0.2\%$	$49.3 \pm 0.2\%$
	$[0-5\%]$	$46.6 \pm 0.6\%$	$47.3 \pm 0.8\%$
	$[5-10\%]$	$47.1 \pm 0.6\%$	$48.0 \pm 0.8\%$
	$[10-20\%]$	$49.2 \pm 0.5\%$	$49.0 \pm 0.5\%$
	$[20-30\%]$	$49.1 \pm 0.5\%$	$50.2 \pm 0.5\%$
	$[30-40\%]$	$51.0 \pm 0.4\%$	$51.1 \pm 0.5\%$
	$[40-50\%]$	$51.7 \pm 0.5\%$	$51.5 \pm 0.5\%$
	$[50-100\%]$	$51.6 \pm 0.3\%$	$53.0 \pm 0.3\%$
	$[50-60\%]$	$51.1 \pm 0.4\%$	$53.0 \pm 0.4\%$
	$[50-100\%]$	$52.1 \pm 0.3\%$	$53.0 \pm 0.3\%$
pp	–	$48.7 \pm 0.1\%$	$49.4 \pm 0.2\%$

Table 7.2: Reconstruction efficiency for Υ(1S) and Υ(2S) embedded in MB HYDJET sample. An acceptance cut of single muon $p_T > 3.5$ GeV/c is applied for these values; the corresponding results for the nominal analysis selection are shown in Table 7.1.

	Centrality	Υ(1S)	Υ(2S)
PbPb	$[0-100\%]$	$43.6 \pm 0.2\%$	$44.8 \pm 0.2\%$
	$[0-5\%]$	$41.8 \pm 0.5\%$	$43.0 \pm 0.7\%$
	$[5-10\%]$	$42.1 \pm 0.5\%$	$44.2 \pm 0.6\%$
	$[10-20\%]$	$44.1 \pm 0.4\%$	$44.2 \pm 0.4\%$
	$[20-30\%]$	$44.4 \pm 0.4\%$	$45.3 \pm 0.4\%$
	$[30-40\%]$	$45.4 \pm 0.4\%$	$46.9 \pm 0.4\%$
	$[40-50\%]$	$46.0 \pm 0.4\%$	$46.9 \pm 0.4\%$
	$[50-60\%]$	$46.4 \pm 0.2\%$	$47.2 \pm 0.4\%$
	$[60-100\%]$	$46.9 \pm 0.2\%$	$47.9 \pm 0.2\%$
pp	–	$43.5 \pm 0.08\%$	$44.6 \pm 0.2\%$

$$\chi \text{ efficiency correction} \equiv \frac{\varepsilon_{\Upsilon(1S)}/\varepsilon_{\Upsilon(2S)}\ |_{\mathrm{PbPb}}}{\varepsilon_{\Upsilon(1S)}/\varepsilon_{\Upsilon(2S)}\ |_{pp}} .$$

The value of such a possible effciciency correction, evaluated for different centrality bins, is shown in Table 10.4. It is found to lie in the range (0.98 to 1.03). This is found to be consistent and fluctuating about unity; the variations are small and negligible compared to the statistical uncertainty expected for the double ratio measurement.

Though we embed Υ in all centralities in a democratic way, the final MC centrality distribution, shown in Fig. 7.5, is not flat. This is due to the fact that the variable used to define the centrality bins for an event, the number of hits in the Forward Hadronic Calorimeters (HF), is based upon the simulated minimum bias HYDJET PbPb collision. Since a *pp* collision is embedded into the minimum bias event, the underlying event leaves extra hits in the HF, which shifts the number of HF hits up, leaving less most peripheral events. This shift can be most strongly seen for the $> 70\%$ bins.

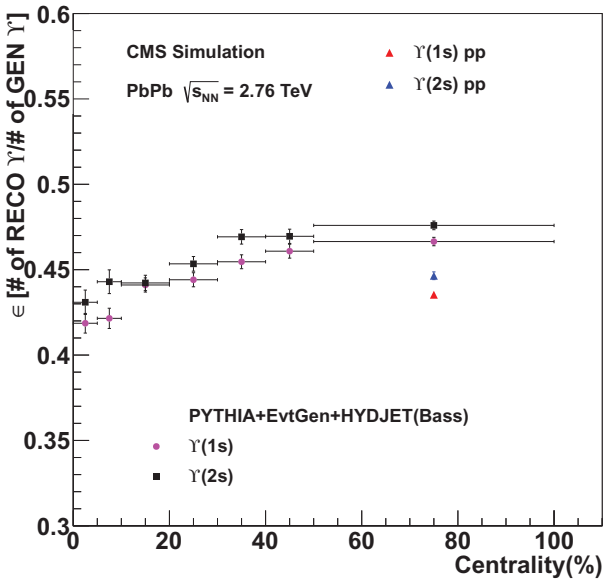

(a) $p_{\mathrm{T}}^{\mu} > 3.5\,\mathrm{GeV}/c$

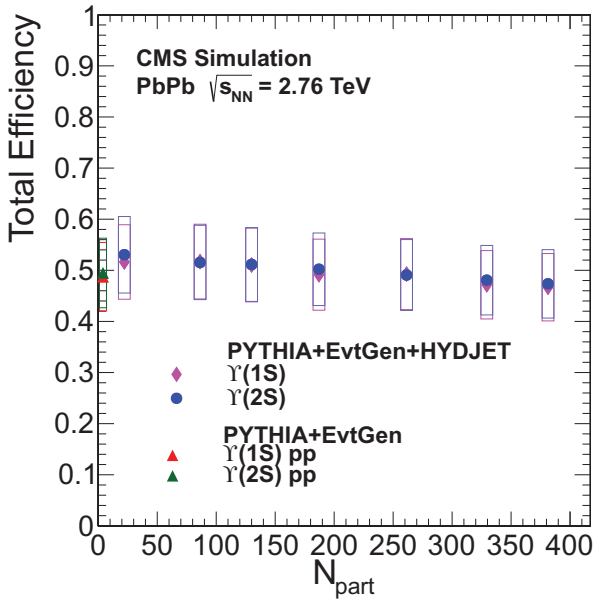

(b) $p_{\mathrm{T}}^{\mu} > 4\,\mathrm{GeV}/c$

Figure 7.3: Total efficiency as a function of centrality, comparing PbPb and *pp*.

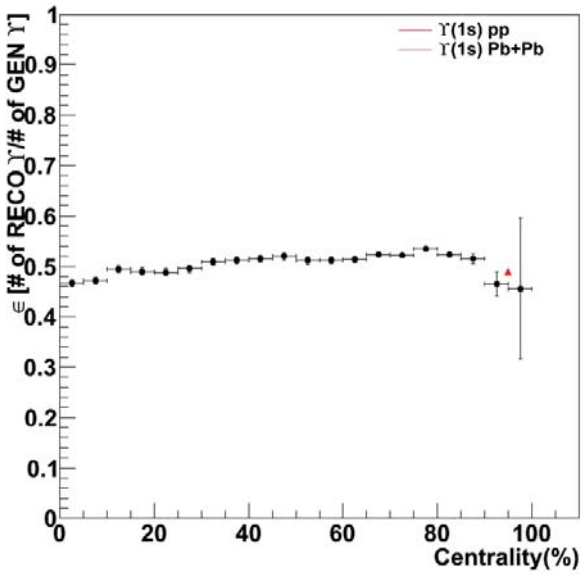

(a) Total Υ(1S) efficiency. The red triangle indicates the *pp* efficiency.

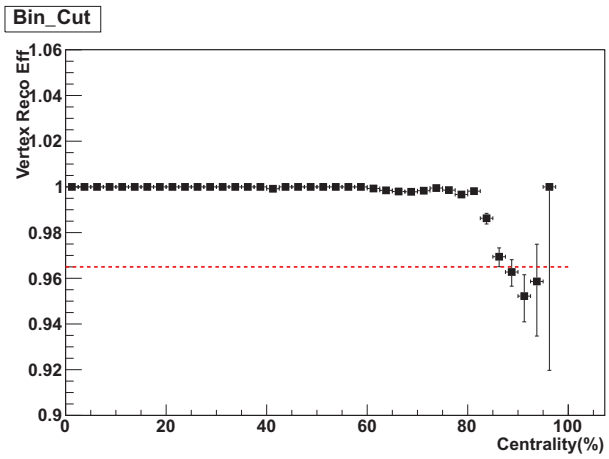

(b) Primary vertex selection efficiency. The horizontal dashed, red line indicates the *pp* efficiency. (Shown for $p_{\mathrm{T}}^{\Upsilon} < 3\,\mathrm{GeV}/c$.)

Figure 7.4: Total and primary-vertex selection efficiencies as a function of centrality, for PbPb simulated events (shown for Υ(1S), $p_{\mathrm{T}}^{\mu} > 4.0\,\mathrm{GeV}/c$). It illustrates an efficiency decrease for very peripheral events.

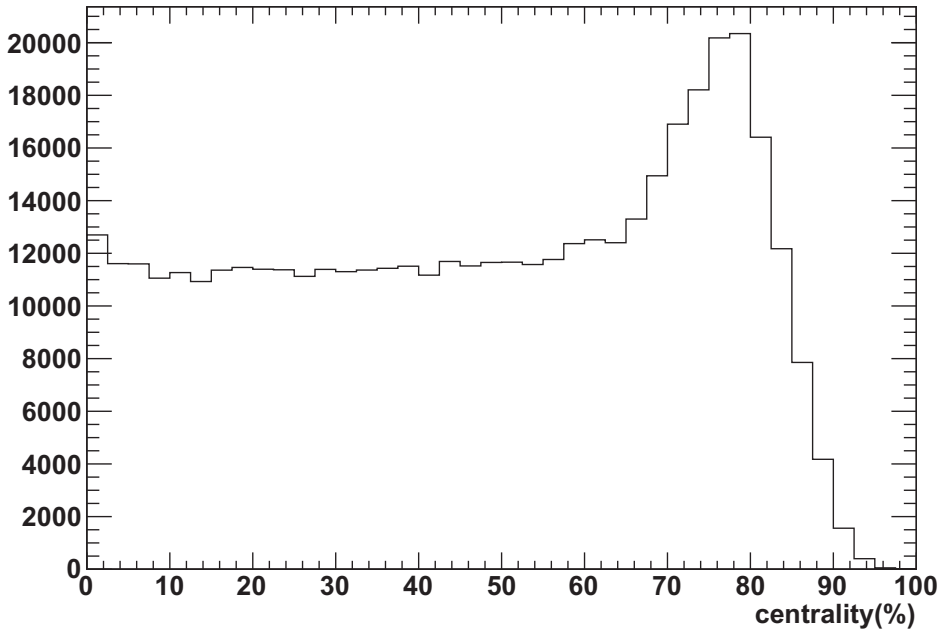

Figure 7.5: Shape of the event centrality distribution in simulation. The non-flatness of the shape in MC is explained in the text.

Chapter 8

Efficiency

We explore the data-driven tag and probe (T&P) method to estimate single-muon trigger, identification, and tracking efficiencies. A comparison of the results obtained by applying the technique to both data and MC simulation allows to estimate related systematic uncertainties.

The procedure is identical to that used in the previous analysis iteration, based on the 2010 PbPb dataset, documented in Ref. [41]. The T&P analysis is done using the official tag and probe framework, as employed for example in Refs. [41, 46]. The J/ψ resonance is used to differentiate signal from background. Two tag-probe invariant mass distributions are formed, in the vicinity of the J/ψ nominal mass, according to whether the probe passes or fails the criteria for which the efficiency is being measured. The two mass distributions are then fit simultaneously and the efficiency ε (and its uncertainty) is extracted as a common parameter in the fit,

$$N_{\text{pass}} = \varepsilon \times N_{\text{probes}} \,, \tag{8.1}$$

$$N_{\text{fail}} = (1 - \varepsilon) \times N_{\text{probes}} \,,$$

where N_{probes}, N_{pass}, and N_{fail} are the number of all probes, passing probes, and failing probes, respectively.

Some challenges arise in measuring the tracking efficiency because in heavy ion collisions fake tracks and tracking efficiency can be "correlated" due to the high multiplicity, i.e. one can have a fake match in events in which one has removed the true match. Yet another problem is that measuring the matching efficiency between a standalone muon and an inner track (necessary to promote a standalone muon to a global muon) is not straightforward in heavy ions [41]. Furthermore, to fit failing tag and probe pairs becomes challenging due to the poor resolution of the standalone (STA) muons. In general, we will compare the efficiency estimations found with T&P in Monte Carlo simulation and data as a cross check of the Monte Carlo based efficiency corrections.

Tags are selected as high quality, global muons, which are matched to the single muon trigger path HLT_HIL1SingleMu0_HighQ, that also pass the offline muon selection used in the data analysis. These tag muons are combined with probe muons to form tag-probe pairs. The probe muon selection depends on the efficiency being measured. A condition is applied to the probes which are split into the passing and failing probe categories. It is the efficiency of this condition relative to all probes that is measured with T&P. We have used the following three probe categories to measure the inner-track reconstruction, muon reconstruction and identification, and muon trigger efficiencies:

- inner-track reconstruction efficiency (including inner to outer track matching, and track quality criteria):
  - probe: a standalone muon (the four-momentum information is taken from the standalone part exclusively)
  - passing probe: probe that is also a global muon passing the quality cuts
- global muon reconstruction and identification efficiency (relative to tracker muon)
  - probe: tracker muon
  - passing probe: probe that can be matched to a global muon and that fulfills the analysis muon selection criteria

- trigger efficiency:
  - probe: (global) muon that satisfies the offline analysis selection criteria
  - passing probe: probe that can be matched to (one leg of) the double muon trigger path.

In order to attempt a reduction of the background level, further selection criteria have been tried. A requirement on the dimuon $p_{\mathrm{T}} > 6.5\,\mathrm{GeV}/c$ is applied as well as a single muon $p_{\mathrm{T}} > 4.0\,\mathrm{GeV}/c$. In all cases, identical selection criteria are applied to both data and simulation: this is necessary for yielding reliable systematic estimates based on data-MC efficiency results comparison.

The efficiency in simulation is measured using T&P on a prompt J/ψ sample. The MC sample is weighted for the centrality dependence (which scales with N_{coll}) and for the relative weights between the different p_{T} bins used in the sample production. While the T&P framework allows for weighted samples, the uncertainty estimates using the current version of RooFit for weighted datasets is not accurate. However, employing large MC statistics, we will take the size of the corresponding errors to be negligible.

The estimation of the systematic uncertainty will be assigned by comparing results between data and simulation. We also note that only results above the single-muon p_{T} of $4.0\,\mathrm{GeV}/c$ are within the acceptance used in the analysis. This tends to reach the muon efficiency plateau, and is less affected by systematics related to the detailed description of the efficiency turn-on.

Trigger efficiency

The trigger efficiency is, in general, the easiest one to fit for, given the cleaner probe sample. The signal shape is describe by a Crystal Ball plus a Gaussian. The addition of the Gaussian is motivated to describe varying detector resolution. The parameters in the Crystal Ball function as well as the width of the Gaussian are free parameters of the fit. The background is described by an exponential function.

Figure 8.1 shows fits to the passing and failing samples of T&P pairs for the trigger efficiency measurement, using the integrated data and MC samples. Figure 8.2 shows the trigger efficiency measured as a function of probe p_{T} and pseudorapidity. Also shown is the trigger efficiency as function of centrality which, as expected, shows no significant dependence.

Muon identification efficiency

We simultaneously fit the passing and failing tag-probe pair mass distributions using a Crystal Ball function and (when needed to account for different resolutions) a Gaussian. A first order polynomial is used to describe the background. For the MC case, a Crystal Ball pdf and an exponential pdf describe the signal and background shapes.

T&P mass fits for the muon identification efficiency are shown in Fig. 8.4, for the integrated data and MC samples. These illustrate the considerably high level of background involved, in the heavy-ion environment. Figure 8.5 shows the muon identification efficiency measured as a function of probe p_{T}, pseudorapidity, and event centrality. Good agreement between data and simulation is observed.

Tracking efficiency

The fits for the tracking efficiency are challenging due to the poor resolution of the standalone muons used as probes. For the same reason, an enlarged fitting range is used. A Crystal Ball pdf (and an additional Gaussian pdf when needed to account for different event resolutions, e.g. for the MC fits) is chosen to describe the signal shape with all its parameters left to float. The background is described by a third order polynomial.

T&P mass fits for the tracking case are shown in Fig. 8.7 for the integrated data and MC samples. These illustrate the considerably large level of background involved and the degraded mass

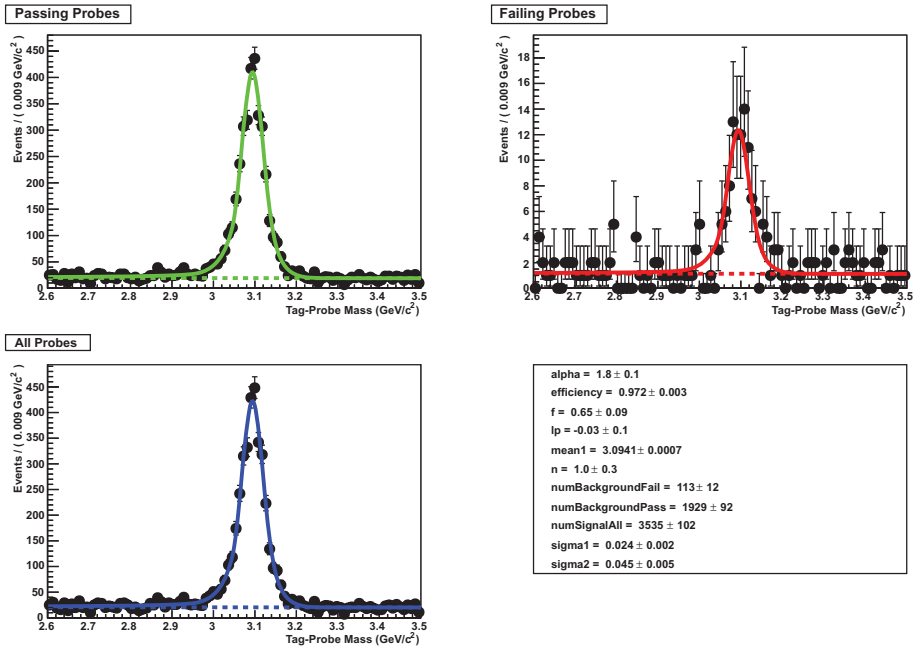

(a) Data

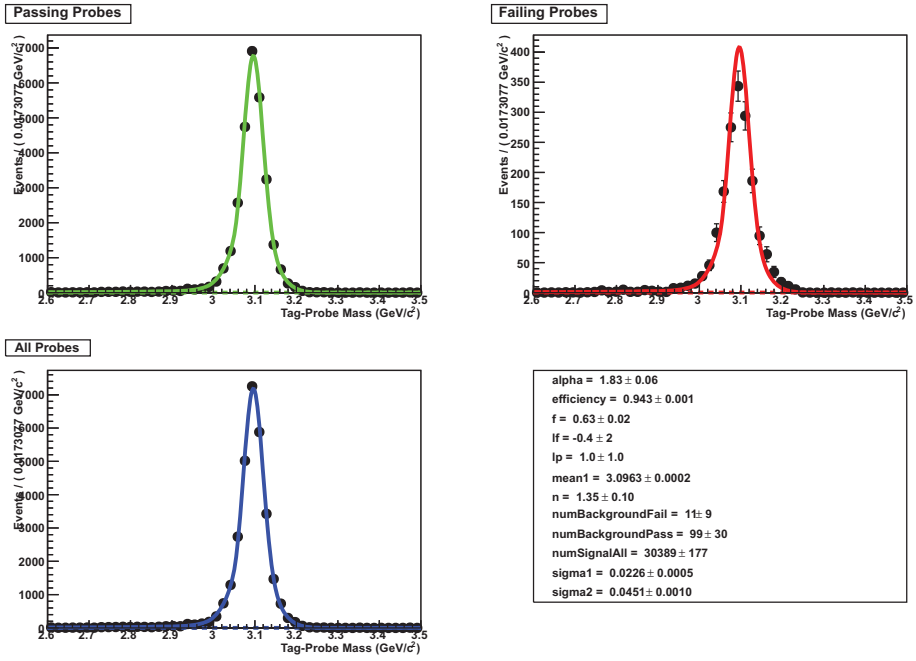

(b) Monte Carlo

Figure 8.1: Examples of T&P pair mass fits used to extract the trigger efficiency for data and MC.

resolution. Shown in Fig. 8.8 is the tracking efficiency as function of the probe muon p_{T}, rapidity and event centrality. The MC is seen to overestimate the data by about 6%.

Finally we summarize in Table 8.1 all the efficiency estimations as a function of centrality, based on the full data and simulation PbPb samples.

Table 8.1: Tag and probe efficiency measurements in PbPb data and simulation; an acceptance cut $p_{\mathrm{T}}^{\mu} > 4.0$ GeV/c on the probe muons is applied; values are in percent, and errors are statistical only.

PbPb	Muon Identification		Trigger		Tracking	
centrality	MC	data	MC	data	MC	data
0-10%	94.6 ± 0.2	94.6 ± 5.0	93.9 ± 2.1	96.7 ± 0.5	83.6 ± 0.4	76.1 ± 2.5
10-20%	95.3 ± 0.3	94.9 ± 1.8	95.1 ± 4.8	96.9 ± 0.5	88.0 ± 0.6	80.6 ± 2.5
20-50%	95.3 ± 0.2	95.8 ± 2.5	94.4 ± 0.7	96.7 ± 0.4	83.1 ± 2.0	81.7 ± 1.5
50-100%	95.9 ± 0.6	97.8 ± 0.8	94.3 ± 0.7	96.8 ± 3.2	86.1 ± 2.0	81.7 ± 1.5
0-100%	95.5 ± 0.1	95.5 ± 4.4	94.3 ± 0.1	96.8 ± 0.2	85.2 ± 0.3	79.6 ± 1.2

Table 8.2 also summarizes the tag and probe results obtained from the *pp* data and MC datasets. These studies were performed in the analysis documented in Ref. [40]. While different selection criteria were employed therein, which prevents a direct comparison of results for *pp* and PbPb, this may be used for the purpose of data–simulation systematic estimation.

Table 8.2: Tag and probe efficiency measurements in *pp* data and simulation; an acceptance cut $p_{\mathrm{T}}^{\mu} > 4.0$ GeV/c on the probe muons is applied; errors are statistical only; results from [40].

	Trigger		Tracking	
	MC	data	MC	data
pp	0.943 ± 0.002	0.925 ± 0.006	0.846 ± 0.010	0.82 ± 0.02

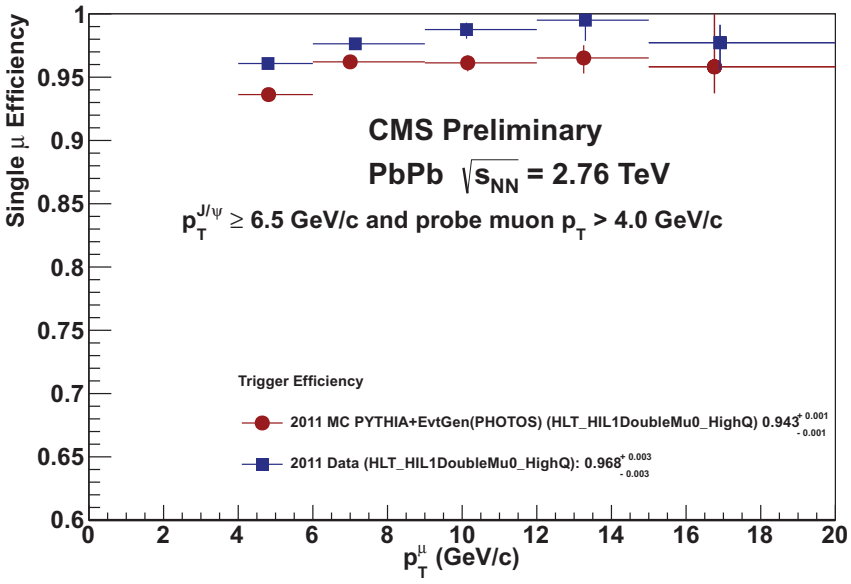

(a) Trigger efficiency dependence on muon p_{T}.

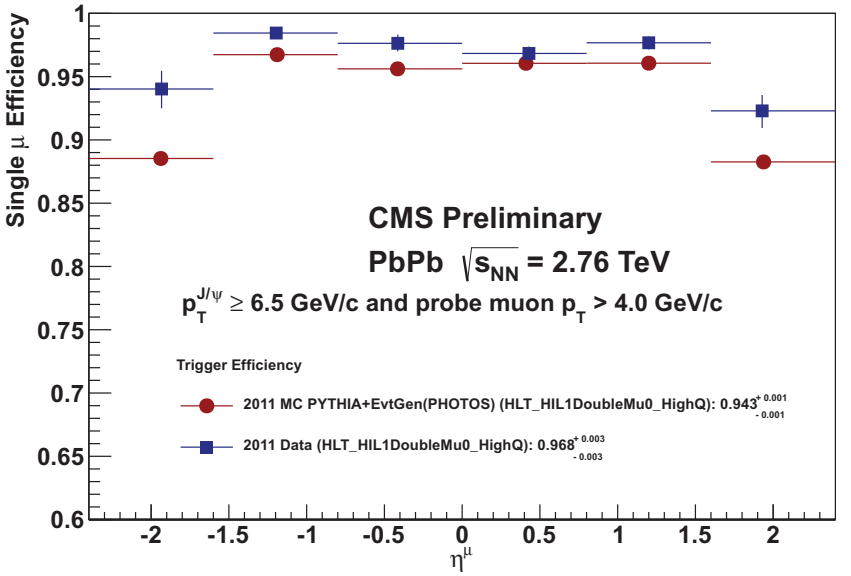

(b) Trigger efficiency dependence on muon η.

Figure 8.2: Trigger efficiency measurements with tag and probe, and dependencies on probe muon p_{T} and pseudorapidity. The efficiencies measured in the full samples are represented as blue square symbols (data) and red circles (MC simulations). The corresponding centrality integrated numerical values are displayed for both data and simulation.

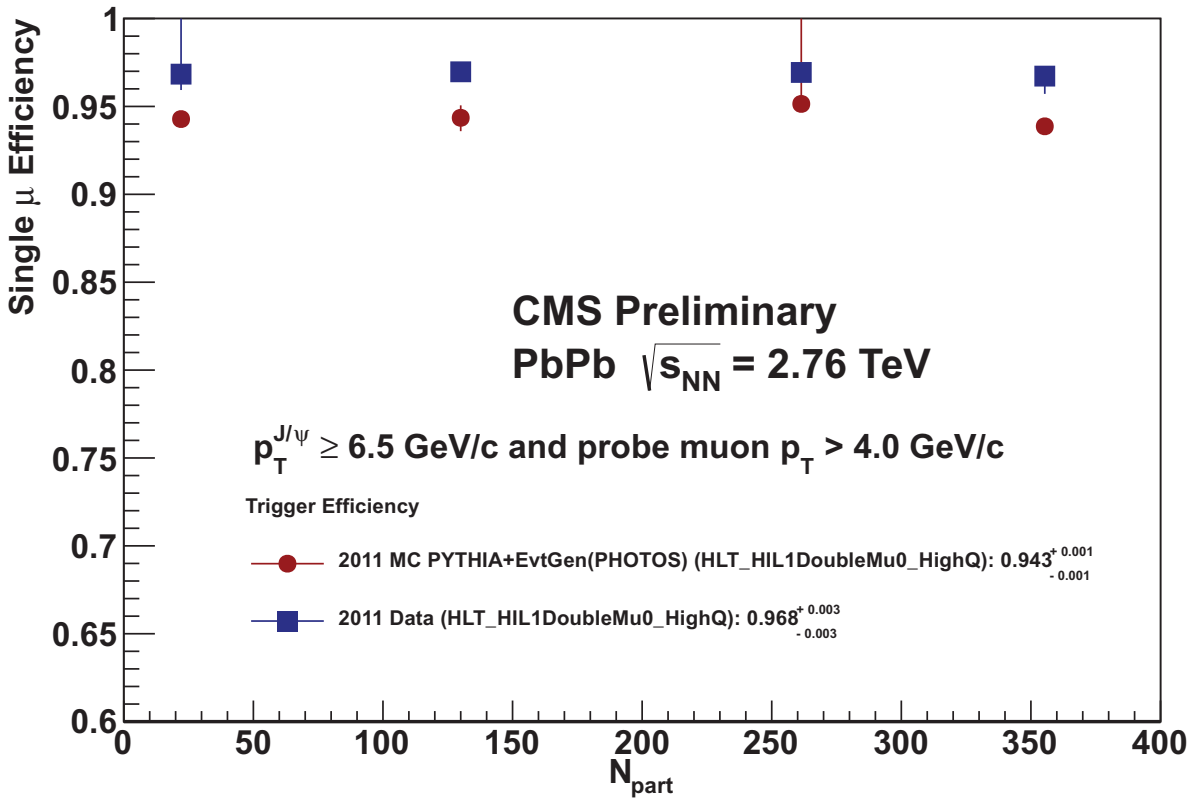

(a) Trigger efficiency dependence on event centrality.

Figure 8.3: Trigger efficiency measurements with tag and probe, and dependencies on event centrality. The efficiencies measured in the full samples are represented as blue square symbols (data) and red circles (MC simulations). The corresponding centrality integrated numerical values are displayed for both data and simulation.

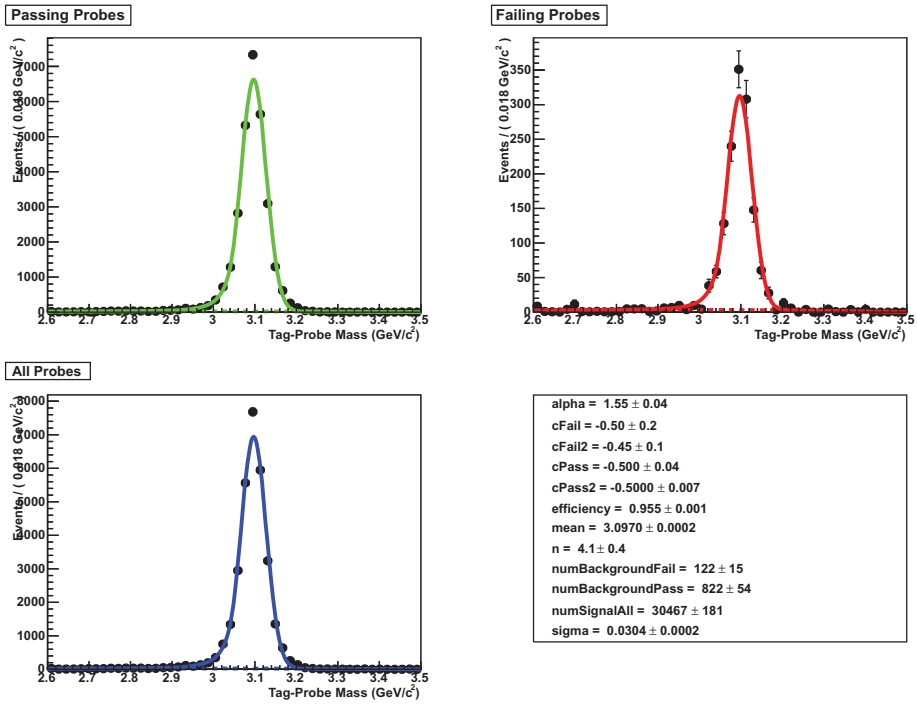

(a) Data

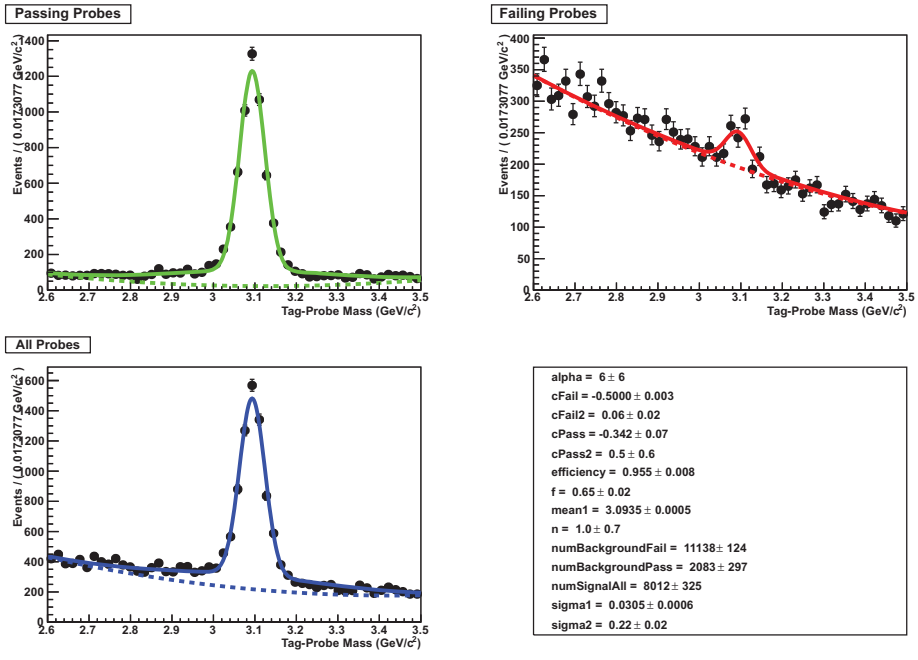

(b) Simulation

Figure 8.4: Examples of T&P pair mass fits for the muon identification efficiency in MC and data.

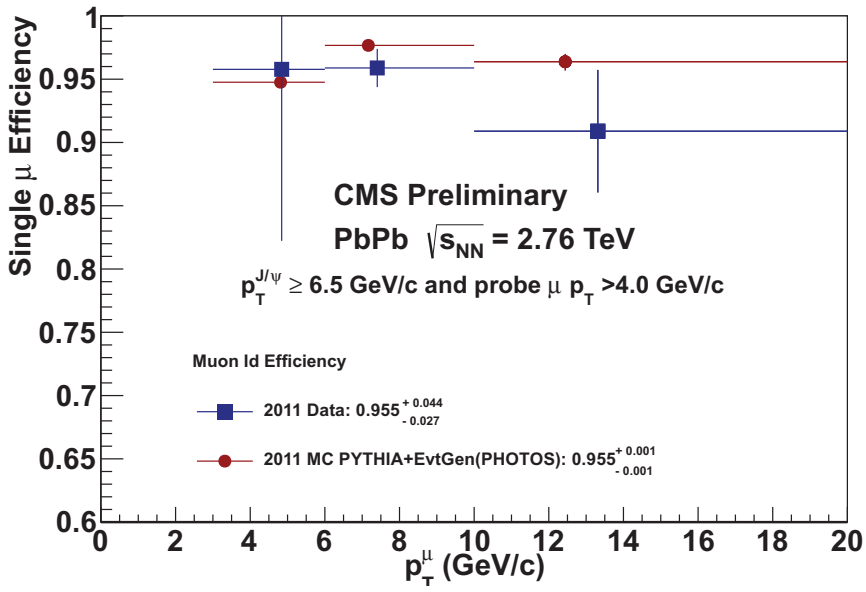

(a) Muon id efficiency dependence on muon p_{T}.

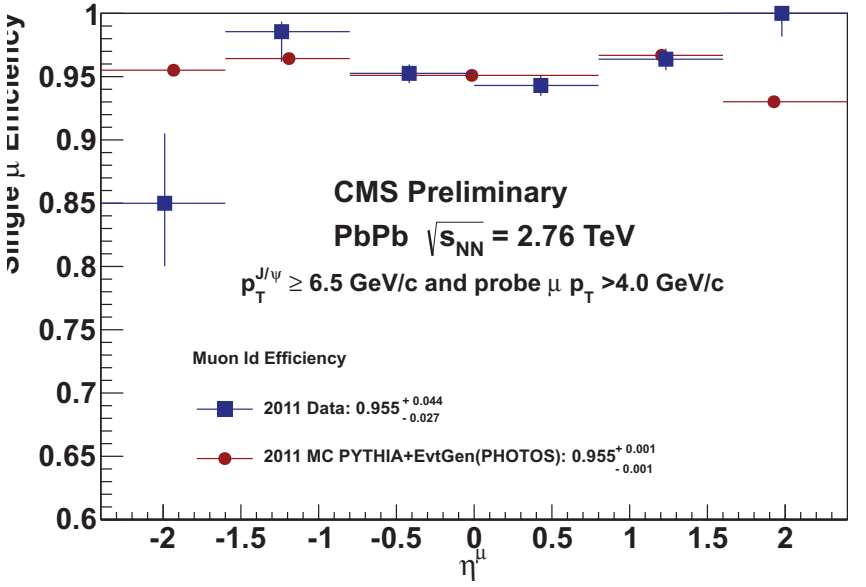

(b) Muon id efficiency dependence on muon η.

Figure 8.5: Muon identification efficiency measurements with tag and probe, and dependencies on probe muon p_{T} and pseudorapidity. The efficiencies measured in the full samples are represented as blue square symbols (data) and red circles (MC simulations). The corresponding centrality integrated numerical values are displayed for both data and simulation.

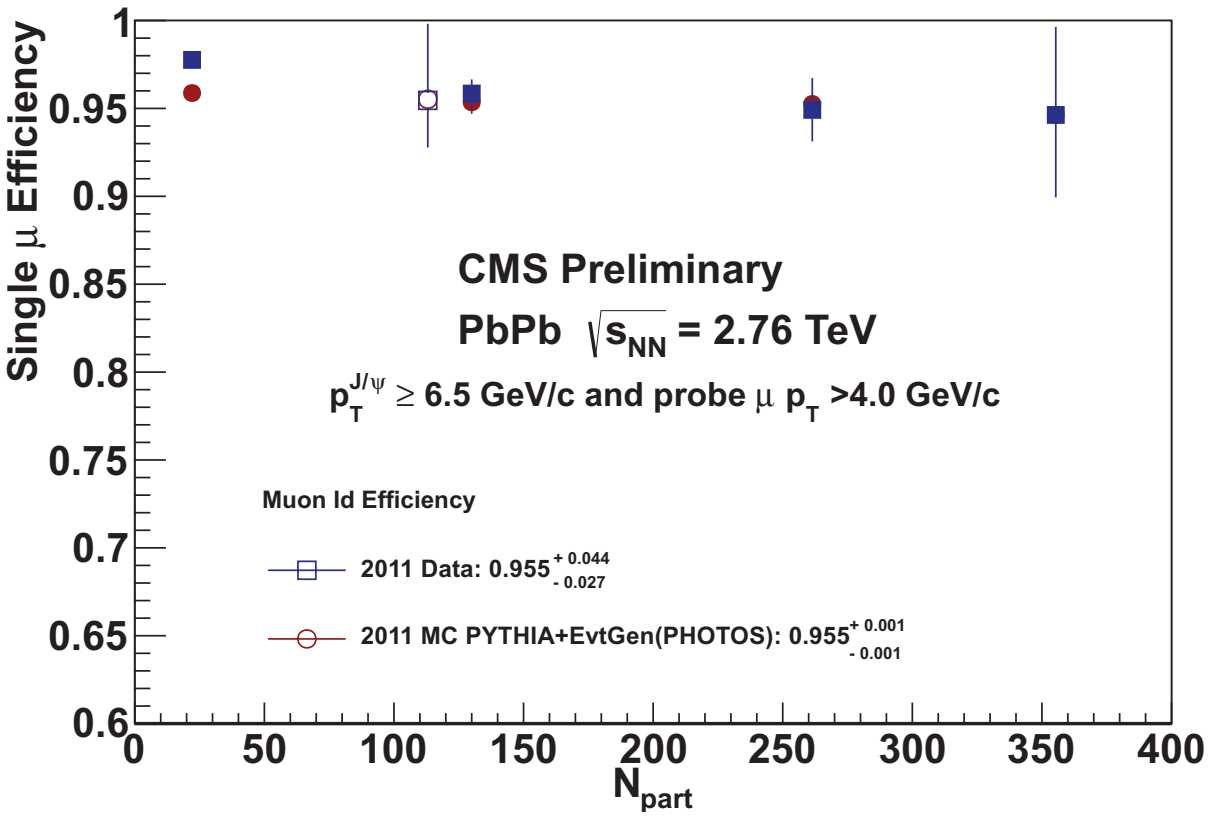

(a) Muon id efficiency dependence on event centrality.

Figure 8.6: Muon identification efficiency measurements with tag and probe and dependencies on event centrality. The efficiencies measured in the full samples are represented as blue square symbols (data) and red circles (MC simulations). The corresponding centrality integrated numerical values are displayed for both data and simulation. The open symbols are the centrality integrated values.

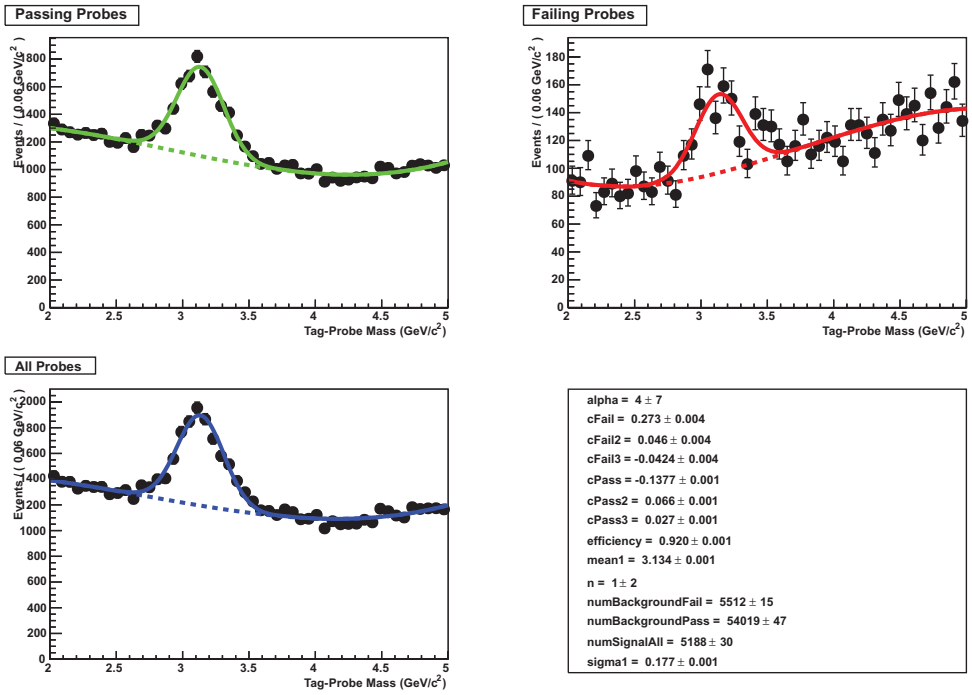

(a) Data

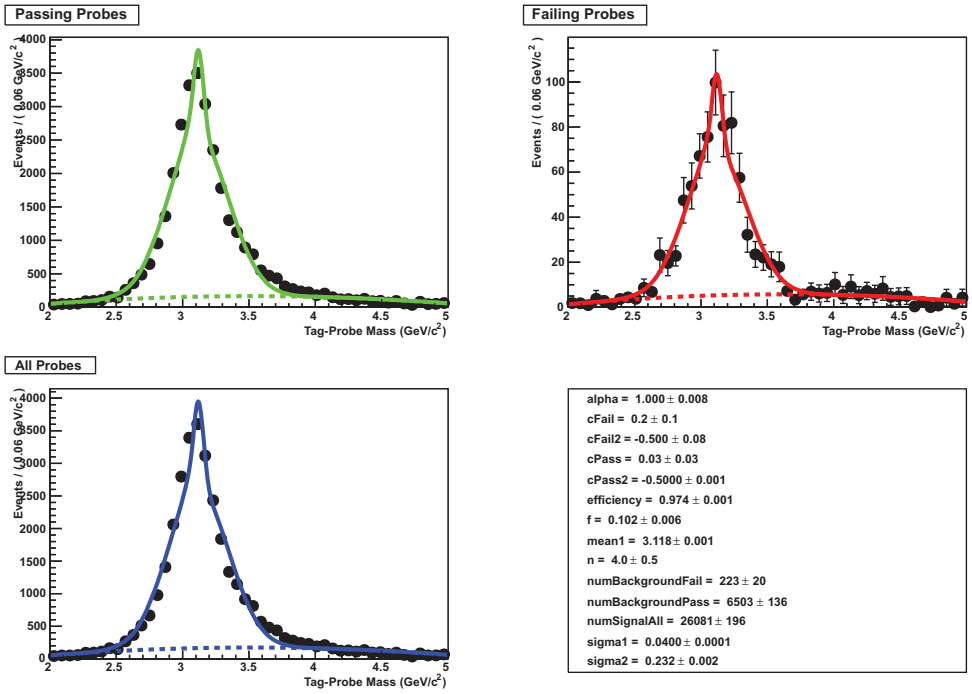

(b) Simulation

Figure 8.7: Examples of T&P pair mass fits for the inner tracking efficiency.

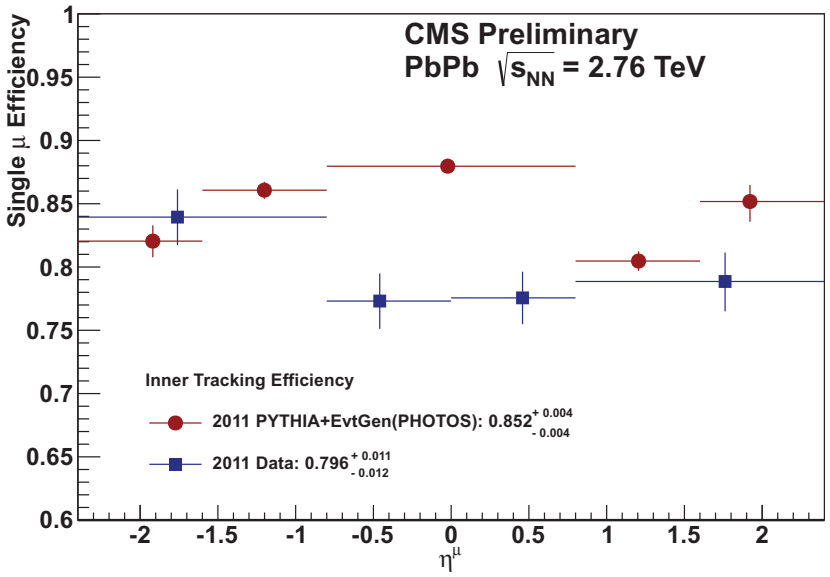

(a) Tracking efficiency dependence on muon p_{T}.

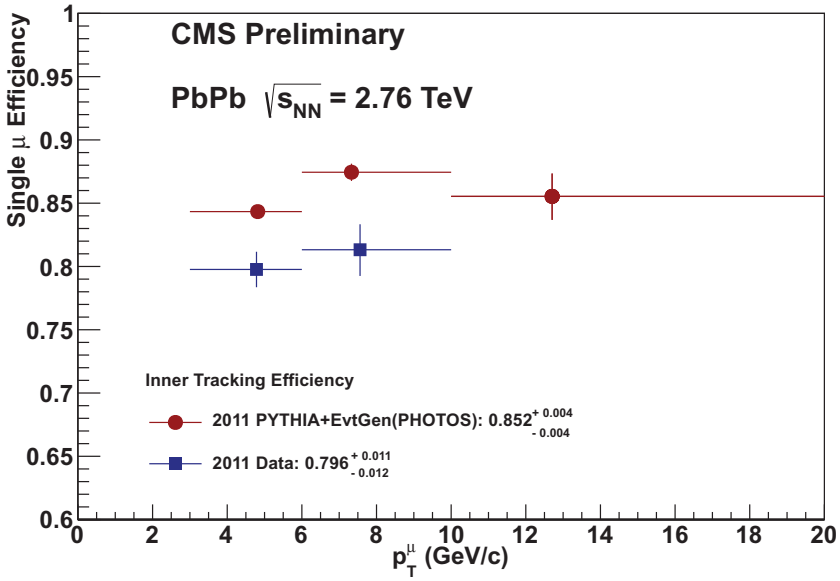

(b) Tracking efficiency dependence on muon η.

Figure 8.8: Tracking efficiency measurements with tag and probe, and dependencies on probe muon p_{T} and pseudorapidity. The efficiencies measured in the full samples are represented as blue square symbols (data) and red circles (MC simulations). The corresponding centrality integrated numerical values are displayed for both data and simulation.

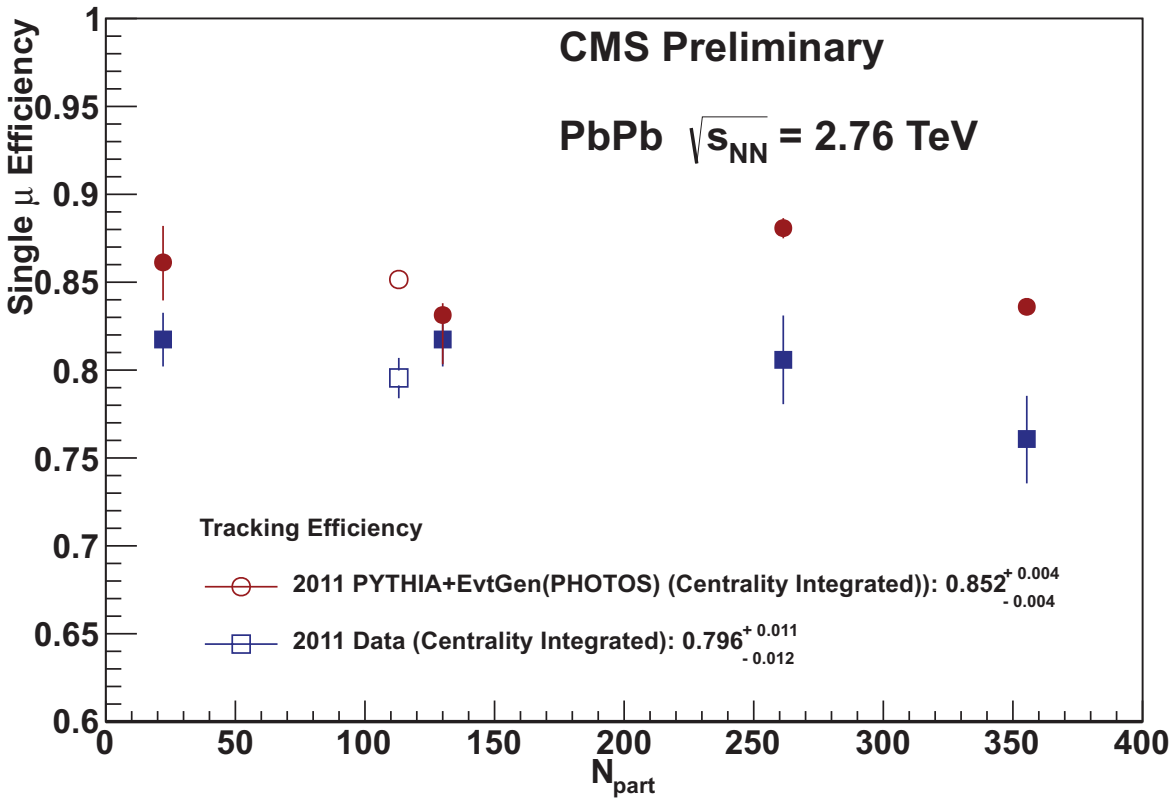

(a) Tracking efficiency dependence on event centrality.

Figure 8.9: Tracking efficiency measurements with tag and probe, and dependencies on event centrality. The efficiencies measured in the full samples are represented as blue square symbols (data) and red circles (MC simulations). The corresponding centrality integrated numerical values are displayed for both data and simulation. The open symbols are the centrality integrated values.

Chapter 9

Upper Limits

The $\Upsilon(3S)$ peak is not significantly observed in the mass spectrum in the PbPb data, as shown in Fig. 9.1. The significance of $\Upsilon(3S)$ peak is $0.86\,\sigma$, evaluated from the profile likelihood ratio. In this section we quantify the relative suppression of the 3S signal state.

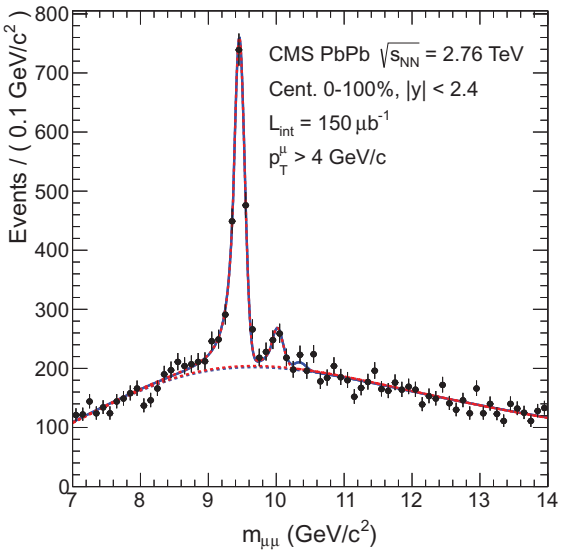

Figure 9.1: $\Upsilon(3S)$ significance, estimated via likelihood ratio, by allowing and disallowing $\Upsilon(3S)$ pdf in two fits.

In some of the centrality bins the data show large downward fluctuations of the background yielding negative yields for the signal $\Upsilon(3S)$. We proceed then to set upper limits for the 3S signal.

Approximate methods of confidence interval construction, in particular, the likelihood-ratio method, are often used in order to reduce computation. However, true confidence intervals can be obtained using the original (defining) Neyman construction [47]. Therefore we opted for the unified Feldman-Cousins (FC) approach since this treatment solves the problem whether to set an upper limit or two-sided intervals if the choice is based on the data alone as in our case.

As a cross check we also present a pure frequentist approach, the *modified*, or *conservative* $\mathrm{CL_s}$ criterion. Here, we use the ratio of p-values, $\mathrm{CL_s} = \mathrm{CL_{sb}}/\mathrm{CL_b}$, instead of the numerator only, to set an upper limit on the single and double ratios involving the 3S. Finally other implementations based on 95% credible intervals are presented as cross checks.

Single ratio R_3 limits

Instead of setting upper limits for the Υ(3S) signal per se we use the single ratio of the third peak over the first peak (R_3) in PbPb as our parameter of interest. The idea of the method can be formulated in terms of hypothesis testing in a frequentist approach. (For a detailed explanation see Ref. [49]). We define H_b as the alternative hypothesis that no signal 3S is present over the background (single ratio of zero) and H_{sb} the null hypothesis that the signal is indeed present. In order to quantify the degree in which each hypotheses are favored or excluded by the experimental observation one chooses a test-statistic which ranks the possible experimental outcomes. A commonly used test statistic consists as the ratio of the likelihood function in both hypotheses: $Q = L_{sb}/L_b$. For our study, the test statistic of choice is $-2\ln Q$.

We introduce the systematic uncertainties into the model via a nuisance parameter. Variation of such a parameter corresponds to certain systematic uncertainty. The nuisance parameter is either profiled or marginalized depending on whether we are using the frequentist approach or the Bayesian one.

The computed 95% CL upper limit with FC is: $R_3 = 0.0737 \pm 0.0014$. The background-only expectations are represented by their median (dashed line) and by the 68% and 95% CL bands. The 95% CL upper limit corresponds to the point where the observed CLs crosses the 0.05 horizontal/red line.

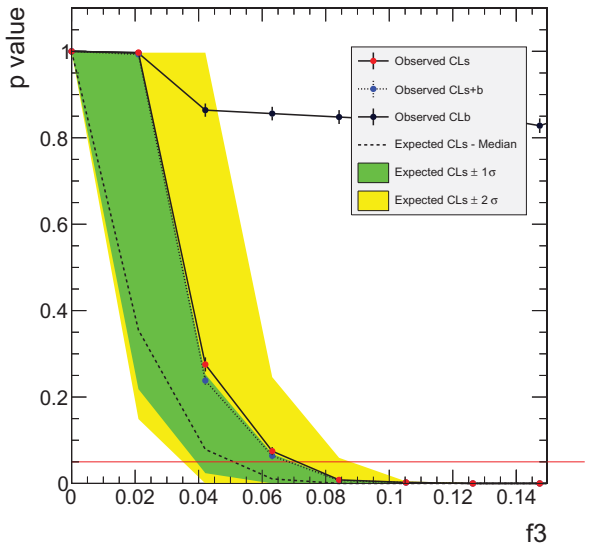

Figure 9.2: Upper limit results for R_3 (f_3 parameter on plot) using the Feldman Cousins method for the PbPb dataset. Shown is a p-value scan using 1000 pseudo experiments for each scanned point. The 95% C.L. upper limit corresponds to the point where the observed CLs crosses the 0.05 horizontal/red line.

Double ratio χ_3 limits

The same statistical method describe above are also used to set the limits for double ratio χ_3. Employing the Feldman-Cousins technique, the upper limit at 95% CL is $\chi_3 \leq 0.173 \pm 0.021$, as represented in Fig. 9.3.

Using the profile likelihood calculator, the 95% C.L. interval is $\chi_3 \in [0.042, 0.104]$, shown in Fig. 9.4. The profile likelihood method gives a lower value for the upper limit due to the fact that the systematic uncertainties are not included. The true interval is expected to be narrower.

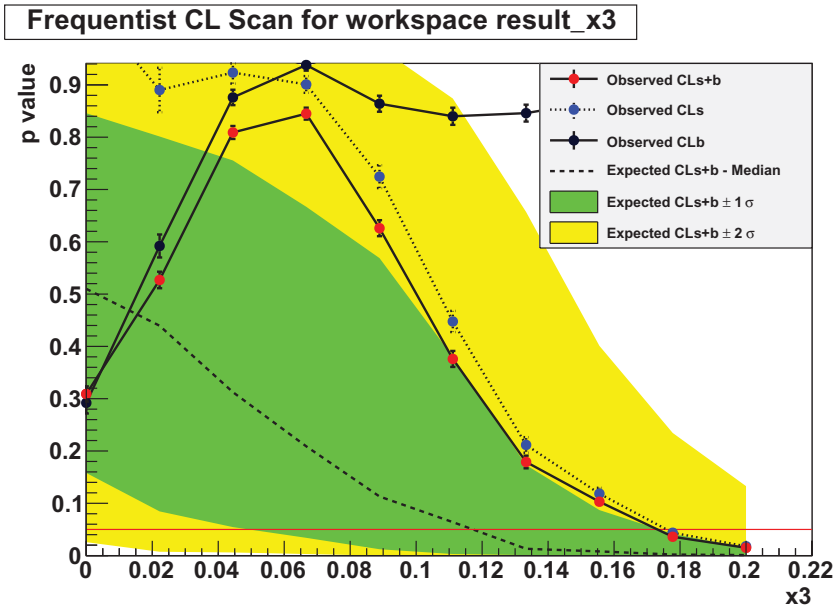

Figure 9.3: 95% interval on χ_3 with Feldman-Cousins technique after including systematic uncertainties.

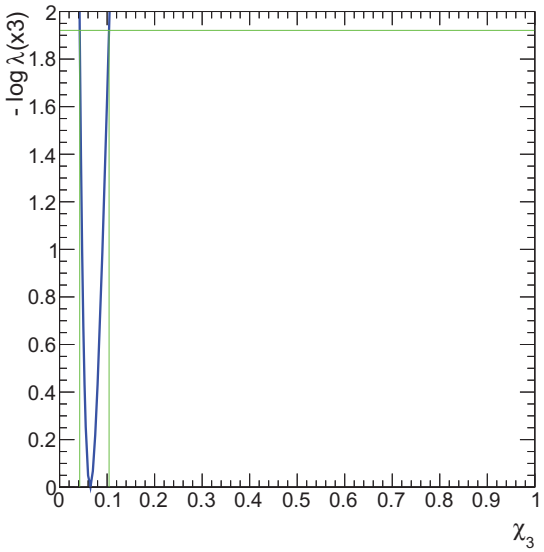

Figure 9.4: 95% interval on χ_3 with profile likelihood calculator not including systematic uncertainties.

We have used two Bayesian implementations to cross check our results. The first Bayesian calculation is using numerical integration assuming a flat prior to derive a one sided 95% credible interval and the second one is using Markov Chain Monte Carlo sampling which is based on the Metropolis-Hastings algorithm [38].

For the centrality integrated bin 0 -100% the computed upper limit for the single ratio of 3S/1S using the Feldman-Cousins method is $R_3 = 0.0695 \pm 0.0004$ which can be seen from Fig. 9.2 when the observed CL_s (red dots) crosses the horizontal threshold (red line). In Fig. 9.5 we present the upper limits for all the centrality bins as a function of the number of participants. The two lowest values for the upper limits were found in the centrality bins where we had negative yields from the fitted results. These upper limits are indeed positive as expected. Figure 9.6 shows cross checks using different implementations. Figs. 9.6(a) and 9.6(b) use CL_s and its asymptotic approximation, and Figs. 9.6(c), 9.6(d) use Bayesian numerical integration and Markov Chain Montecarlo, respectively. Notice that all results are consistent within uncertainties. Finally, in Fig. 9.7, we show Bayesian results in the 30-40% centrality bin where we found negative ratios. However, the upper limits are found to be positive, as expected. The upper limits found for the different centrality bins are tabulated in Tables 9.1 and 9.2.

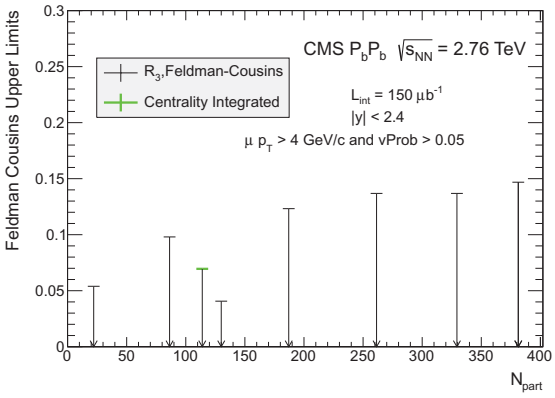

Figure 9.5: Upper limit results using the Feldman-Cousins method on R_3 in PbPb, evaluated for the different centrality bins.

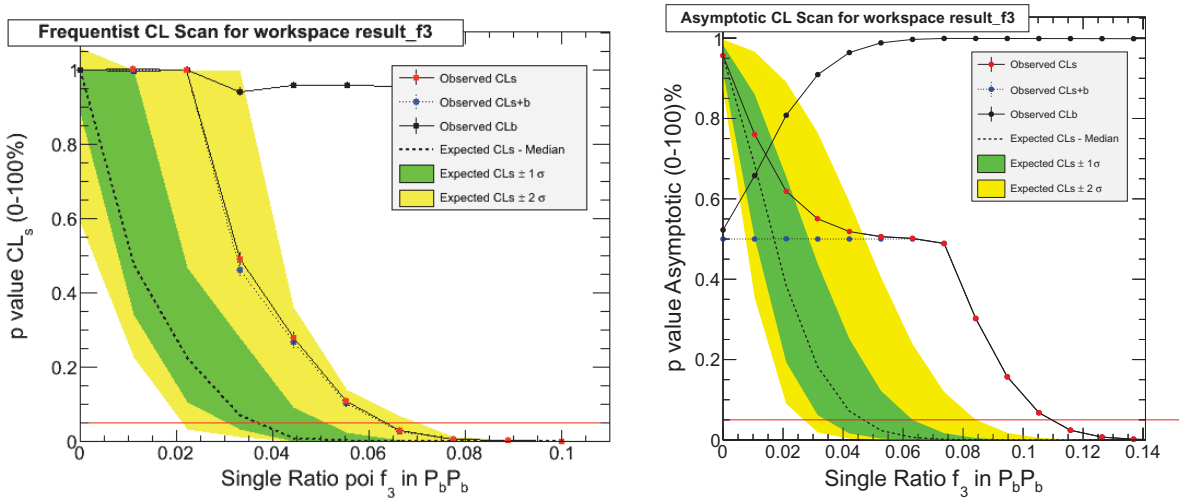

(a) Observed CLs crosses the 0.05 red line

(b) Asymptotic approach using Asimov test statistics

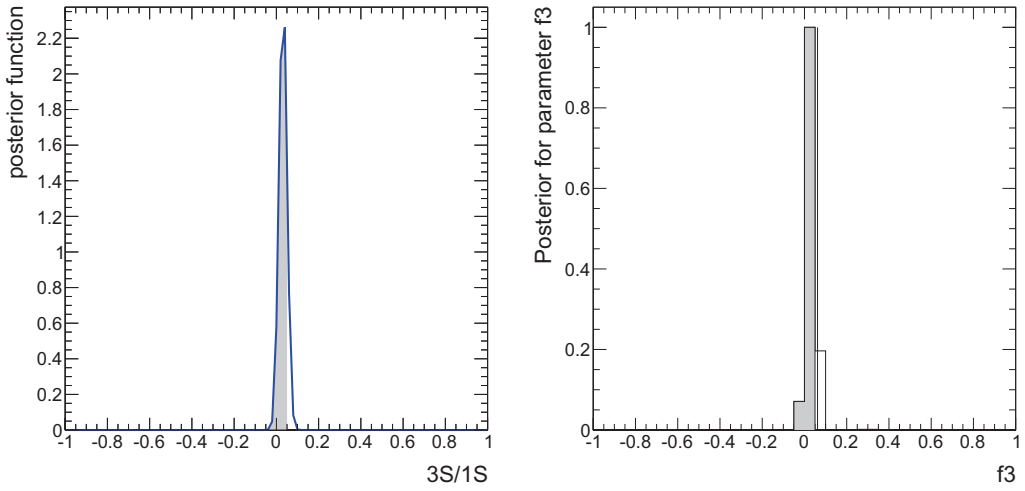

(c) Bayesian posterior

(d) Markov Chain Monte Carlo

Figure 9.6: CLs and Bayesian cross checks for the centrality integrated bin, using uniform prior. Figures 9.6(a), 9.6(b): p-value Scan with different test statistics using 1000 pseudo experiments at each point. The dotted black line shows the median (average) expected limit in the absence of a Υ(3S) signal. The green and yellow bands indicate the corresponding 68% and 95% certainty of those values; Figures 9.6(c), 9.6(d): Two different Bayesian approaches: Numerical calculation and Markov Chain Monte Carlo. On the plots the parameter f_3 correspond to the parameter of interest (poi) R_3.

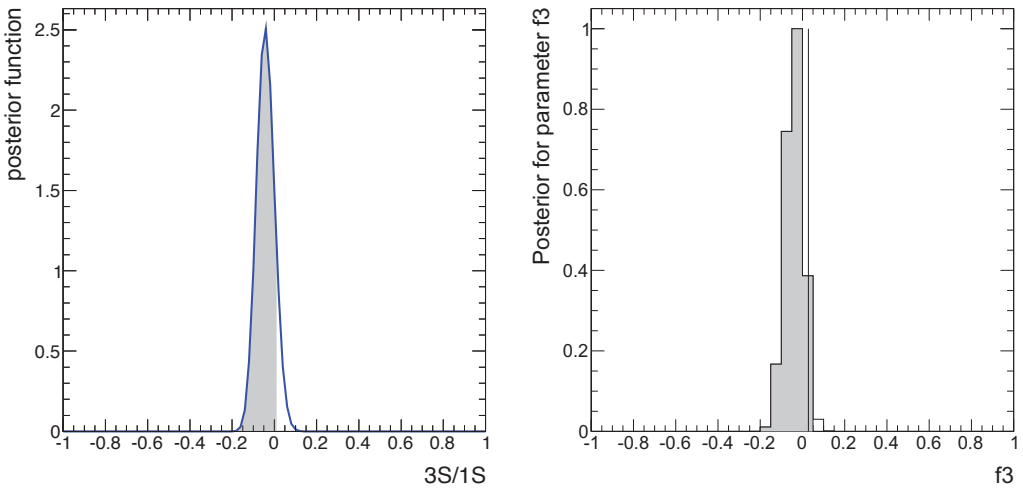

(a) Bayesian posterior

(b) MC Markov Chain posterior

Figure 9.7: Bayesian results for 40-50% centrality bin. Figures 9.7(a), 9.7(b): Bayesian Numerical Calculator and Montecarlo Markov Chain.

Table 9.1: Single-ratio upper limits.

	R_3	Feldman-Cousins	frequentist scan CL_s	asymptotic scan
0 - 5%	0.043 ± 0.051	0.147 ± 0.003	0.143 ± 0.005	0.129
5 - 10%	0.018 ± 0.055	0.1368 ± 0.0009	0.2222 ± 0.0002	0.124
10 - 20%	0.0062 ± 0.0352	0.1390 ± 0.0009	0.3129 ± 0.0005	0.074
20 - 30%	0.052 ± 0.036	0.1232 ± 0.0006	0.110 ± 0.0003	0.11
30 - 40%	-0.046 ± 0.045	0.0407 ± 0.0001	0.065 ± 0.011	0.063
40 - 50%	0.23 ± 0.070	0.0980 ± 0.0003	0.364 ± 0.003	0.35
50 - 100%	-0.069 ± 0.061	0.054 ± 0.0002	0.081 ± 0.005	0.084
0 - 100%	0.032 ± 0.019	0.0695 ± 0.0004	0.0638 ± 0.00006	0.0631

Table 9.2: Single-ratio credible intervals: Bayesian cross checks.

	R3	Bayesian calculator	MCMC
0 - 5%	0.043 ± 0.051	$[-1, 0.12]$	$[-1, 0.14]$
5 - 10%	0.018 ± 0.055	$[-1, 0.091]$	$[-1, 0.47]$
10 - 20%	0.0062 ± 0.0352	$[-1, 0.051]$	$[-1, 0.070]$
20 - 30%	0.052 ± 0.036	$[-1, 0.091]$	$[-1, 0.11]$
30 - 40%	-0.046 ± 0.045	$[-1, 0.010]$	$[-1, 0.028]$
40 - 50%	0.23 ± 0.070	$[-1, 0.33]$	$[-1, 0.41]$
50 - 100%	-0.069 ± 0.061	$[-1, 0.010]$	$[-1, 0.062]$
0 - 100%	0.032 ± 0.019	$[-1, 0.051]$	$[-1, 0.062]$

Chapter 10

Systematics

In this section, we gather the systematic uncertainties associated to the estimates of the efficiencies and their ratios. In particular, the effect of possible variations of the transverse momenta and rapidity distributions, and of the unknown polarizations, are estimated.

Momentum and rapidity shape

Since the efficiency depends on p_{T} and y, uncertainties in the predicted distributions for these variables can lead to a systematic uncertainty in the average efficiency over a p_{T} or y bin. To estimate these uncertainties, the shapes of the generated MC p_{T} and y distributions are varied by applying a weight that increases linearly from 0.7 to 1.3 over the range $0 < |y| < 2.4$ and p_{T} ¡ 20 GeV/c.

We set the following notation. V denotes the efficiency for pp and W is efficiency for PbPb. $V-(V+)$ or $W-(W+)$ are the efficiencies obtained by a change in the distribution by -30% (+30%). V/W is central efficiency ratio in a centrality bin. The systematic error due to shape variations is $(V-/W+-V+/W-)$ in that bin.

Tables 10.1 and 10.2 show the central value of efficiencies and values after p_{T} and rapidity shape variations for Υ(1S) and Υ(2S), in the PbPb and pp Monte Carlo.

Tables 10.3 and 10.4 show the systematic uncertainty on the single ratio and the double ratio arising from the p_{T} and rapidity shape variations for PbPb and pp Montecarlo.

Tables 10.5 and 10.6 show the systematic uncertainty on the efficiency ratio PbPb vs pp for Υ(1S) and Υ(2S) due to p_{T} and rapidity variations. Systematic uncertainty values are found between 2.7% to 5.2% for Υ(1S) and 2.2% to 5.7% for Υ(2S).

Table 10.1: Reconstruction efficiency for Υ(1S) with variations in p_{T} and rapidity shape

Centrality	Υ(1S)	Υ(1S) p_{T} +30%	Υ(1S) p_{T} -30%	Υ(1S) y +30%	Υ(1S) y-30%
$[0-5\%]$	$46.6 \pm 0.6\%$	$46.9 \pm 0.6\%$	$46.5 \pm 0.7\%$	$46.2 \pm 0.7\%$	$47.1 \pm 0.6\%$
$[5-10\%]$	$47.1 \pm 0.7\%$	$47.5 \pm 0.6\%$	$46.9 \pm 0.7\%$	$46.3 \pm 0.7\%$	$47.9 \pm 0.7\%$
$[10-20\%]$	$49.2 \pm 0.5\%$	$49.4 \pm 0.4\%$	$49.1 \pm 0.5\%$	$48.8 \pm 0.5\%$	$49.6 \pm 0.5\%$
$[20-30\%]$	$49.1 \pm 0.5\%$	$49.5 \pm 0.4\%$	$48.8 \pm 0.5\%$	$48.5 \pm 0.5\%$	$49.7 \pm 0.5\%$
$[30-40\%]$	$51.0 \pm 0.4\%$	$51.3 \pm 0.4\%$	$50.7 \pm 0.5\%$	$50.5 \pm 0.5\%$	$51.5 \pm 0.5\%$
$[40-50\%]$	$51.7 \pm 0.5\%$	$52.0 \pm 0.4\%$	$51.4 \pm 0.5\%$	$51.2 \pm 0.5\%$	$52.1 \pm 0.5\%$
$[50-100\%]$	$51.6 \pm 0.3\%$	$52.0 \pm 0.2\%$	$51.2 \pm 0.3\%$	$51.2 \pm 0.3\%$	$52.0 \pm 0.3\%$
$[50-60\%]$	$51.1 \pm 0.4\%$	$51.5 \pm 0.4\%$	$50.8 \pm 0.5\%$	$50.8 \pm 0.5\%$	$51.5 \pm 0.5\%$
$[60-100\%]$	$52.1 \pm 0.3\%$	$52.6 \pm 0.2\%$	$51.7 \pm 0.3\%$	$51.7 \pm 0.3\%$	$52.5 \pm 0.3\%$
$[0-100\%]$	$48.6 \pm 0.2\%$	$48.9 \pm 0.2\%$	$48.4 \pm 0.2\%$	$48.1 \pm 0.2\%$	$49.1 \pm 0.2\%$
pp	$48.7 \pm 0.1\%$	$49.2 \pm 0.1\%$	$48.3 \pm 0.1\%$	$48.1 \pm 0.1\%$	$49.3 \pm 0.1\%$

Table 10.2: Reconstruction efficiency for Υ(2S) with variations in p_{T} and rapidity shapes

Centrality	Υ(2S)	Υ(2S) p_{T} +30%	Υ(2S) p_{T} -30%	Υ(2S) y +30%	Υ(2S) y-30%
$[0-5\%]$	$47.3 \pm 0.8\%$	$47.4 \pm 0.8\%$	$47.2 \pm 0.8\%$	$46.7 \pm 0.8\%$	$47.9 \pm 0.8\%$
$[5-10\%]$	$48.0 \pm 0.8\%$	$48.2 \pm 0.7\%$	$47.9 \pm 0.6\%$	$47.4 \pm 0.8\%$	$48.6 \pm 0.8\%$
$[10-20\%]$	$49.0 \pm 0.5\%$	$49.2 \pm 0.5\%$	$48.9 \pm 0.6\%$	$48.5 \pm 0.6\%$	$49.6 \pm 0.5\%$
$[20-30\%]$	$50.2 \pm 0.5\%$	$50.3 \pm 0.4\%$	$50.1 \pm 0.5\%$	$49.7 \pm 0.5\%$	$50.6 \pm 0.5\%$
$[30-40\%]$	$51.1 \pm 0.5\%$	$51.3 \pm 0.4\%$	$51.0 \pm 0.5\%$	$50.6 \pm 0.5\%$	$51.6 \pm 0.5\%$
$[40-50\%]$	$51.5 \pm 0.5\%$	$51.7 \pm 0.4\%$	$51.3 \pm 0.5\%$	$51.1 \pm 0.5\%$	$51.8 \pm 0.5\%$
$[50-100\%]$	$53.0 \pm 0.3\%$	$53.2 \pm 0.3\%$	$52.8 \pm 0.3\%$	$52.6 \pm 0.3\%$	$53.4 \pm 0.3\%$
$[50-60\%]$	$53.0 \pm 0.4\%$	$53.2 \pm 0.4\%$	$52.8 \pm 0.5\%$	$52.6 \pm 0.4\%$	$53.4 \pm 0.5\%$
$[60-100\%]$	$53.0 \pm 0.3\%$	$53.2 \pm 0.4\%$	$52.9 \pm 0.3\%$	$52.5 \pm 0.3\%$	$53.5 \pm 0.3\%$
$[0-100\%]$	$49.3 \pm 0.2\%$	$49.5 \pm 0.2\%$	$49.2 \pm 0.2\%$	$48.8 \pm 0.2\%$	$49.9 \pm 0.2\%$
pp	$49.4 \pm 0.2\%$	$49.8 \pm 0.2\%$	$49.1 \pm 0.2\%$	$48.7 \pm 0.2\%$	$50.1 \pm 0.2\%$

Table 10.3: Systematic uncertainty on the single ratio R_2 using p_T and rapidity shape variations. (All numbers with % are relative errors).

CentBin	R_2 Eff Ratio	p_T Syst	y Syst	Total
0-5%	1.02	1.28%	4.46%	4.64%
5-10%	1.02	1.89%	5.9%	6.2%
10-20%	0.996	1.22%	3.87%	4.06%
20-30%	1.02	1.82%	4.24%	4.61%
30-40%	1.0	1.76%	3.92%	4.3%
40-50%	0.996	1.94%	3.1%	3.66%
50-100%	1.03	2.31%	3.06%	3.83%
0-100%	1.01	1.64%	4.29%	4.59%
pp	1.02	3.26%	5.3%	6.2%

Table 10.4: Systematic uncertainty on the double ratio χ_2 using p_T and rapidity shape variations. (All numbers in % are relative uncertainties).

CentBin	χ_2 Eff Ratio	p_T Syst	y Syst	Total
0-5%	0.999	0.864%	0.978%	1.30%
5-10%	0.995	1.090%	0.532%	1.21%
10-20%	1.022	0.413%	0.952%	1.04%
20-30%	0.992	1.480%	0.284%	1.51%
30-40%	1.010	0.997%	0.357%	1.06%
40-50%	1.020	0.785%	0.012%	0.786%
50-100%	0.988	1.260%	0.337%	1.30%
0-100%	1.000	0.851%	0.542%	1.01%

Table 10.5: Systematic uncertainty on Υ(1S) R_{AA} using p_T and rapidity shape variations. (All numbers in % are relative uncertainties).

Centrality	Υ(1S) R_{AA} Eff Ratio	p_T Syst	y Syst	Total
0-5%	1.05	2.7%	4.39%	5.15%
5-10%	1.03	3.11%	5.86%	6.64%
10-20%	0.99	2.46%	4.09%	4.77%
20-30%	0.992	3.27%	4.91%	5.90%
30-40%	0.955	3.03%	4.43%	5.36%
40-50%	0.942	3.01%	4.21%	5.18%
50-100%	0.944	3.4%	4.01%	5.26%
50-60%	0.953	3.21%	3.83%	5.00%
60-100%	0.929	3.59%	4.02%	5.39%
0-100%	1.00	2.87%	4.52%	5.36%

Table 10.6: Systematic uncertainty on Υ(2S) R_{AA} using p_{T} and rapidity shape variations. (All numbers in % are relative errors).

CentBin	Υ(2S) R_{AA} EffRatio	p_{T} Syst	y Syst	Total
0-5%	1.04	1.84%	5.37%	5.68%
5-10%	1.03	2.04%	5.33%	5.71%
10-20%	1.01	2.03%	5.07%	5.46%
20-30%	0.984	1.82%	4.63%	4.98%
30-40%	0.967	2.0%	4.79%	5.19%
40-50%	0.959	2.19%	4.2%	4.74%
50-100%	0.932	2.17%	4.34%	4.86%
50-60%	0.932	2.17%	4.16%	4.69%
50-100%	0.932	1.98%	4.72%	5.12%
0-100%	1.0	2.02%	5.06%	5.45%

Table 10.7: Reconstruction efficiency for Υ(1S) in p_{T} bins (the errors are statistical).

p_{T} (GeV/c)	Υ(1S) PbPb	Υ(1S) pp
$0 - 6.5$	$47.5 \pm 0.3\%$	$46.7 \pm 0.1\%$
$6.5 - 10$	$50.3 \pm 0.4\%$	$51.0 \pm 0.2\%$
$10 - 30$	$52.5 \pm 0.3\%$	$53.3 \pm 0.2\%$

Table 10.8: Reconstruction efficiency for Υ(2S) in p_{T} bins (the errors are statistical).

p_{T} (GeV/c)	Υ(2S) PbPb	Υ(2S) pp
$0 - 6.5$	$48.9 \pm 0.3\%$	$47.9 \pm 0.3\%$
$6.5 - 30$	$51.9 \pm 0.3\%$	$53.3 \pm 0.5\%$

Table 10.9: Reconstruction efficiency for Υ(1S) in p_{T} bins with $\pm$30% variations in p_{T} and rapidity shapes

p_{T} (GeV/c)	Υ(1S) p_{T} +30%	Υ(1S) p_{T} -30%	Υ(1S) y +30%	Υ(1S) y-30%
$[0 - 6.5]$	$47.6 \pm 0.3\%$	$47.5 \pm 0.3\%$	$47.2 \pm 0.3\%$	$47.9 \pm 0.3\%$
$[6.5 - 30]$	$51.5 \pm 0.2\%$	$51.2 \pm 0.3\%$	$50.5 \pm 0.3\%$	$52.2 \pm 0.3\%$

Table 10.10: Reconstruction efficiency for Υ(2S) in p_{T} bins with $\pm$30% variations in p_{T} and rapidity shapes

p_{T} (GeV/c)	Υ(2S) p_{T} +30%	Υ(2S) p_{T} -30%	Υ(2S) y +30%	Υ(2S) y-30%
$0-6.5$	$49.0 \pm 0.3\%$	$48.9 \pm 0.3\%$	$48.4 \pm 0.3\%$	$49.4 \pm 0.3\%$
$6.5-30$	$52.1 \pm 0.3\%$	$51.9 \pm 0.3\%$	$51.1 \pm 0.3\%$	$52.9 \pm 0.3\%$

Table 10.11: *pp* Reconstruction efficiency for Υ(1S) in p_{T} bins with $\pm$30% variations in p_{T} and rapidity shapes

p_{T} (GeV/c)	Υ(1S) p_{T} +30%	Υ(1S) p_{T} -30%	Υ(1S) y +30%	Υ(1S) y-30%
$0-6.5$	$46.9 \pm 0.1\%$	$46.7 \pm 0.1\%$	$46.4 \pm 0.1\%$	$47.2 \pm 0.1\%$
$6.5-30$	$52.3 \pm 0.1\%$	$52.0 \pm 0.1\%$	$51.3 \pm 0.1\%$	$52.9 \pm 0.1\%$

Table 10.12: *pp* Reconstruction efficiency for Υ(2S) in p_{T} bins with $\pm$30% variations in p_{T} and rapidity shapes

p_{T} (GeV/c)	Υ(2S) p_{T} +30%	Υ(2S) p_{T} -30%	Υ(2S) y +30%	Υ(2S) y-30%
$0-6.5$	$48.0 \pm 0.3\%$	$47.9 \pm 0.3\%$	$47.3 \pm 0.3\%$	$48.6 \pm 0.3\%$
$6.5-30$	$53.5 \pm 0.5\%$	$53.2 \pm 0.5\%$	$52.5 \pm 0.5\%$	$54.2 \pm 0.5\%$

Table 10.13: Reconstruction efficiency for Υ(1S) in rapidity bins

rapidity	Υ(1S) PbPb	Υ(1S) *pp*
$0-1.0$	$50.8 \pm 0.3\%$	$51.0 \pm 0.1\%$
$1.0-2.4$	$46.2 \pm 0.3\%$	$46.2 \pm 0.1\%$

Table 10.14: Reconstruction efficiency for Υ(2S) in rapidity bins

rapidity	Υ(2S) PbPb	Υ(2S) *pp*
$0-1.0$	$51.3 \pm 0.3\%$	$52.1 \pm 0.3\%$
$1.0-2.4$	$47.1 \pm 0.3\%$	$46.5 \pm 0.3\%$

Table 10.15: Reconstruction efficiency for Υ(1S) in rapidity bins with $\pm$30% variations in p_{T} and rapidity shapes

rapidity	Υ(1S) p_{T} +30%	Υ(1S) p_{T} -30%	Υ(1S) y +30%	Υ(1S) y-30%
$0 - 1.0$	$51.3 \pm 0.3\%$	$50.5 \pm 0.3\%$	$50.9 \pm 0.3\%$	$50.8 \pm 0.3\%$
$1.0 - 2.4$	$46.4 \pm 0.3\%$	$46.2 \pm 0.3\%$	$45.9 \pm 0.3\%$	$46.8 \pm 0.3\%$

Table 10.16: Reconstruction efficiency for Υ(2S) in rapidity bins with $\pm$30% variations in p_{T} and rapidity shapes

rapidity	Υ(2S) p_{T} +30%	Υ(2S) p_{T} -30%	Υ(2S) y +30%	Υ(2S) y-30%
$0 - 1.0$	$51.7 \pm 0.3\%$	$51.1 \pm 0.3\%$	$51.4 \pm 0.3\%$	$51.4 \pm 0.3\%$
$1.0 - 2.4$	$47.2 \pm 0.3\%$	$47.1 \pm 0.4\%$	$46.8 \pm 0.3\%$	$47.8 \pm 0.3\%$

Table 10.17: *pp* Reconstruction efficiency for Υ(1S) in rapidity bins with ±30% variations in p_{T} and rapidity shapes

rapidity	Υ(1S) p_{T} +30%	Υ(1S) p_{T} -30%	Υ(1S) y +30%	Υ(1S) y-30%
$0-1.0$	$51.7 \pm 0.1\%$	$50.6 \pm 0.1\%$	$51.1 \pm 0.1\%$	$51.0 \pm 0.1\%$
$1.0-2.4$	$46.5 \pm 0.5\%$	$46.0 \pm 0.1\%$	$45.8 \pm 0.1\%$	$46.8 \pm 0.1\%$

Table 10.18: *pp* Reconstruction efficiency for Υ(2S) in rapidity bins with ±30% variations in p_{T} and rapidity shapes

rapidity	Υ(2S) p_{T} +30%	Υ(2S) p_{T} -30%	Υ(2S) y +30%	Υ(2S) y-30%
$0-1.0$	$52.6 \pm 0.3\%$	$51.8 \pm 0.3\%$	$52.2 \pm 0.3\%$	$52.1 \pm 0.3\%$
$1.0-2.4$	$46.8 \pm 0.4\%$	$46.2 \pm 0.4\%$	$46.0 \pm 0.3\%$	$47.2 \pm 0.3\%$

Table 10.19: Systematic uncertainty on the Υ(1S) R_{AA} in p_{T} bins with ±30% variations in p_{T} and rapidity shapes

p_{T} (GeV/c)	Eff Ratio	p_{T} Syst %	y Syst%	Total%
$0-6.5$	0.98	0.638%	3.4%	3.46%
$6.5-30$	1.02	1.35%	6.38%	6.52%

Table 10.20: Systematic uncertainty for Υ(2S) R_{AA} in p_{T} bins with $\pm 30\%$ variations in p_{T} and rapidity shapes.

p_{T} (GeV/c)	Eff Ratio	p_{T} Syst %	y Syst%	Total%
$0 - 6.5$	0.98	0.413%	4.76%	4.78%
$6.5 - 30$	1.024	0.946%	6.64%	6.71%

Table 10.21: Systematic uncertainty on the double ratio in p_{T} bins with $\pm 30\%$ variations in p_{T} and rapidity shapes.

p_{T} (GeV/c)	CF	p_{T} Syst %	y Syst%	Total%
$0 - 6.5$	$0.996 \pm 0.004\%$	0.227%	1.37%	1.39%
$6.5 - 30$	$1.010 \pm 0.001\%$	0.396%	0.261%	0.474%

Table 10.22: Systematic uncertainty for Υ(1S) R_{AA} in rapidity bins with $\pm 30\%$ variations in p_{T} and rapidity shapes.

rapidity	Eff Ratio	P p_{T} yst %	y Syst%	Total%
$0 - 1.0$	1.0	3.17%	0.397%	3.2%
$1.0 - 2.4$	1.0	1.51%	4.54%	4.79%

Table 10.23: Systematic uncertainty on the Υ(2S) R_{AA} in rapidity bins with $\pm 30\%$ variations in p_{T} and rapidity shapes.

rapidity	Eff Ratio	p_{T} Syst %	y Syst%	Total%
$0 - 1.0$	1.02	2.7%	0.192%	2.71%
$1.0 - 2.4$	0.987	1.29%	4.68%	4.85%

Table 10.24: Systematic uncertainty on the double ratio in rapidity bins with ±30% variations in p_{T} and rapidity shapes.

rapidity	CF	p_{T} Syst %	y Syst%	Total%
$0-1.0$	$1.010 \pm 0.003\%$	0.404%	0.197%	0.449%
$1.0-2.4$	$0.987 \pm 0.004\%$	0.223%	0.178%	0.285%

Tables 10.7 and 10.8 shows the reconstruction efficiencies for Υ(1S) and Υ(2S) in p_{T} bins.

Tables 10.9 and 10.10 shows the reconstruction efficiencies for Υ(1S) and Υ(2S) in p_{T} bins with ± 30 % variation in p_{T} and rapidity shape.

Tables 10.11 and 10.12 shows the pp reconstruction efficiencies for Υ(1S) and Υ(2S) in p_{T} bins with ± 30 % variation in p_{T} and rapidity shape.

Tables 10.13 and 10.14 shows the reconstruction efficiencies for Υ(1S) and Υ(2S) in rapidity bins.

Tables 10.15 and 10.16 shows the reconstruction efficiencies for Υ(1S) and Υ(2S) in rapidity bins with ± 30 % variation in p_{T} and rapidity shape.

Tables 10.17 and 10.18 shows the reconstruction efficiencies for Υ(1S) and Υ(2S) in rapidity bins with ± 30 % variation in p_{T} and rapidity shape.

Tables 10.19 and 10.20 shows the systematic uncertainty on the Υ(1S) R_{AA} and Υ(2S) R_{AA} in p_{T} bins.

Tables 10.22 and 10.23 shows the systematic uncertainty on the Υ(1S) R_{AA} and Υ(2S) R_{AA} in rapidity bins.

Tables 10.21 and 10.24 shows the systematic uncertainty on the double ratio in p_{T} and rapidity bins.

Unknown polarization

The impact of the unknown production polarization on the efficiency ratios is studied for extreme (transverse, longitudinal) polarization scenarios in the Collins-Soper (w2,w3) and helicity (w4,w5) reference frames.

Tables 10.25 and 10.26 show the central values of the efficiencies and values after different polarizations for Υ(1S) and Υ(2S) evaluated in PbPb MC and *pp* MC. Table 10.27 and Table 10.28 shows the corresponding variations on the efficiency ratio from different polarizations. These are about 0.5% and negligible compared to other sources.

Note that possible different polarization for PbPb and *pp* are not considered. These would induce modifications to the acceptance which would not cancel in the ratios. The effect of such possible modifications of the polarization in PbPb relative to *pp* are considered as part of the physics studied and are incorporated in the measured ratios.

Table 10.25: Reconstruction efficiency for Υ(1S) in different polarization scenarios.

Centrality	Υ(1S)	Υ(1S) w2	Υ(1S) w3	Υ(1S) w4	Υ(1S) w5
$0-5\%$	$46.6 \pm 0.6\%$	$46.4 \pm 0.6\%$	$47.0 \pm 0.7\%$	$46.8 \pm 0.6\%$	$46.4 \pm 0.7\%$
$5-10\%$	$47.1 \pm 0.7\%$	$46.9 \pm 0.7\%$	$47.4 \pm 0.7\%$	$47.3 \pm 0.6\%$	$46.9 \pm 0.7\%$
$10-20\%$	$49.2 \pm 0.5\%$	$49.0 \pm 0.5\%$	$49.4 \pm 0.5\%$	$49.2 \pm 0.4\%$	$49.2 \pm 0.5\%$
$20-30\%$	$49.1 \pm 0.5\%$	$49.0 \pm 0.4\%$	$49.3 \pm 0.5\%$	$49.2 \pm 0.4\%$	$48.9 \pm 0.5\%$
$30-40\%$	$51.0 \pm 0.4\%$	$50.8 \pm 0.4\%$	$51.2 \pm 0.5\%$	$51.0 \pm 0.4\%$	$50.9 \pm 0.5\%$
$40-50\%$	$51.7 \pm 0.4\%$	$51.5 \pm 0.5\%$	$51.9 \pm 0.5\%$	$51.8 \pm 0.4\%$	$51.5 \pm 0.5\%$
$50-100\%$	$51.6 \pm 0.3\%$	$51.4 \pm 0.3\%$	$51.9 \pm 0.3\%$	$51.7 \pm 0.2\%$	$51.4 \pm 0.3\%$
$0-100\%$	$48.6 \pm 0.2\%$	$48.4 \pm 0.2\%$	$48.8 \pm 0.2\%$	$48.7 \pm 0.2\%$	$48.5 \pm 0.2\%$
pp	$48.7 \pm 0.1\%$	$48.5 \pm 0.1\%$	$48.9 \pm 0.1\%$	$48.8 \pm 0.1\%$	$48.5 \pm 0.1\%$

Trigger efficiency in simulation

The latest signal MC simulation for *pp* employed a trigger table which does not reproduce the trigger paths used online in early 2011. Some difficulties arose re-running the old menu in the more recent software release (related to apparent incompatibilities between menu, release and global tag).

Table 10.26: Reconstruction efficiency for Υ(2S) with different polarization scenarios.

Centrality	Υ(2S)	Υ(2S) w2	Υ(2S) w3	Υ(2S) w4	Υ(2S) w5
$0-5\%$	$47.3 \pm 0.8\%$	$47.1 \pm 0.8\%$	$47.5 \pm 0.8\%$	$47.3 \pm 0.8\%$	$47.3 \pm 0.8\%$
$5-10\%$	$48.0 \pm 0.8\%$	$47.7 \pm 0.8\%$	$48.4 \pm 0.8\%$	$47.9 \pm 0.8\%$	$48.1 \pm 0.8\%$
$10-20\%$	$49.0 \pm 0.5\%$	$48.9 \pm 0.5\%$	$49.2 \pm 0.5\%$	$49.0 \pm 0.5\%$	$49.1 \pm 0.5\%$
$20-30\%$	$50.2 \pm 0.5\%$	$49.9 \pm 0.5\%$	$50.4 \pm 0.5\%$	$50.0 \pm 0.4\%$	$50.3 \pm 0.5\%$
$30-40\%$	$51.1 \pm 0.5\%$	$50.9 \pm 0.5\%$	$51.4 \pm 0.5\%$	$50.9 \pm 0.4\%$	$51.3 \pm 0.5\%$
$40-50\%$	$51.5 \pm 0.5\%$	$51.2 \pm 0.5\%$	$51.8 \pm 0.5\%$	$51.4 \pm 0.4\%$	$51.6 \pm 0.5\%$
$50-100\%$	$53.0 \pm 0.3\%$	$52.8 \pm 0.3\%$	$53.3 \pm 0.3\%$	$52.9 \pm 0.3\%$	$53.1 \pm 0.3\%$
$0-100\%$	$49.3 \pm 0.2\%$	$49.1 \pm 0.2\%$	$49.6 \pm 0.2\%$	$49.2 \pm 0.2\%$	$49.4 \pm 0.2\%$
pp	$49.4 \pm 0.2\%$	$49.2 \pm 0.2\%$	$49.7 \pm 0.2\%$	$49.5 \pm 0.2\%$	$49.3 \pm 0.2\%$

Table 10.27: Systematic uncertainty for Υ(1S) using different polarizations. (All numbers in % are relative uncertainties).

Centrality	Υ(1S) R_{AA} Eff Ratio	Pol Syst
0-5%	1.05	0.44%
5-10%	1.03	0.23%
10-20%	0.99	0.41%
20-30%	0.99	0.21%
30-40%	0.95	0.22%
40-50%	0.94	0.02%
50-100%	0.94	0.17%
0-100%	1.00	0.21%

The correct trigger simulation was performed in the previous MC production, also used in the previous analysis iteration of Ref. [41].

Table 10.29 shows the reconstruction, trigger, and total efficiencies estimated using different simulations. From these values, the efficiency ratios evaluated for the different ratios explored in the analysis are shown in Table 10.30. When using total-efficiency estimates from the recent *pp* simulation (missing the correct trigger emulation), a correction factor a; on R_{AA} is needed for the trigger efficiency (the actual path used online has a larger efficiency than the simulated one). These correction factors, employing Table 10.29, are given by $a_{\Upsilon(1S)} = 93.91/90.22 = 1.041$, and $a_{\Upsilon(2S)} = 93.64/90.20 = 1.038$. Although a different release, with slightly different reconstruction software, is used to estimate the trigger correction for *pp*, the effect on the trigger efficiency estimation is considered negligible; no systematic uncertainty is assigned to this effect.

Table 10.28: Systematic uncertainty on Υ(2S) using different polarizations. (All numbers in % are relative uncertainties).

Centrality	Υ(2S) R_{AA} Eff Ratio	Pol Syst
0-5%	1.04	0.20%
5-10%	1.03	0.41%
10-20%	1.01	0.41%
20-30%	0.98	0.60%
30-40%	0.97	0.60%
40-50%	0.96	0.40%
50-100%	0.93	0.39%
0-100%	1.0	0.41%

Table 10.29: Efficiency comparisons from different simulations.

	total efficiency %	reco efficiency %	trigger efficiency %
$\Upsilon(1S)^{\text{old MC}}_{pp}$	54.0 ± 0.15	57.5 ± 0.15	93.91 ± 0.015
$\Upsilon(1S)^{\text{new MC}}_{pp}$	48.9 ± 0.08	54.2 ± 0.08	90.22 ± 0.014
$\Upsilon(1S)^{\text{new MC}}_{\text{PbPb}}$	48.8 ± 0.20	54.1 ± 0.20	90.20 ± 0.03
$\Upsilon(2S)^{\text{old MC}}_{pp}$	54.5 ± 0.13	58.2 ± 0.13	93.64 ± 0.014
$\Upsilon(2S)^{\text{new MC}}_{pp}$	49.3 ± 0.07	54.6 ± 0.07	90.20 ± 0.03
$\Upsilon(2S)^{\text{new MC}}_{\text{PbPb}}$	48.9 ± 0.30	54.3 ± 0.30	90.05 ± 0.05

Possible differences data - simulation (T&P)

No corresponding systematic uncertainty is assigned to discrepancies between data and simulation distributions.

Data-driven efficiency estimations, employing the tag and probe technique, are discussed in Sec. 7.0.1 and summarized in Tables 8.1 and 8.2. A comparison of the T&P results obtained for data and simulation is used to estimate systematic uncertainties. While these are considered to be negligble for the double ratios, the propagation of these efficiency uncertainties on the R_{AA} measurements is investigated.

Method A

The total PbPb systematic uncertainty on the T&P measurement, denoted by $\Delta_{\text{T\&P}}$, is formed as the quadratic sum of the trigger, muon ID, and tracking efficiency systematic errors, which

Table 10.30: Efficiency ratios and comparisons from different simulations.

efficiency ratios	total ratio	reco ratio	trigger ratio
$R_{2,\ pp}^{\text{old MC}} = \frac{\Upsilon(2S)_{pp}^{\text{old MC}}}{\Upsilon(1S)_{pp}^{\text{old MC}}}$	1.009 ± 0.0003	1.012 ± 0.0003	0.9971 ± 0.0001
$R_{2,\ pp}^{\text{new MC}} = \frac{\Upsilon(2S)_{pp}^{\text{new MC}}}{\Upsilon(1S)_{pp}^{\text{new MC}}}$	1.008 ± 0.0002	1.007 ± 0.0001	1.0010 ± 0.0001
$R_{2,\ \text{PbPb}}^{\text{new MC}} = \frac{\Upsilon(2S)_{\text{PbPb}}^{\text{new MC}}}{\Upsilon(1S)_{\text{PbPb}}^{\text{new MC}}}$	1.002 ± 0.0020	1.004 ± 0.0018	0.9984 ± 0.0002
$\chi_2^{\text{old MC}} = \frac{R_{2,\ pp}^{\text{old MC}}}{R_{2,\ \text{PbPb}}^{\text{new MC}}}$	1.007 ± 0.0016	1.008 ± 0.0014	0.9988 ± 0.0001
$\chi_2^{\text{new MC}} = \frac{R_{2,\ pp}^{\text{new MC}}}{R_{2,\ \text{PbPb}}^{\text{new MC}}}$	1.006 ± 0.0018	1.004 ± 0.0016	1.0020 ± 0.0001
$\Upsilon(1S)\ R_{AA}^{\text{old MC}} = \frac{\Upsilon(1S)_{\text{PbPb}}^{\text{new MC}}}{\Upsilon(1S)_{pp}^{\text{old MC}}}$	0.9037 ± 0.0011	0.9409 ± 0.0010	0.9605 ± 0.0002
$\Upsilon(1S)\ R_{AA}^{\text{new MC}} = \frac{\Upsilon(1S)_{\text{PbPb}}^{\text{new MC}}}{\Upsilon(1S)_{pp}^{\text{new MC}}}$	0.998 ± 0.0025	0.9982 ± 0.0022	0.9998 ± 0.0002
$\Upsilon(2S)\ R_{AA}^{\text{old MC}} = \frac{\Upsilon(2S)_{\text{PbPb}}^{\text{new MC}}}{\Upsilon(2S)_{pp}^{\text{old MC}}}$	0.8972 ± 0.0033	0.9330 ± 0.0030	0.9617 ± 0.0004
$\Upsilon(2S)\ R_{AA}^{\text{new MC}} = \frac{\Upsilon(2S)_{\text{PbPb}}^{\text{new MC}}}{\Upsilon(2S)_{pp}^{\text{new MC}}}$	0.9919 ± 0.0046	0.9945 ± 0.0042	0.9974 ± 0.0005

themselves are taken as twice (for the muon pair) the difference between data and simulation. Of the T&P results estimated for a single-muon leg, as in Table 8.1, the largest difference across the centrality bins is taken .

The full variation, $\Delta_{\text{T\&P}}$, evaluated from PbPb T&P is not a suitable contribution to the R_{AA} uncertainty: in fact, as R_{AA} involves the ratios of efficiencies between PbPb and pp, only the non-cancelling, centrality-dependent component of the efficiency would be affected.

Following the procedure employed in the previous R_{AA} measurement, documented in Ref. [40], an estimation method is considered where the systematic uncertainty on the R_{AA} is given by:

$$\Delta_{\text{T\&P}} \times |1 - \varepsilon_{pp}/\varepsilon_{\text{PbPb}}| \,. \tag{10.1}$$

From Tables 10.5 and 10.6, the second term in Eq. (10.1), as evaluated from MC simulation, is rather small. A typical value of order of 0.5% for the systematic is obtained.

Method B

A more conservative estimate is attempted by considering the variation of efficiencies with centrality. In this method, the T&P uncertainty on the R_{AA} results is assigned as the product of $\Delta_{\mathrm{T\&P}}$ and the largest efficiency difference across the centrality bins used in the analysis, as estimated from PbPb MC in Table 7.1. In this way, the data-MC efficiency systematic uncertainty is effectively applied only to the centrality-dependent portion of the efficiency (as the remaining, centrality-independent component is expected to cancel in the R_{AA} ratio, *pp*/PbPb). Specifically, the uncertainty in R_{AA} is evaluated as

$$\Delta_{\mathrm{T\&P}} \times |\varepsilon \text{ spread with centrality}| \,. \tag{10.2}$$

The result is shown in Table 10.31. A systematic value of order 2.1% for Υ(1S) is obtained.

This approach is more conservative than that previously decribed (method A), as the efficiency spread amongst centrality bins is larger than the efficiency difference between the centrality bin estimates in PbPb and the *pp* estimation, taken from MC.

Table 10.31: Relative systematic uncertainty for Υ(1S) and Υ(2S) R_{AA} from tag and probe efficiency estimates (method B).

	Υ(1S)	Υ(2S)
$\Delta_{\mathrm{T\&P}}$, fractional data-MC efficiency difference in T&P, from Table 8.1	19.1%	19.1%
highest efficiency for all centrality bins, from Table 7.1	51.7%	53.0%
lowest efficiency for all centrality bins, from Table 7.1	46.6%	47.3%
$\Delta\varepsilon_{\mathrm{cent}}$, fractional efficiency spread in centrality	10.9%	12.1%
T&P systematic on R_{AA}: $\Delta_{\mathrm{T\&P}} \times \Delta\varepsilon_{\mathrm{cent}}$	2.1%	2.3%

Method C

In the two methods described above, the assumption is made that the MC simulation accurately describes possible differences betwee PbPb and *pp*. That is, the second factor in Equations 10.1 and 10.2 are estimated from simulation. The approach described next attempts to include data-driven estimates of such possible differences by employing T&P measurements from both PbPb and *pp*.

The R_{AA} measurement, presented in Section 11.5.2, involves the ratio of efficiencies, see Eq.11.8:

$$R_{AA} \propto \frac{\varepsilon_{pp}}{\varepsilon_{\rm PbPb}} \equiv \zeta \,. \tag{10.3}$$

The efficiency ratio will be nominally estimated from MC simulation. As a systematic error, we estimate its fractional difference between data and simulation, employing the T&P results summarized in Tables 8.1 and 8.2. This can be expressed as

$$\begin{aligned} \text{uncertainty on } R_{AA} &= \frac{\zeta_{\rm MC} - \zeta_{\rm data}}{\zeta_{\rm MC}} \\ &= 1 - \frac{\varepsilon_{pp}^{\rm data}/\varepsilon_{\rm PbPb}^{\rm data}}{\varepsilon_{pp}^{\rm MC}/\varepsilon_{\rm PbPb}^{\rm MC}} \\ &= 1 - \frac{\varepsilon_{pp}^{\rm data}/\varepsilon_{pp}^{\rm MC}}{\varepsilon_{\rm PbPb}^{\rm data}/\varepsilon_{\rm PbPb}^{\rm MC}} \\ &= 1 - \frac{\varsigma_{pp}}{\varsigma_{\rm PbPb}}\,, \quad \text{with} \quad \varsigma \equiv \frac{\varepsilon^{\rm data}}{\varepsilon^{\rm MC}}\,. \end{aligned} \tag{10.4}$$

The results are summarized in Table 10.32.

Table 10.32: Relative systematic uncertainty for R_{AA} from tag and probe efficiency estimates (method C).

efficiency	*pp*			PbPb		
factor	data	MC	$\varsigma(\equiv \frac{\rm data}{\rm MC})$	data	MC	$\varsigma(\equiv \frac{\rm data}{\rm MC})$
trigger	0.925 ± 0.006	0.943 ± 0.002	0.981	0.968 ± 0.003	0.943 ± 0.001	1.031
tracking	0.82 ± 0.02	0.846 ± 0.010	0.969	0.796 ± 0.010	0.852 ± 0.001	0.948
muon ID	–	–	–	0.955 ± 0.008	0.955 ± 0.001	1.000
combined	0.758	0.798	0.951	0.736	0.767	0.959

efficiency factor	difference $1 - \frac{\varsigma_{pp}}{\varsigma_{\rm PbPb}}$
trigger	4.4%
tracking	-3.7%
muon ID	–
combined	0.9%

The final systematic uncertainty on the R_{AA} is evaluated as follows: (i) we take the ratio difference, in Table 10.32 (0.9%), (ii) we multiply this by a factor of 2 (to go from per-leg to per-

pair efficiency efficiency), (iii) we sum the results in quadrature with the estimate from Method B, to account for the centrality dependence. Finally, the systematic uncertainty on Υ(1S) and Υ(2S) from the T&P method is 3%.

Chapter 11

Ratios

Bottomonium suppression in PbPb collisions is studied in this section by measuring the ratios of observed yields of excited Υ states relative to the ground state Υ(1S), with the 150 μb^{-1} 2011 PbPb data. The suppression is inferred from a comparison of the ratios measured in PbPb against the *pp* reference. The centrality dedendence in the PbPb collisions is explored.

The data reconstruction and selection criteria are described in Sec. 4.3. The parameters of interest are extracted from the data samples directly via an extended unbinned maximum likelihood fit to the dimuon invariant-mass spectra described in Section 5.1.6.

11.1 Single ratio measurement

As mentioned previously, the following ratios of observed yields of Υ excited states relative to the ground state are studied:

$$R_{23} \equiv \frac{N\left(\Upsilon(2\mathrm{S})+\Upsilon(3\mathrm{S})\right)}{N(\Upsilon(1\mathrm{S}))}, \tag{11.1}$$

$$R_{2} \equiv \frac{N\left(\Upsilon(2\mathrm{S})\right)}{N(\Upsilon(1\mathrm{S}))}, \tag{11.2}$$

$$R_{3} \equiv \frac{N\left(\Upsilon(3\mathrm{S})\right)}{N(\Upsilon(1\mathrm{S}))}. \tag{11.3}$$

In addition to the combined excited-to-ground ratio, R_{23}, the current statistics allow for the separation of the 2S and 3S ratios, R_2 and R_3. No evidence for the Υ(3S) state is found in the PbPb data. The corresponding upper limit on this ratio is studied in Chapter. 9.

These ratios are measured from fits to the PbPb and *pp* datasets, separately performed. The nominal $p_{\mathrm{T}} > 4.0\,\mathrm{GeV}/c$ cut is used. These fits are displayed in Fig. 11.1.

Systematic variations of the fit model are performed to further establish the stability of the results. For the fit to the PbPb data, the following variations are considered:

- Like-sign background modeling: the background model is formed of two components, given by the like-sign distribution plus a second order polynomial; the PDF from the like-sign data is obtained from a fit employing the Erf * Exp model Fig 11.2(g);
- Like-sign background modeling using RooKeys: the background model is formed of two components, given by the like-sign distribution and a second order polynomial; the PDF from the like-sign data is obtained from the RooKeysPdf smoothing method Fig 11.2(d);
- Track-rotation background modeling: the background model is formed of two components, given by the track-rotation distribution and a second order polynomial; the PDF from the track-rotation data is obtained from a fit employing the Erf * Exp model Figures 11.2(h) and 11.2(i);
- Track-rotation background modeling using RooKeys: the background model is formed of two components, given by the track-rotation distribution and a second order polynomial; the PDF from the track-rotation data is obtained from the RooKeysPdf smoothing method Figures 11.2(e) and 11.2(f);
- The Crystal Ball signal tail parameters are fixed ($\alpha = 1.4$, from high-statistics *pp* data as in Table 6.1), Fig 11.2(a);
- The resolution is fixed ($\sigma_{1S} = 92$ MeV/c^2), Fig 11.2(b);

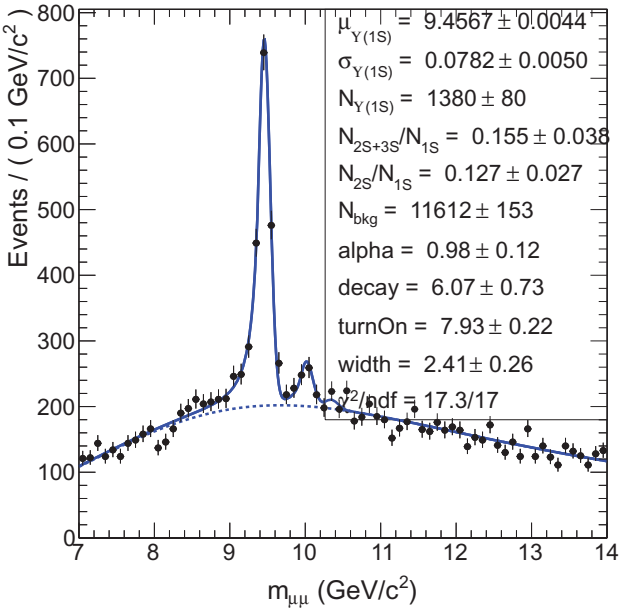

(a) Fit to the PbPb data

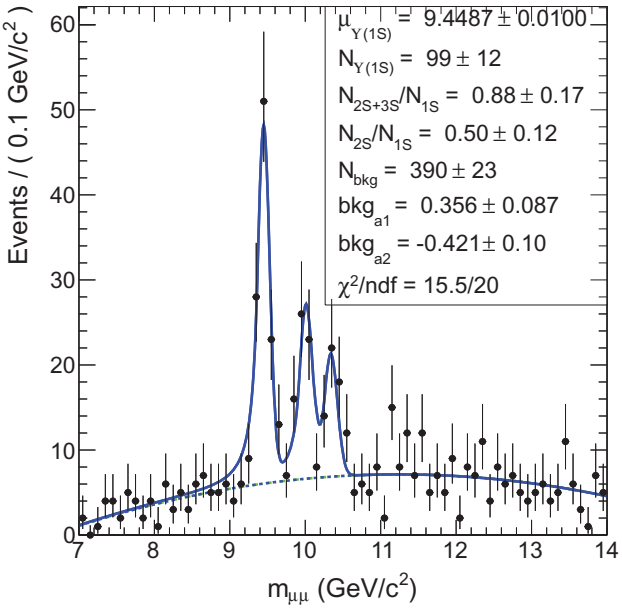

(b) Fit to the pp data

Figure 11.1: Nominal mass fits, performed separately to the PbPb $(150\,\mu b^{-1})$ and pp $(231\,nb^{-1})$ full datasets.

- The signal shape parameters are fixed ($\alpha = 1.4$, $n = 2.3$, $\sigma_{1S} = 92$ MeV/c^2), Fig 11.2(c).

For the fit to the *pp* data, these variations are considered:

- The Crystal Ball signal tail parameters are fixed ($\alpha = 1.4$, from high-statistics *pp* data as in Table 6.1)
- The resolution is fixed ($\sigma_{1S} = 92$ MeV/c^2);
- The signal shape parameters are fixed ($\alpha = 1.4$, $n = 2.3$, $\sigma_{1S} = 92$ MeV/c^2);
- Like-sign background modeling: the background model is formed of two components, given by the like-sign distribution and a second order polynomial; the PDF from the like-sign data is obtained from a fit employing the Erf * Exp model;
- Like-sign background modeling using Rookeys: the background model is formed of two components, given by the like-sign distribution and a second order polynomial; the PDF from the like-sign data is obtained from the RooKeysPdf smoothing method;
- Error function for background shape.

The associated systematic uncertainties are summarized in Table 11.1 for PbPb, and in Table 11.2 for *pp*. From the several variations, two estimates of the systematic uncertainty are provided: (i) the quadratic-mean deviation relative to the nominal central value, RMS (schematically, see Eq. 11.4); and (ii) the largest deviation. The latter is used as the estimated systematic uncertainty.

$$\text{RMS} \equiv \sqrt{(\sum \text{variation - nominal})^2/(\text{n}-1)}\,, \tag{11.4}$$

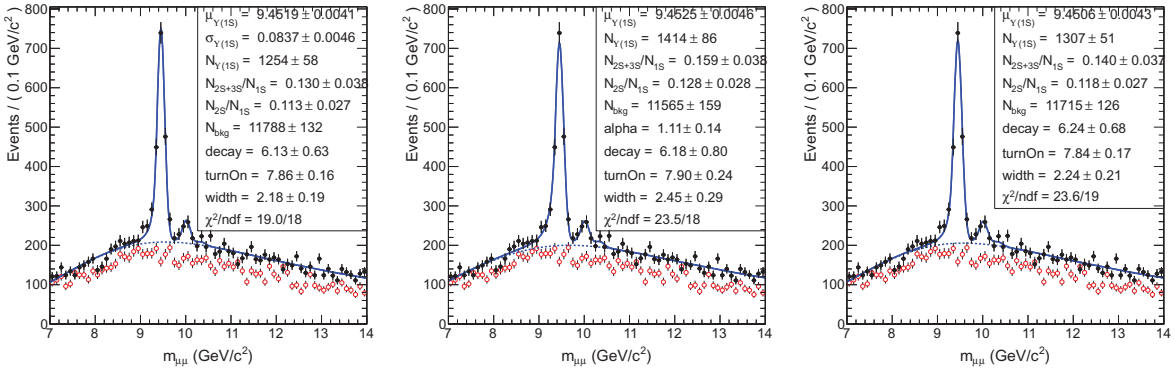

(a) fix CB to MC ($\alpha = 1.4$) (b) fix resolution to MC (c) fix CB and resolution to MC

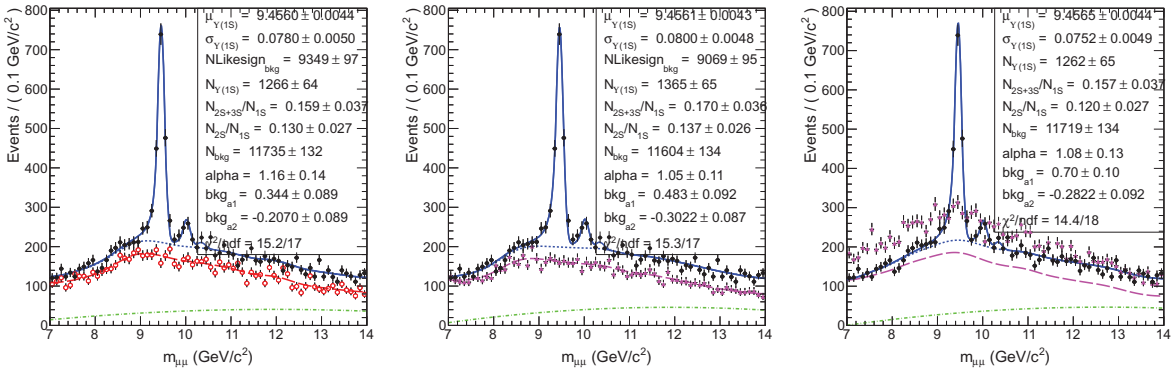

(d) LS keys + pol2 (e) LS TrkRot keys + pol2 (f) OS TrkRot keys + pol2

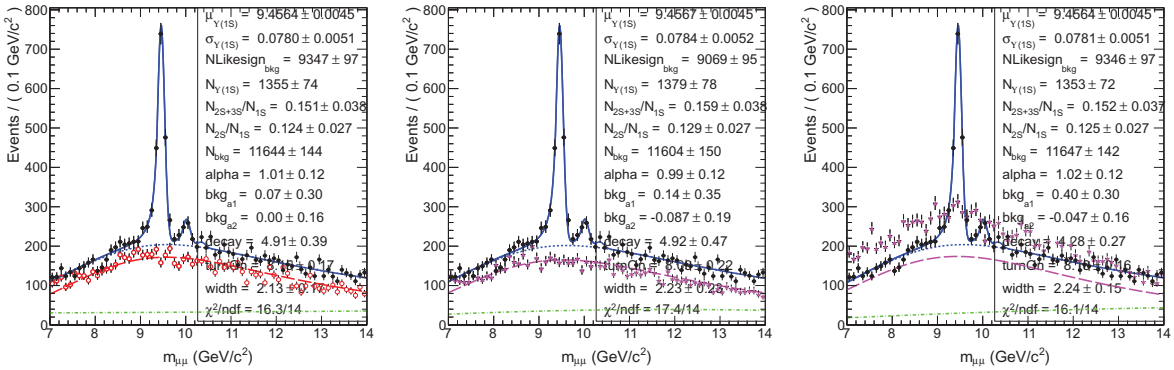

(g) LS Erf*Exp + pol2 (h) LS TrkRot Erf*Exp + pol2 (i) OS TrkRot Erf*Exp + pol2

Figure 11.2: PbPb fit model variations ($150\,\mu b^{-1}$).

Table 11.1: Summary of single-ratio results, for the PbPb dataset.

	$p_{\mathrm{T}}^{\mu} > 4\,\mathrm{GeV}/c$, Cent. 0-100%		
	R_{23}	R_2	R_3
nominal (Erf*Exp)	0.155 ± 0.038	0.127 ± 0.027	0.027 ± 0.025
systematic variations:			
like-sign (LS) keyspdf + pol.2	0.159 ± 0.037	0.130 ± 0.027	0.029 ± 0.046
LS Erf*Exp + pol.2	0.151 ± 0.038	0.124 ± 0.027	0.027 ± 0.047
opposite-sign (OS) Track Rotation (TR) keyspdf + pol.2	0.157 ± 0.037	0.120 ± 0.027	0.037 ± 0.046
OS TR Erf*Exp + pol.2	0.152 ± 0.037	0.125 ± 0.027	0.025 ± 0.046
fix CB tail from MC (alpha = 1.4)	0.130 ± 0.038	0.113 ± 0.027	0.017 ± 0.047
fix resolution from MC (92 MeV/c^2)	0.159 ± 0.038	0.128 ± 0.028	0.031 ± 0.047
fix both CB and resolution from MC	0.140 ± 0.037	0.118 ± 0.027	0.022 ± 0.046
fit systematic (RMS)	0.011	0.007	0.005
fit systematic (largest variation)	0.026	0.016	0.015
other checks:			
LS Track Rotation (TR) keyspdf + pol.2	0.170 ± 0.036	0.137 ± 0.026	0.033 ± 0.044
LS TR Erf*Exp + pol.2	0.159 ± 0.038	0.129 ± 0.027	0.030 ± 0.047
nominal simultaneous fit (Erf*Exp)	0.143 ± 0.038	0.119 ± 0.027	0.024 ± 0.024

Table 11.2: Summary of single-ratio results for the *pp* 2.76 TeV dataset.

	$p_{\mathrm{T}}^{\mu} > 4\,\mathrm{GeV}/c$		
	R_{23}	R_2	R_3
nominal (pol2; signal pdf fixed from PbPb)	0.88 ± 0.17	0.50 ± 0.12	0.38 ± 0.10
systematic variations:			
fix CB tail from MC	0.85 ± 0.16	0.49 ± 0.11	0.36 ± 0.19
fix resolution from MC	0.89 ± 0.16	0.49 ± 0.12	0.40 ± 0.20
fix both CB and resolution	0.87 ± 0.16	0.49 ± 0.11	0.38 ± 0.19
Erf*Exp	0.86 ± 0.16	0.49 ± 0.11	0.37 ± 0.19
LS keyspdf + pol.2	0.84 ± 0.17	0.48 ± 0.12	0.36 ± 0.21
LS Erf*Exp + pol.2	0.87 ± 0.16	0.49 ± 0.12	0.38 ± 0.20
fit systematic (RMS)	0.023	0.012	0.015
fit systematic (largest variation)	0.051	0.024	0.035
nominal simultaneous fit (pol2)	0.97 ± 0.19	0.56 ± 0.13	0.41 ± 0.11

11.2 Centrality dependence

Effects induced by the hot medium are expected to display, in general, a dependence on the centrality of the collision – the effect is accentuated for the most central collisions. The most peripheral events are expected to tend asymptotically towards those in the absence of medium effects. The *pp* collision results are taken as reference for absence of the nuclear effects.

We repeat the single ratio measurement, by splitting the PbPb dataset into centrality bins. The mass distributions are shown in Fig 11.3.

The systematic uncertainties are evaluated for the nominal selection and summarized in Table 11.3. The corresponding differential results are displayed in Fig. 11.5. In these plots, the single ratio values are normalized by the central value of the measurement performed using the *pp* data. Note these normalization values depend on the p_{T} threshold and are obtained from the fit to the *pp* data with the constrained signal shape by the MC, displayed in Table 11.2. The uncertainty on the single *pp* measurement is not included, because a common uncertainty factor is not relevant for point-to-point comparison of the double ratio trend with N_{part}. Some error bars in Fig. 11.5 include negative values. These are refines using Feldman-Cousins limit calculated as shown in Fig. 11.6.

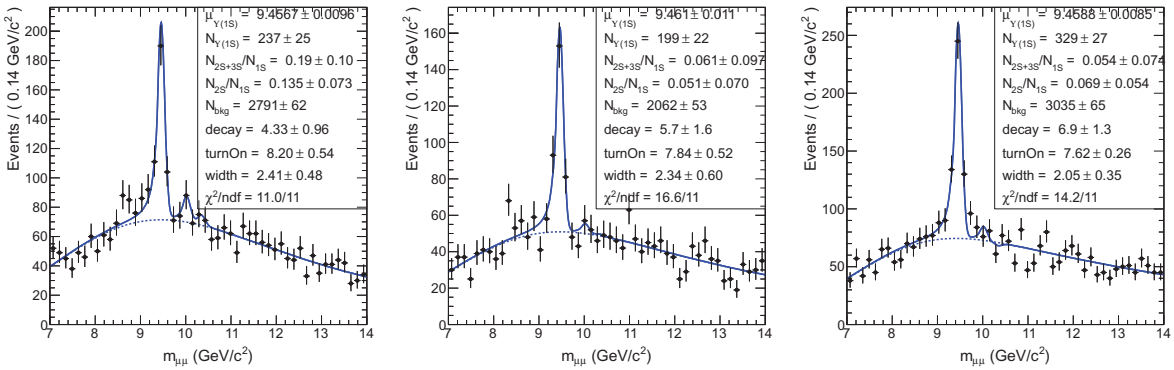

(a) 0- 5% (b) 5- 10% (c) 10- 20%

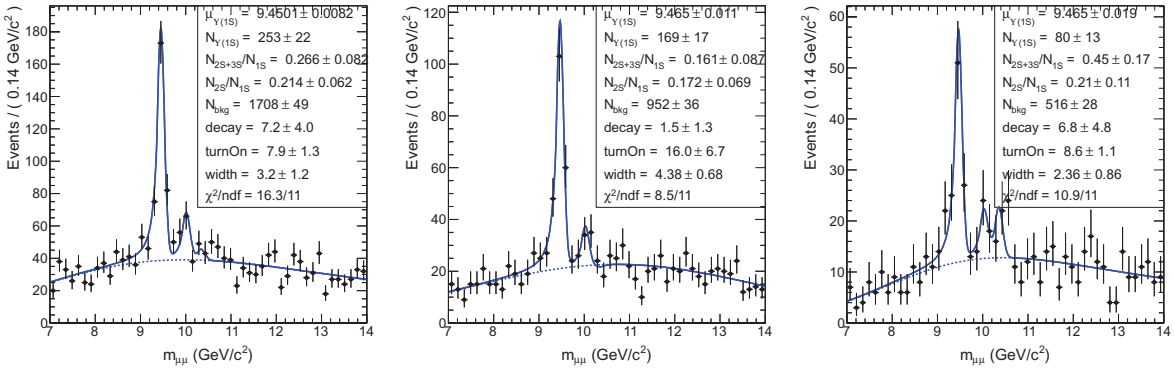

(d) 20- 30% (e) 30- 40% (f) 40- 50%

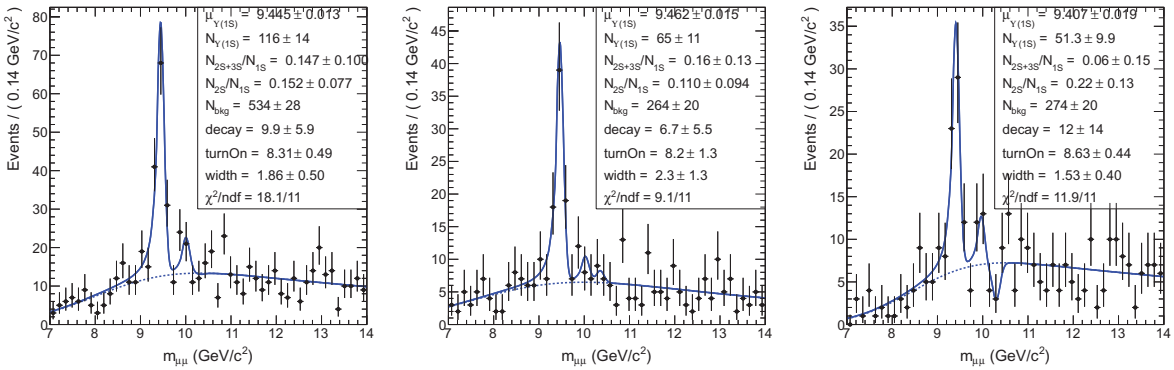

(g) 50-100% (h) 50- 60% (i) 60-100%

Figure 11.3: Centrality dependence of the PbPb single ratio, for $p_{\mathrm{T}}^{\mu} > 4.0\,\mathrm{GeV}/c$. $(150\,\mu b^{-1})$.

Table 11.3: Summary of single-ratio centrality dependent results.

	0-5%	5-10%	10-20%	20-30%	30-40%	40-50%	50-100%
R_{23} $(p_{\mathrm{T}}^{\mu} > 4.0\,\mathrm{GeV}/c)$							
nominal result	0.190 ± 0.100	0.061 ± 0.097	0.054 ± 0.074	0.266 ± 0.082	0.161 ± 0.087	0.450 ± 0.170	0.147 ± 0.100
systematic variations:							
LS keyspdf + pol.2	0.220 ± 0.099	0.009 ± 0.097	0.030 ± 0.075	0.246 ± 0.079	0.125 ± 0.088	0.488 ± 0.160	0.165 ± 0.095
TR keyspdf + pol.2	0.237 ± 0.097	-0.011 ± 0.093	0.109 ± 0.070	0.200 ± 0.084	0.151 ± 0.090	0.554 ± 0.169	0.164 ± 0.096
LS Erf*Exp + pol.2	0.189 ± 0.104	0.060 ± 0.097	0.029 ± 0.079	0.251 ± 0.082	0.125 ± 0.091	0.470 ± 0.158	0.128 ± 0.142
TR Erf*Exp + pol.2	0.187 ± 0.105	0.057 ± 0.100	0.078 ± 0.073	0.263 ± 0.080	0.151 ± 0.088	0.482 ± 0.156	0.055 ± 0.101
fix CB tail to MC	0.186 ± 0.109	0.039 ± 0.102	0.015 ± 0.083	0.234 ± 0.081	0.158 ± 0.087	0.512 ± 0.165	0.134 ± 0.104
fix resolution to MC	0.186 ± 0.101	0.051 ± 0.097	0.088 ± 0.076	0.287 ± 0.082	0.183 ± 0.087	0.497 ± 0.162	0.166 ± 0.100
fix both CB and resolution	0.162 ± 0.108	0.037 ± 0.099	0.039 ± 0.073	0.254 ± 0.081	0.151 ± 0.087	0.468 ± 0.169	0.126 ± 0.101
fit systematic:							
RMS	0.024	0.036	0.033	0.031	0.022	0.054	0.039
largest variation	0.047	0.072	0.055	0.066	0.036	0.104	0.092
R_2 $(p_{\mathrm{T}}^{\mu} > 4.0\,\mathrm{GeV}/c)$							
nominal result	0.135 ± 0.078	0.051 ± 0.070	0.069 ± 0.054	0.214 ± 0.062	0.172 ± 0.069	0.210 ± 0.110	0.152 ± 0.077
systematic variations:							
LS keyspdf + pol.2	0.154 ± 0.074	0.022 ± 0.070	0.047 ± 0.055	0.205 ± 0.062	0.150 ± 0.070	0.251 ± 0.107	0.159 ± 0.075
TR keyspdf + pol.2	0.164 ± 0.072	0.008 ± 0.068	0.102 ± 0.053	0.171 ± 0.064	0.172 ± 0.072	0.255 ± 0.112	0.160 ± 0.076
LS Erf*Exp + pol.2	0.134 ± 0.075	0.052 ± 0.071	0.056 ± 0.056	0.204 ± 0.063	0.152 ± 0.071	0.220 ± 0.107	0.141 ± 0.096
TR Erf*Exp + pol.2	0.133 ± 0.075	0.050 ± 0.071	0.080 ± 0.054	0.211 ± 0.062	0.165 ± 0.070	0.223 ± 0.107	0.103 ± 0.078
fix CB tail to MC	0.136 ± 0.077	0.039 ± 0.071	0.044 ± 0.057	0.194 ± 0.060	0.176 ± 0.069	0.204 ± 0.110	0.149 ± 0.079
fix resolution to MC	0.127 ± 0.074	0.046 ± 0.071	0.087 ± 0.056	0.224 ± 0.063	0.189 ± 0.070	0.209 ± 0.109	0.162 ± 0.078
fix both CB and resolution	0.116 ± 0.077	0.038 ± 0.070	0.057 ± 0.052	0.206 ± 0.061	0.171 ± 0.068	0.211 ± 0.110	0.144 ± 0.077
fit systematic:							
RMS	0.015	0.021	0.021	0.019	0.013	0.024	0.020
largest variation	0.029	0.043	0.033	0.043	0.022	0.045	0.049

11.3 Double ratio measurement

Here we compare the single ratios measured in PbPb and *pp*. Such a double-ratio is given by as previously defined in Chapter 7.

$$\chi_{23} \equiv \frac{R_{23|\mathrm{PbPb}}}{R_{23|pp}} = \frac{[N(\Upsilon(2S)+\Upsilon(3S))/N(\Upsilon(1S))]_{\mathrm{PbPb}}}{[N(\Upsilon(2S)+\Upsilon(3S))/N(\Upsilon(1S))]_{pp}}, \tag{11.5}$$

$$\chi_{2} \equiv \frac{R_{2|\mathrm{PbPb}}}{R_{2|pp}} = \frac{[N(\Upsilon(2S))/N(\Upsilon(1S))]_{\mathrm{PbPb}}}{[N(\Upsilon(2S))/N(\Upsilon(1S))]_{pp}}, \tag{11.6}$$

$$\chi_{3} \equiv \frac{R_{3|\mathrm{PbPb}}}{R_{3|pp}} = \frac{[N(\Upsilon(3S))/N(\Upsilon(1S))]_{\mathrm{PbPb}}}{[N(\Upsilon(3S))/N(\Upsilon(1S))]_{pp}}. \tag{11.7}$$

No evidence for the Υ(3S) state is found in the PbPb data, and the corresponding ratio is studied in Chapter. 9.

Several effects, and their associated uncertainties, cancel out in the computation of these doubly-normalized observables, including efficiency and acceptance correction factors.

The PbPb and *pp* data samples are fit simultaneously. The double ratios are extracted directly as fit parameters. The background is described by the nominal Erf*Exp model, in the case of the PbPb dataset. For the *pp* dataset, in view of the smaller statistics, a simpler background model is employed, namely a second order polynomial. The signal shape parameters are common, while the backgrounds float separately in the simultaneous fit. The fit projections are shown in Figures 11.4.

The double-ratio results and systematic uncertainties are summarized in Table 11.4. We tried 7 different systematic variations for the signal fit function (Table 11.4):

- the CB signal tail parameters are fixed ($\alpha = 1.4$, from high-statistics *pp* data as in Table 6.1)
- The Υ(1S) mass resolution is fixed to Monte Carlo (92 MeV/c^2);
- The CB parameters and mass resolution are fixed;
- The CB tail is allowed to float separately in *pp* and PbPb samples, (shared for the nominal);

- Let the resolution float separately in *pp* and PbPb samples, (shared for the nominal);
- Let both the CB tail and resolution float separately in pp and PbPb samples (they are shared for nominal);
- The Υ(1S) mass mean is shared in the *pp* and PbPb samples but float separately in the nominal configuration.

For the background function, we tried the following three sets of variations (Table 11.4):

- Keep the second order polynomial for *pp*, but vary the PbPb fit with 4 different pdfs;
- Keep the Erf*Exp function for PbPb, but vary the pp fit with 4 different pdfs;
- Vary both PbPb and *pp* background pdfs simultaneously.

The systematic uncertainties associated with the signal and background modeling are estimated as the RMS, computed relative to the nominal fit value, for the corresponding set of variations described above. The total systematic uncertainty is obtained as the sum of these two sources in quadrature. The systematic uncertainties on the double ratios are detailed in Table 11.4.

No clear dependence can be inferred within the statistical precision offered by the data. We also note that the most peripheral bin in PbPb and the *pp* reference do not necessarily match, both because a fully peripheral bin is not accessible given limited statistics in the data and as a consequence of complexity of the underlying phenomena.

11.4 Kinematic dependences

Both he single-ratio and double-ratio measurements are performed in bins of dimuon rapidity and p_{T}, for the nominal selection ($p_{\mathrm{T}} > 4.0$ GeV/c) . The fits to the data are shown in Figs 11.7 and 11.8. The background level and shape are seen to vary considerably in the different regions, as

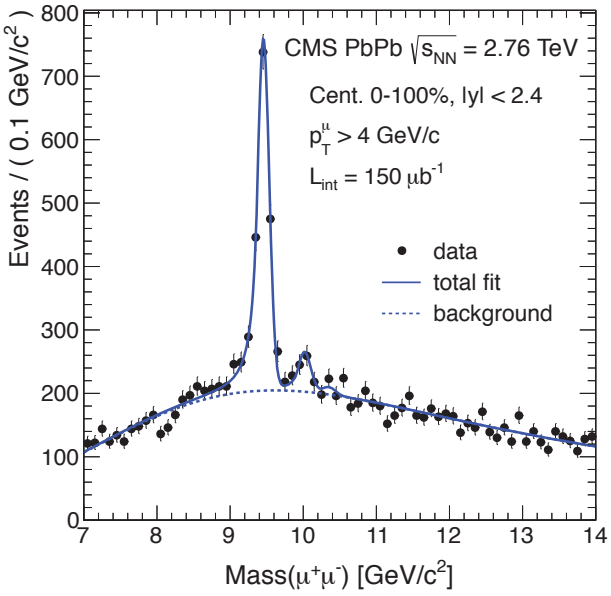

(a) PbPb projection

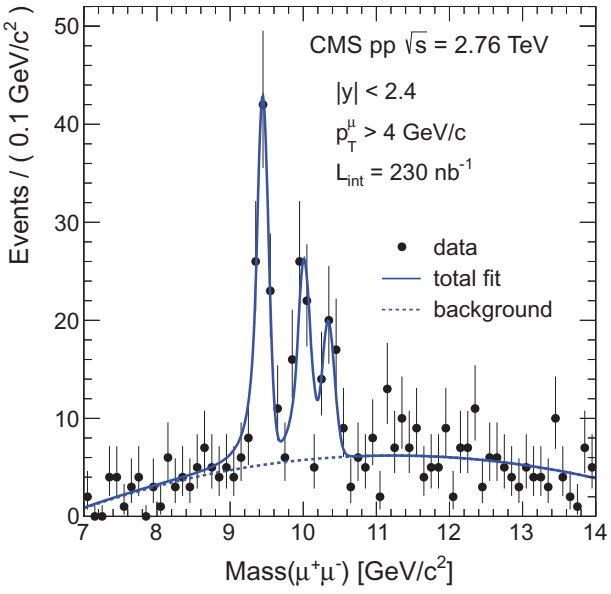

(b) *pp* projection

Figure 11.4: Simultaneous fit to the PbPb $(150\,\mu b^{-1})$ and *pp* $(231\,nb^{-1})$, for $p_{\mathrm{T}}^{\mu} > 4.0\,\mathrm{GeV}/c$.

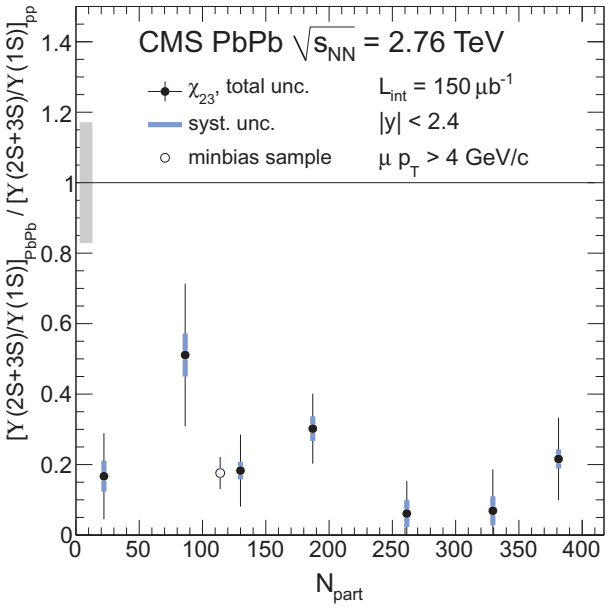

(a) χ_{23},$p_{\mathrm{T}}^{\mu} > 4.0\,\mathrm{GeV}/c$

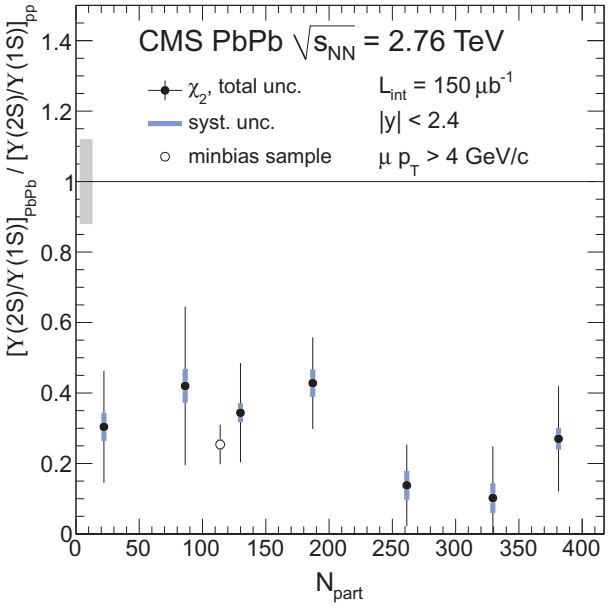

(b) χ_2, $p_{\mathrm{T}}^{\mu} > 4.0\,\mathrm{GeV}/c$

Figure 11.5: Centrality dependence of the double ratios χ_{23} and χ_2; the PbPb statistical and systematic uncertainties are included; the graphs are normalized by the corresponding *pp* single-ratio central values; *pp* uncertainties are represented by the gray box at unity, and are excluded from the data points as they do not affect point-to-point comparison. $(150\,\mu b^{-1})$.

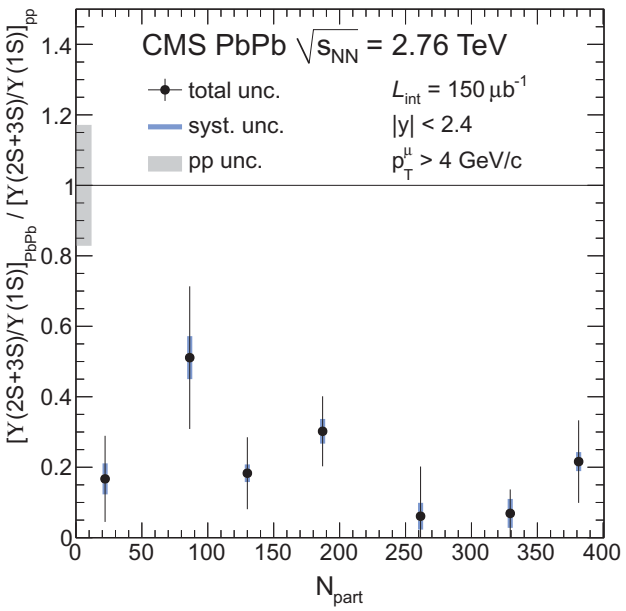

(a) χ_{23},$p_{\mathrm{T}}^{\mu} > 4.0\,\mathrm{GeV}/c$

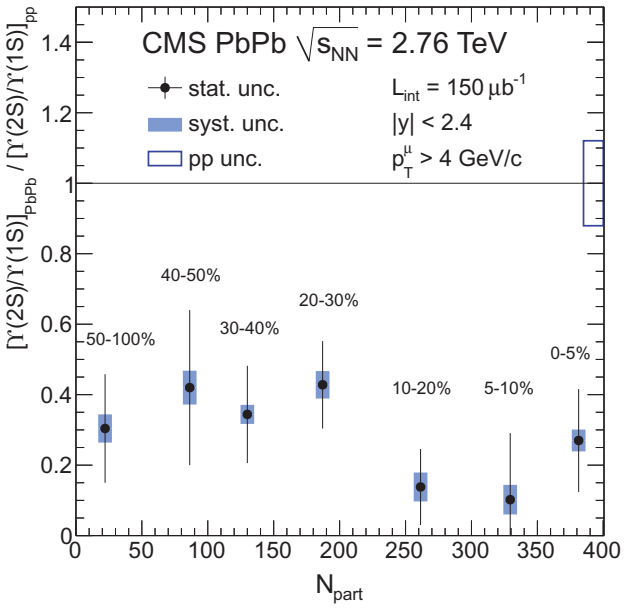

(b) χ_2, $p_{\mathrm{T}}^{\mu} > 4.0\,\mathrm{GeV}/c$

Figure 11.6: Centrality dependence of the double ratio.

expected. For example, the kinematic effect due to the muon p_{T} selection threshold is more noticeable for low dimuon p_{T} and high rapidity regions, with softer muon p_{T} spectra.

The double-ratio results are represented in the graphs in Fig. 11.9. Due to the limitted statistics in the *pp* sample, the statistical precision available can not infer possible dependencies of the double ratio on the inspected kinematic variables.

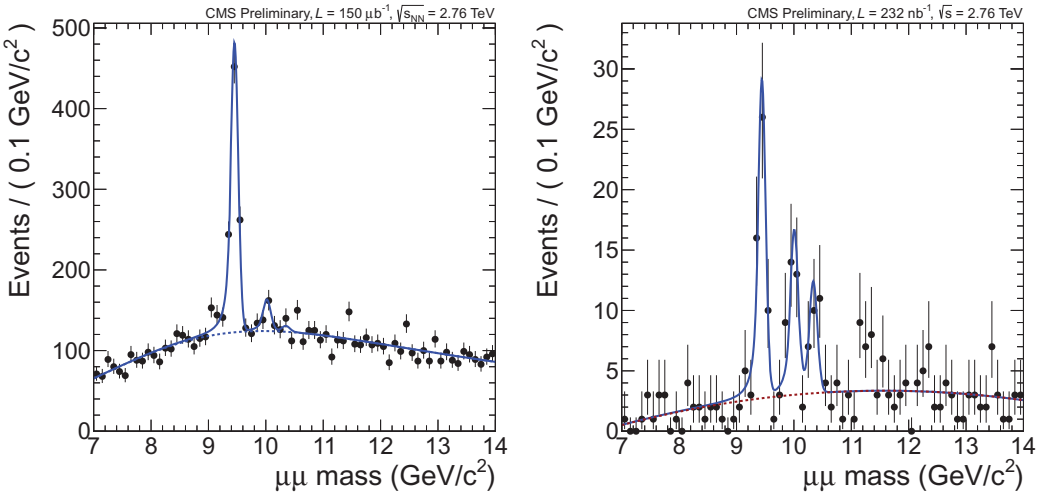

(a) PbPb data $0.0 < |y| < 1.0$

(b) *pp* data $0.0 < |y| < 1.0$

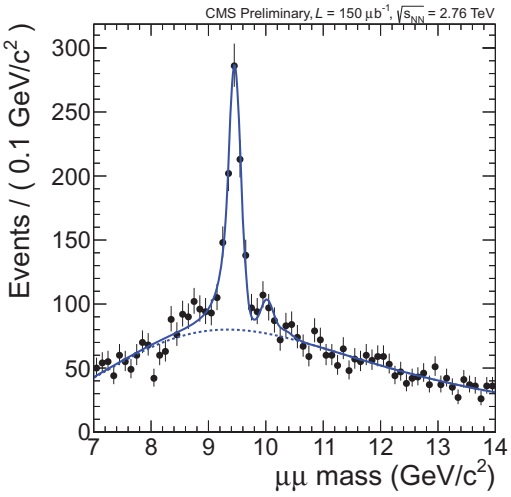

(c) PbPb data $1.0 < |y| < 2.4$

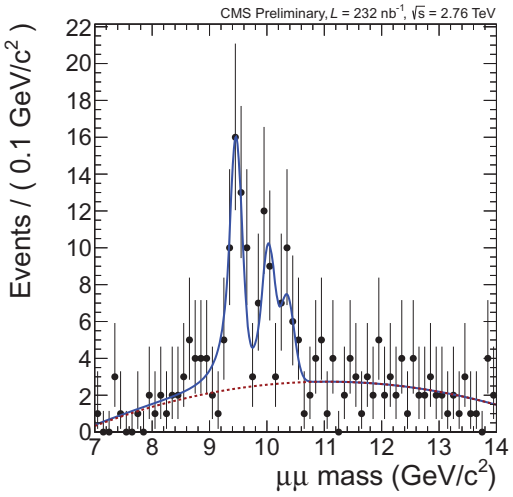

(d) *pp* data $1.0 < |y| < 2.4$

Figure 11.7: Mass fits in dimuon rapidity ranges.

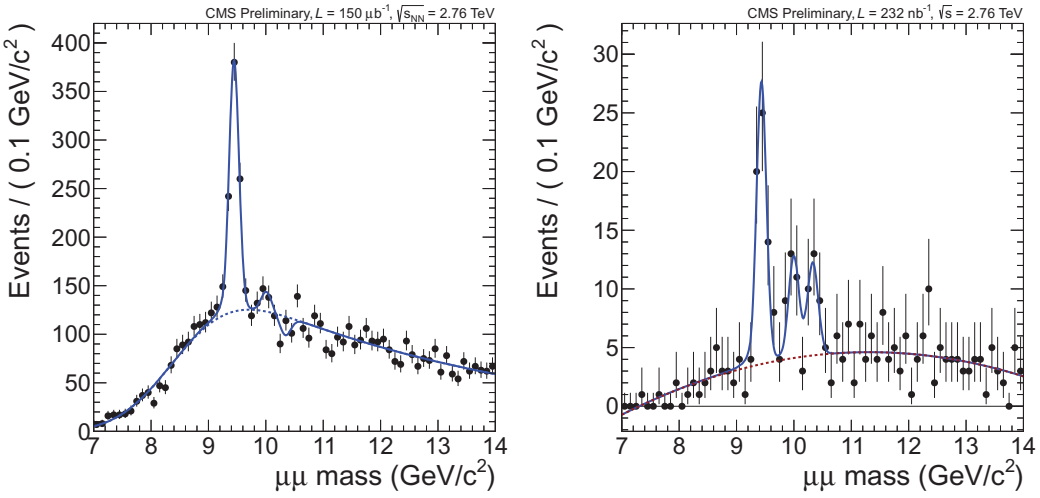

(a) PbPb data $p_{\mathrm{T}}^{\Upsilon} < 5\,\mathrm{GeV}/c$

(b) pp data $p_{\mathrm{T}}^{\Upsilon} < 5\,\mathrm{GeV}/c$

(c) PbPb data $p_{\mathrm{T}}^{\Upsilon} > 5\,\mathrm{GeV}/c$

(d) pp data $p_{\mathrm{T}}^{\Upsilon} > 5\,\mathrm{GeV}/c$

Figure 11.8: Mass fits in dimuon p_{T} ranges.

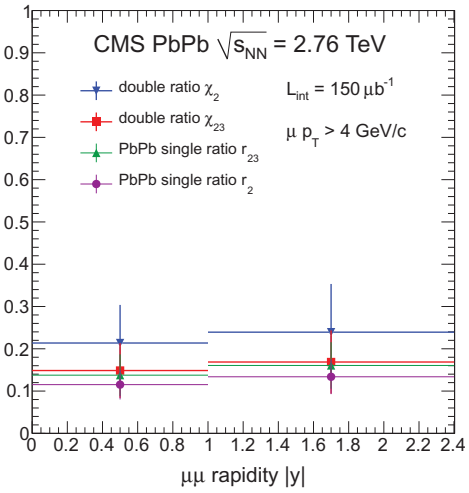

(a) $|y|$ dependence, statatistical error only

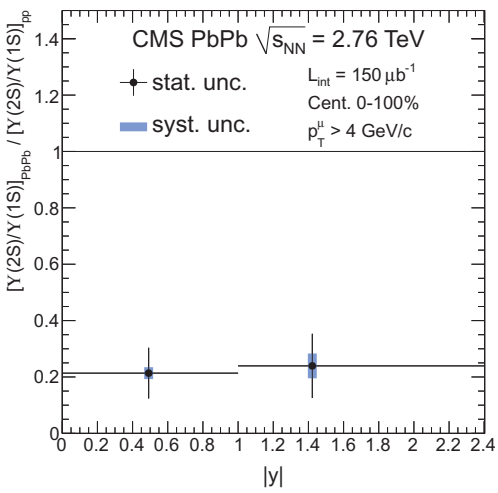

(b) $|y|$ dependence, with systematics

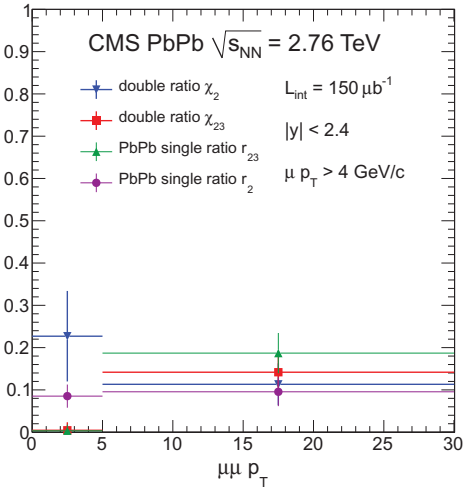

(c) p_{T} dependence, statatistical error only

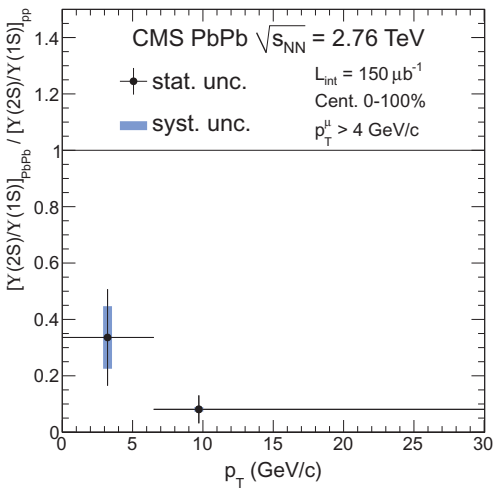

(d) p_{T} dependence, with systematics

Figure 11.9: Rapidity and p_{T} dependencies of the double ratios.

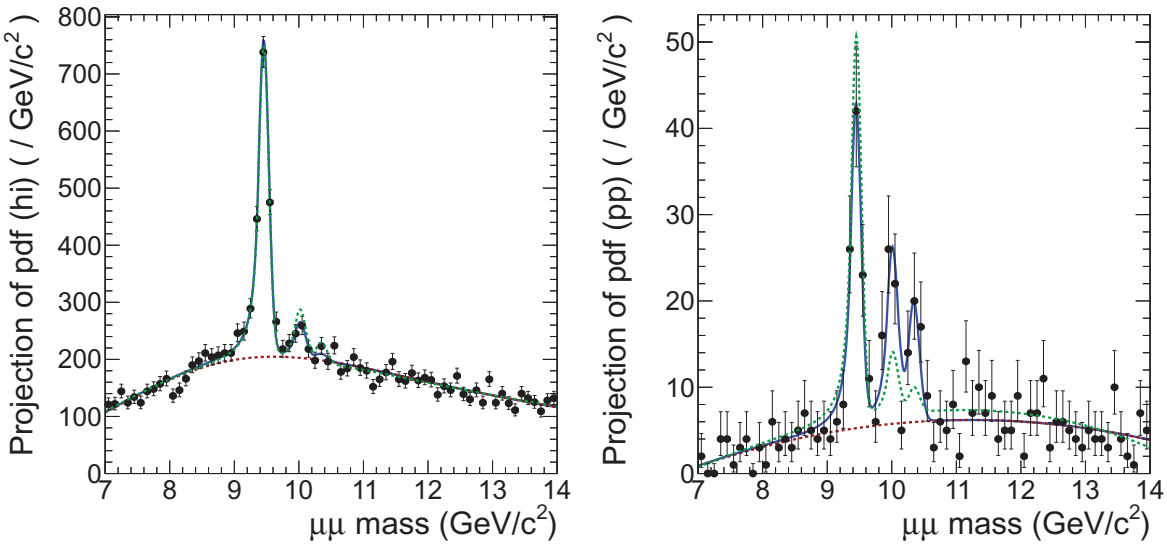

(a) PbPb data fit projection

(b) *pp* data fit projection

Figure 11.10: Mass projections of the fit overlaid with the same fit under the assumption of the null hypothesis show in the dashed green curve, used in the estimation of the significance.

11.5 Significance

11.5.1 Double ratio significance

Here we attempt to quantify the significance of the observed relative suppression of the excited-to-ground states, estimated through the double ratios χ_{23} and χ_2.

The nominal method employed employs the profile likelihood calculator, implemented in the RooStats package (`ProfileLikelihoodCalculator`). The null hypothesis is that χ_{23} and χ_2 are unity. Utilizing the nominal fit procedure, and ignoring systematic uncertainties, the obtained p-value of our result with respect to the null hypothesis corresponds to 6.3σ. The projections of the fit overlaid with the fit under the null hypothesis is shown in Fig. 11.10.

The propagation of systematic uncertainties is challenging. In particular, the various systematic variations considered cannot be readily expressed as nuisance parameters in the nominal fit model. Instead, we adopt for this purpose a modified fit configuration, identical to our nominal except that we

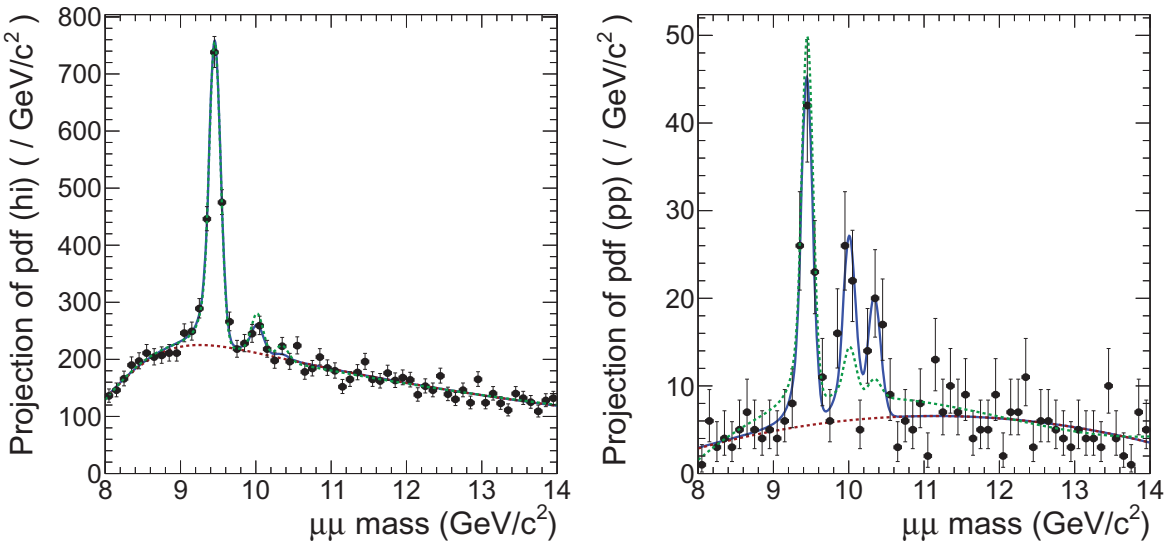

(a) PbPb data fit projection

(b) pp data fit projection

Figure 11.11: Mass projections of the fit overlaid with the same fit under the assumption of the null hypothesis show in the dashed green curve, used in the estimation of the significance. The fit is performed in a restricted mass range to account for the systematic and statistical uncertainties, as described in the text.

restrict the fitting range to $(8, 14)$ GeV/c^2. This has the effect of increasing the statistic fit uncertainties on the parameters of interest (i.e. the double ratios) to the level expected for the total uncertainties from the nominal fit range, including the corresponding systematic errors. We also include systematic errors on the fixed FSR tail parameter. This procedure yields a p-value estimate corresponding to 5.4σ. The projections including the null hypothesis are shown in Fig. 11.11.

For the previous measurement [39], we estimated the probability for a fluctuation of the background to yield a result as extreme as the one observed, by generating pseudo-experiments according to the no-suppression scenario (null hypothesis), and counting the fraction of occurrencies (p-value) for which the double ratio value χ is smaller than that observed in the data. In further detail, the following steps are performed:

1. Take the signal and background distribution for the nominal *pp* fit. Then, take the background from the PbPb fit to the sidebands. In the signal shape allow for known fluctuations of the fixed shape parameters.

2. Generate a *pp* pseudo-data sample using the fit to the *pp* data as a template. In this, allow the relative contributions from the background and three signal resonances to shift within their respective statistics, but fix the total number of events to the number observed in the data.

3. Generate background pseudo-data using the PbPb background nominal model.

4. Generate the PbPb signal pseudo-data using the *pp* signal model. The number of events is constrained so that N_{bkg} (generated in step 3) and N_{sig} from this step equals the number of events observed in the data. Because we are generate this with the *pp* signal model, χ_{23} is unity up to statistical fluctuations.

5. Fit these pseudo-data samples using the nominal fitter.

6. From the distributions of χ_{23} and χ_2 obtained in this fashion, integrate from $-\infty$ to the observed data value to get the p-value of the measurement.

To cross check our new profiled likelihood significance calculation we employed it on the data from the 2011 result[39]. We calculated the significance using the procedure just described. When we included all systematic uncertainties we found the significance of our result was $2.4\,\sigma$. Using the profile likelihood procedure with the data and models of the 2011 measurement we find a significance of $2.8\,\sigma$, where this is purely statistical. The compatibility of these two methods provides some validation for the profiled likelihood significance determination.

Applying this method to half of the current data and nominal fit configuration, the distributions of χ_{23} obtained from 10k generated pseudo-experiments are shown in Fig. 11.12. The vertical, red lines indicated in the plots, at 0.472 ($p_{\mathrm{T}}^{\mu} > 3.5\,\mathrm{GeV}/c$) and 0.488 ($p_{\mathrm{T}}^{\mu} > 4.0\,\mathrm{GeV}/c$), denote the ex-

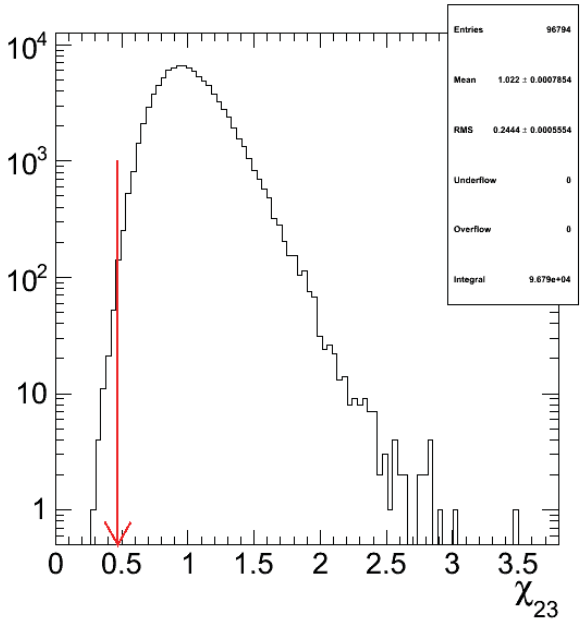

(a) $p_{\mathrm{T}}^{\mu} > 3.5\,\mathrm{GeV}/c$

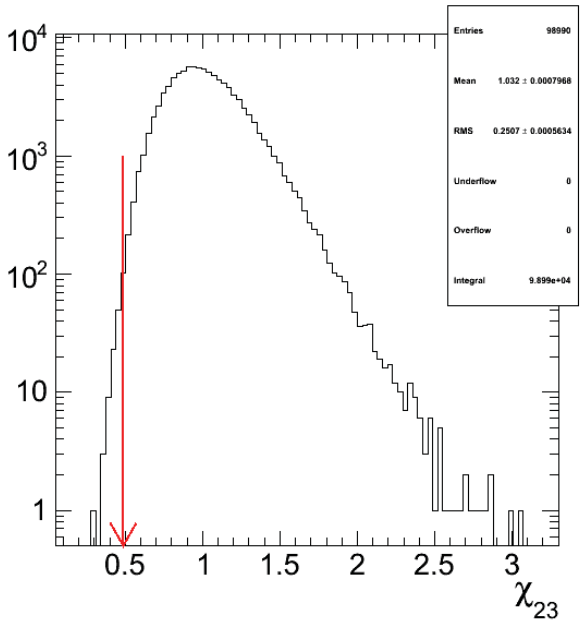

(b) $p_{\mathrm{T}}^{\mu} > 4.0\,\mathrm{GeV}/c$

Figure 11.12: Distributions of χ_{23} from pseudo-experiments generated under the hypothesis of no suppression. The arrow indicates the χ_{23} value that would correspond to 3σ significance.

tracted $3\,\sigma$ equivalent χ_{23} values. The measured double ratio results, shown in Table 11.4, are indeed smaller than these indicated values, which therefore indicate a significance higher than three standard deviations.

We then generated 500k pseudo-experiments as per our outlined procedure ($p_{\mathrm{T}}^{\mu} > 4.0\,\mathrm{GeV}/c$). The χ_2 and χ_{23} values were smeared from unity at generation according to their respective % systematic uncertainty. This is an extremely conservative approach since the magnitude of the error certainly does not scale with the central value. But since we are unaware how it scales this is what we've adopted since it is conservative. This accounts for the systematic errors on the double ratios. As shown in Fig. 11.13, there are no events with a χ_2 value as extreme as we observe. This corresponds to a p-value smaller than 2.7×10^{-6} which is larger than $4\,\sigma$, the limit we can probe with this method.

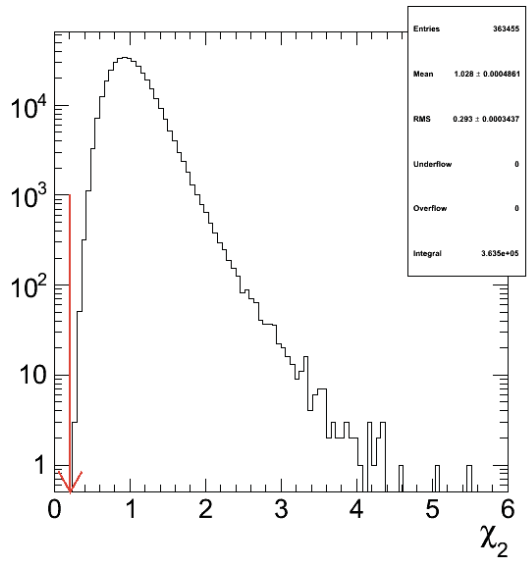

Figure 11.13: Distributions of χ_2 from pseudo-experiments generated under the hypothesis of no suppression. The arrow indicates the χ_2 value that would correspond to 4σ significance (systematic included).

Given the very small expected p-value, associated with the considerably higher significance of the current result compared to our previous measurement [39], this same method is impractical to attempt. Indeed, an estimate of the significance would require the tail of the p-value distribution in

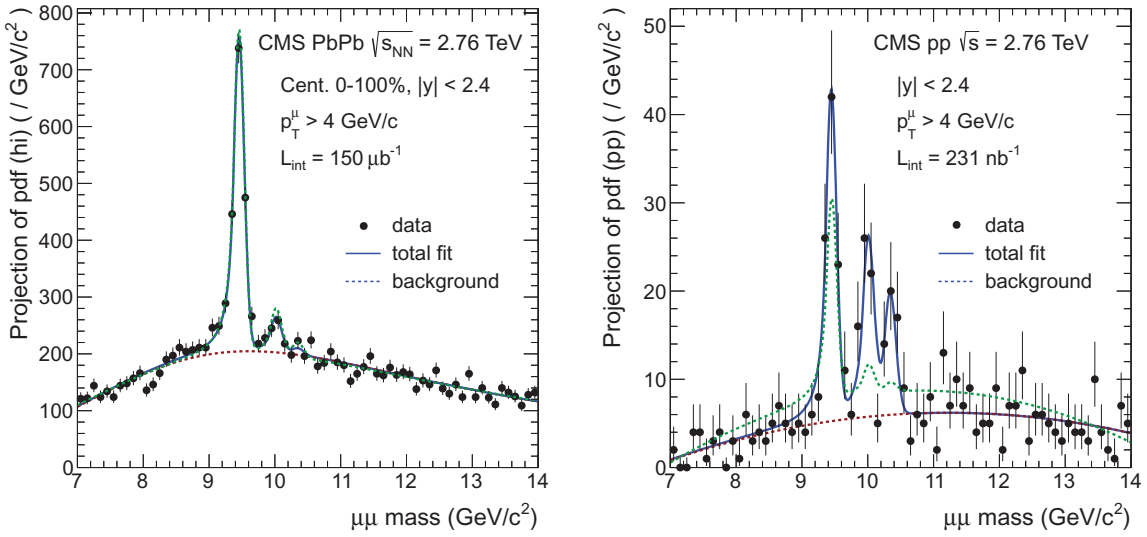

(a) PbPb data fit projection

(b) *pp* data fit projection

Figure 11.14: Mass projections of the fit overlaid with the same fit under the assumption of the null hypothesis show in the dashed green curve, used in the estimation of the significance. The null hypothesis: $R_{AA} = 1$ for Υ(1S), Υ(2S) and Υ(3S)

Fig. 11.12 and Fig. 11.13 to be well populated, which in turn requires larger generation of pseudo-experiments – beyond what is reasonably feasible. This justifies the use of the alternative method described above for estimating the significance of our current result.

11.5.2 R_{AA} significance

Similar approach is applied to compute the significance for R_{AA}. The result is summarised in Table 11.5. The fit plots for each case are shown in Fig. 11.14, Fig. 11.15, Fig. 11.16, and Fig. 11.17.

In addition to the *relative* excited-to-ground-state suppression, explored in Sec. 11.3, a measurement of the *absolute* suppression of the individual $\Upsilon(nS)$ states is performed. In addition, relevant information about the suppression phenomena is this way extracted from the data. Effectively, the ratio of the $\Upsilon(nS)$ cross sections in PbPb and *pp* collisions is determined. The procedure employed follows the description in Ref. [41].

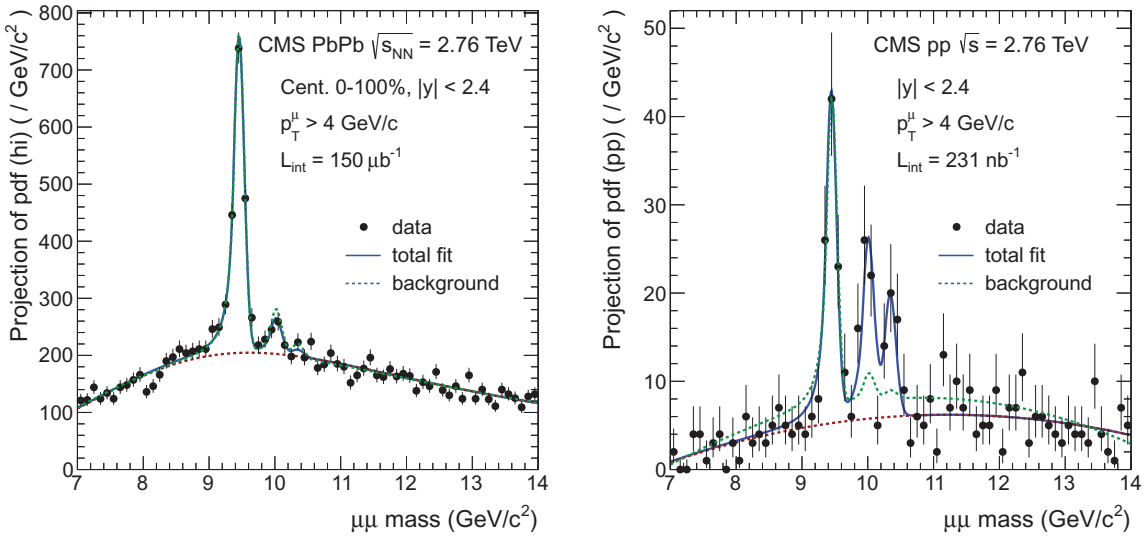

(a) PbPb data fit projection

(b) pp data fit projection

Figure 11.15: Mass projections of the fit overlaid with the same fit under the assumption of the null hypothesis show in the dashed green curve, used in the estimation of the significance. The null hypothesis: $R_{AA} = 1$, for Υ(2S) and Υ(3S)

This ratio is estimated via the nuclear modification factor, R_{AA}, defined as:

$$R_{AA}(\Upsilon(nS)) = \frac{\mathcal{L}_{pp}}{T_{AA} N_{\rm MB}} \frac{N_{\rm PbPb}(\Upsilon(nS))}{N_{pp}(\Upsilon(nS))} \cdot \frac{\varepsilon_{pp}}{\varepsilon_{\rm PbPb}}\,, \tag{11.8}$$

based on raw yields and correcting for the multiplicity-dependent fraction of the efficiency ($\varepsilon_{pp}/\varepsilon_{\rm PbPb}$). The individual terms entering in Eq. 11.8 are:

- N_{pp} and $N_{\rm PbPb}$ are the number of measured $\Upsilon(nS)$ in the pp and PbPb data, respectively;
- $\mathcal{L}_{pp}$, luminosity of the pp 2.76 TeV dataset, $231 \pm 14\ nb^{-1}$;
- $N_{\rm MB} = 1126653312$, is the number of minimum bias events sampled by CMS when the dimuon trigger was live. It is multiplied by the centrality bin width for distributions as a function of $N_{\rm part}$;

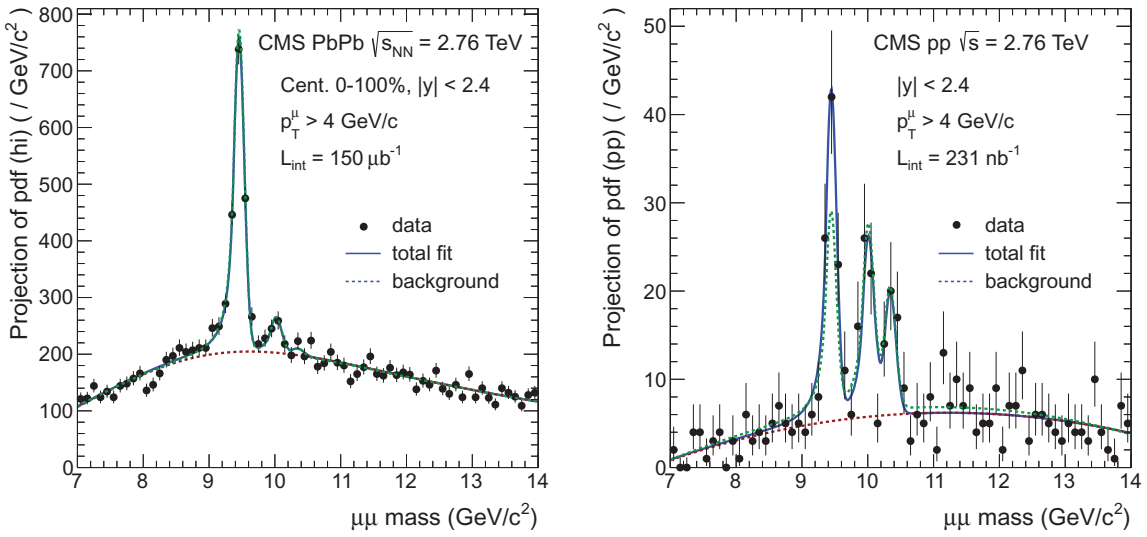

(a) PbPb data fit projection

(b) *pp* data fit projection

Figure 11.16: Mass projections of the fit overlaid with the same fit under the assumption of the null hypothesis show in the dashed green curve, used in the estimation of the significance. The null hypothesis: $R_{AA} = 1$ for Υ(1S)

- T_{AA} is the nuclear overlap function which varies with the centrality of the collision, has units of mb^{-1}, being defined as $T_{AA} =< N_{\rm coll} > /\sigma_{pp}$, with σ_{pp} the inelastic pp cross section.

- ε is the combined trigger and reconstruction efficiency which depends on the $p_{\rm T}$ and rapidity of the quarkonium state and the centrality of the collision;

11.5.3 Υ(1S) and Υ(2S) R_{AA} measurements

Measuremens are provided for the Υ(1S) and Υ(2S) states, individually. The Υ(3S) state is not prominent in the PbPb dataset. An upper limit on the corresponding R_{AA} may be set using the results presented in Sec. 11.5.5.

The observed Υ(1S) and Υ(2S) yields are summarized in Tables 11.6, 11.8 and 11.7, for PbPb and *pp*. The efficiency corrections are those from Table 7.1. The R_{AA} values for the various centrality bins are listed in Table 11.11 and displayed in the graphs in Fig. 11.18. A log scale R_{AA} plot is shown in

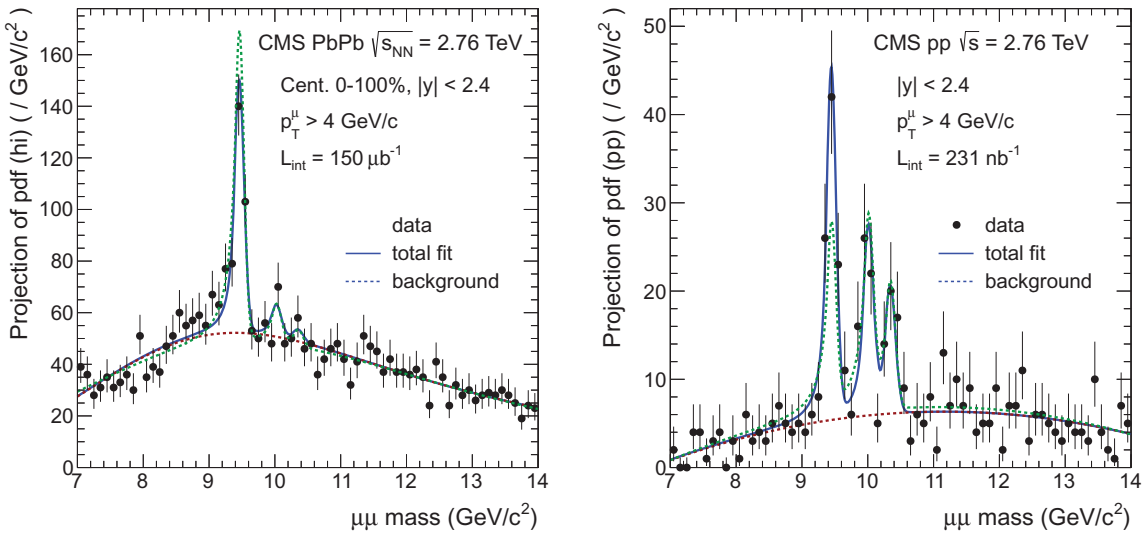

(a) PbPb data fit projection

(b) *pp* data fit projection

Figure 11.17: Mass projections of the fit overlaid with the same fit under the assumption of the null hypothesis show in the dashed green curve, used in the estimation of the significance. The null hypothesis: $R_{AA} = 1$ for Υ(1S). (centrality $< 10\%$ cut is used for the PbPb sample.)

Fig. 11.19. A strong centrality dependence can be observed for the R_{AA} of Υ(1S). The R_{AA} values for the various p_{T} and rapidity bins are listed in Table 11.13 and displayed in the graphs in Fig. 11.20. We also studied the stability of R_{AA} results against different single muon p_{T} cut, as displayed in Fig. 11.19.

The uncertainty on the measured R_{AA} values is estimated from the uncertainties associated to each term in Eq. 11.8. The statistical uncertainty on the R_{AA} measurement corresponds to the statistical uncertainty on the yields. The systematic uncertainties from the yield determination (Tables 11.6, 11.7, using the method discussed in Sec. 11.1), from the efficiency ratio determination (Tables 10.5, 10.6), from the tag-and-probe systematic (3%) and from T_{AA} are represented as the smaller error bar in the data points of Fig. 11.18. The common systematic uncertainty in Fig. 11.18 contains the *pp* luminosity measurement systematic (6%) and the *pp* yield systematic (2.3% for Υ(1S) and 3.3% for Υ(2S)), represented in Fig. 11.18 as the gray square at unity. For Fig. 11.20, however, the T_{AA} uncer-

tainty and *pp* luminosity uncertainty belong to the common systematic since it is the same for all the p_{T} and rapidity bins.

11.5.4 R_{AA} comparisons

A comparison of the centrality-dependent results with Υ(1S) and Υ(2S) R_{AA} with prompt J/ψ R_{AA}, Υ(1S) R_{AA}, and charged particle R_{AA} obtained from the 2010 data is shown in Fig. 11.21. The *pp* statistical error is treated as bin-to-bin error in the 2010 data while, in this analysis, it is designated as the common error. Comparisons of the Υ(1S) and Υ(2S) R_{AA} with the STAR experiment and with some theory predictions [50] are shown in Fig. 11.22, displaying a good compatibility. The black error bars in Fig. 11.21 and Fig. 11.22 are statistical error only. Both hydro model calculations describe the data.

The model shown in Fig. 11.22 (lower right) uses the rate-equation approach for the bottomonium production, the degree of suppression is a rather sensitive measure of color screening, together with the appropriate dissociation reactions. The significance of cold nuclear matter effects has been simulated by employing two nuclear absorption cross sections to estimate an upper and lower bound. For the LHC 0.0 and 2.0 mb are used to produce the bands seen in the plot. The regeneration component is calculated as "Total R_{AA}" - "Primordial R_{AA}". The resulting Υ(1S) R_{AA} agrees reasonably well with the CMS data in the strong-binding scenario, but is suppressed too much in the weak-binding scenario of Ref. [48]. On the other hand, Υ(2S) is strongly suppressed even in the former, with the observed yield ascribed to regeneration.

A comparison of the Υ(1S) and Υ(2S) nuclear modification factor R_{AA} as a function of centrality to the Υ(1S) R_{AA} measured in the forward rapidity range ($2.5<y<4$) by the ALICE experiment is given in figure Fig. 11.22 (lower left). The grey box at unity displays correlated systematic errors relative to the *pp* reference. On the right hand side a smaller panel is included, a comparing the centrality-integrated results.

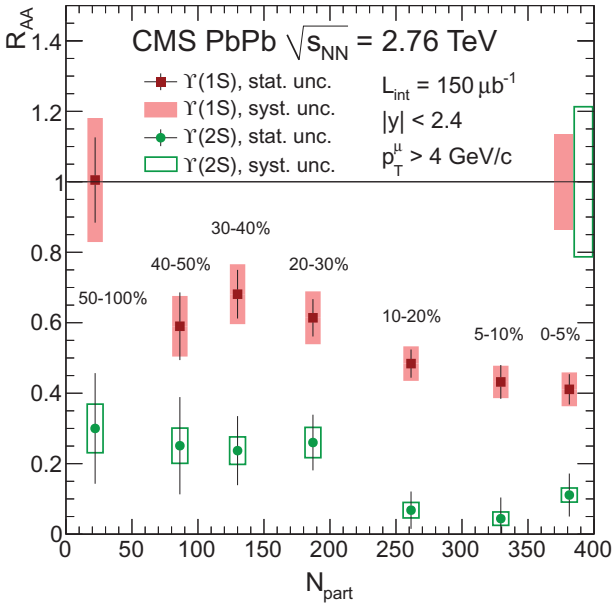

(a) default binning

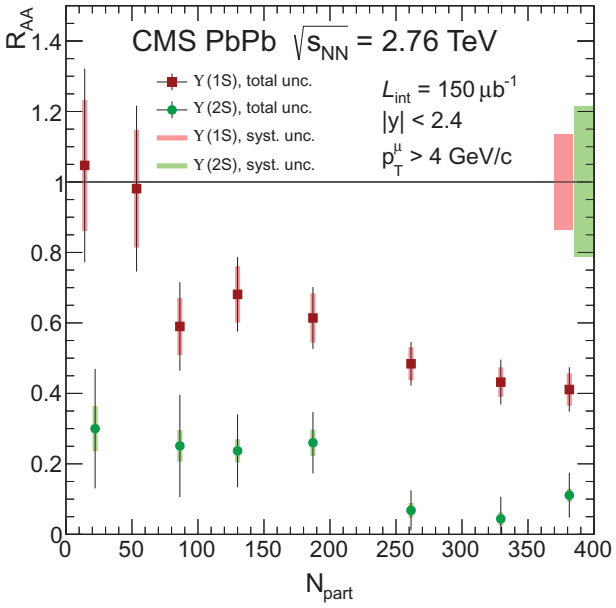

(b) most peripheral bin for Υ(1S) has been split into two centrality bins

Figure 11.18: Υ(1S) and Υ(2S) nuclear modification factors, R_{AA}, as a function of centrality. ($150\,\mu b^{-1}$)

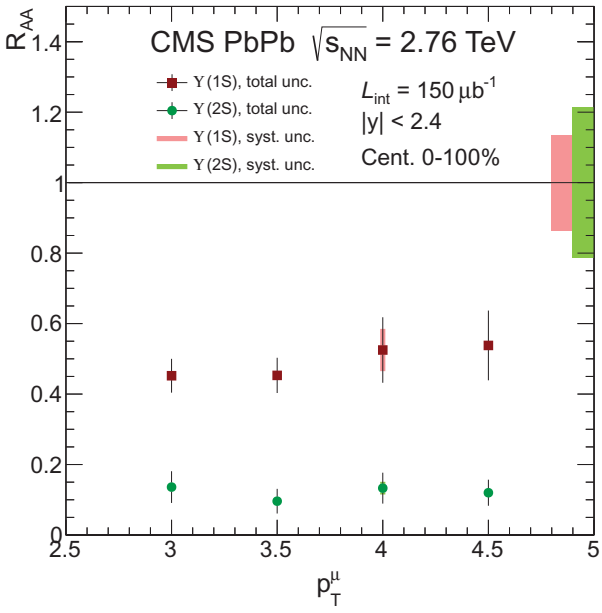

(a) Υ(1S) and Υ(2S) R_{AA} vs muon p_{T} cut

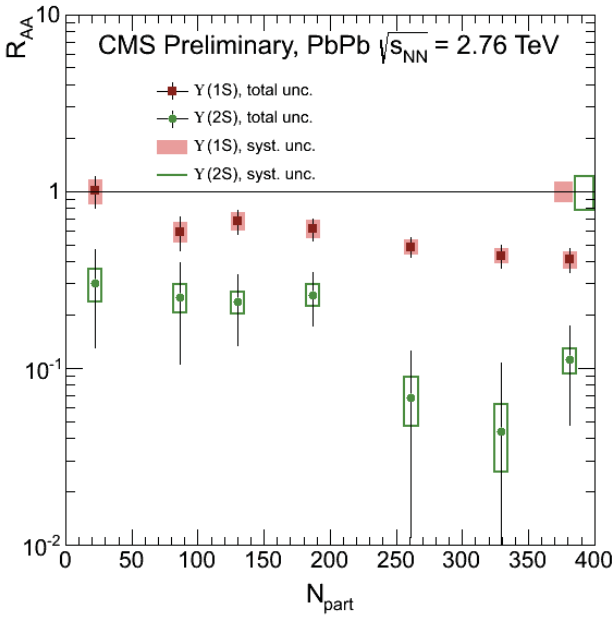

(b) Υ(1S) and Υ(2S) R_{AA} in log scale

Figure 11.19: Υ(1S) and Υ(2S) R_{AA} dependence on muon p_{T} cut (a). Below (b) is the R_{AA} in log scale.

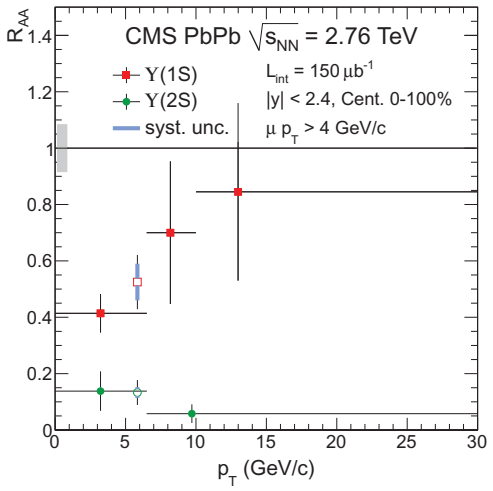

(a) p_{T}, stat. err. only

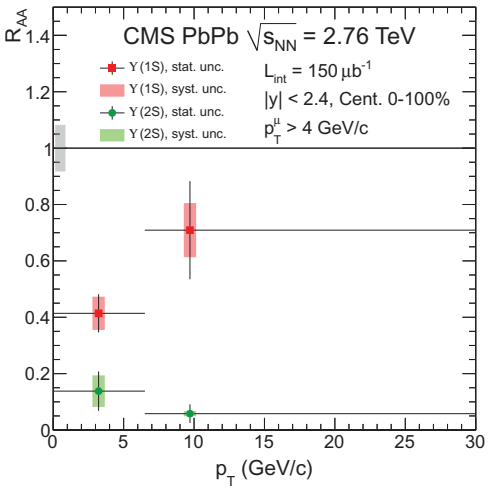

(b) p_{T}, with syst.

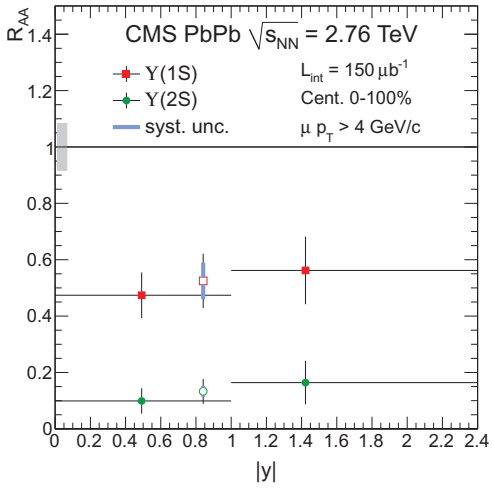

(c) rapidity, stat. err. only

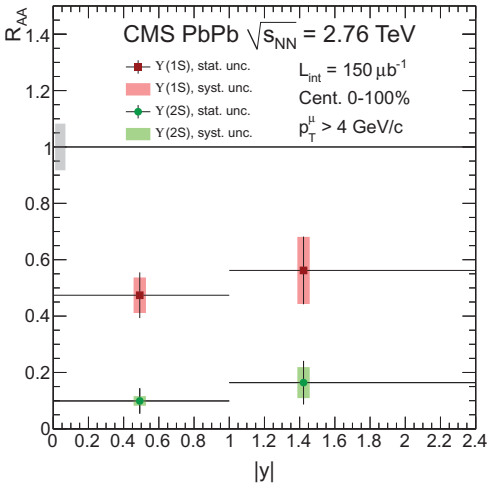

(d) rapidity, with syst.

Figure 11.20: Υ(1S) and Υ(2S) nuclear modification factors, R_{AA}, and their dependence on Υ p_{T} and rapidity. ($150\,\mu b^{-1}$)

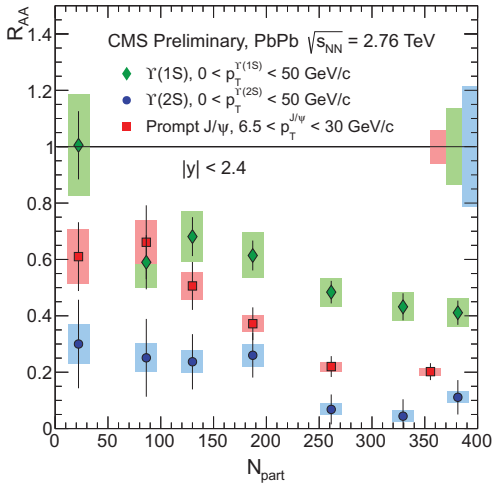

(a) Comparison of the Υ(1S) and Υ(2S) nuclear modification factor R_{AA} centrality dependence results with the 2010 J/ψ R_{AA}.

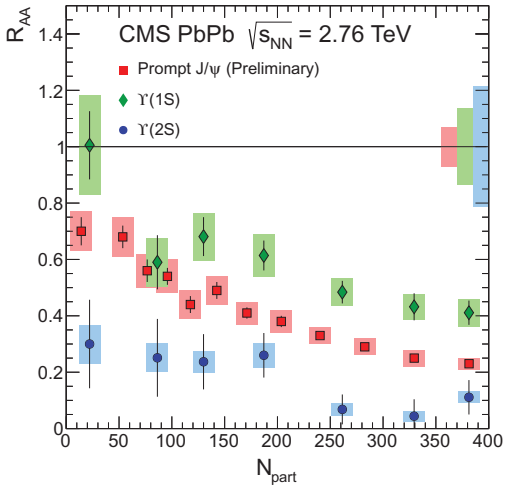

(b) Comparison of the Υ(1S) and Υ(2S) nuclear modification factor R_{AA} centrality dependence results with the 2011 J/ψ R_{AA}.

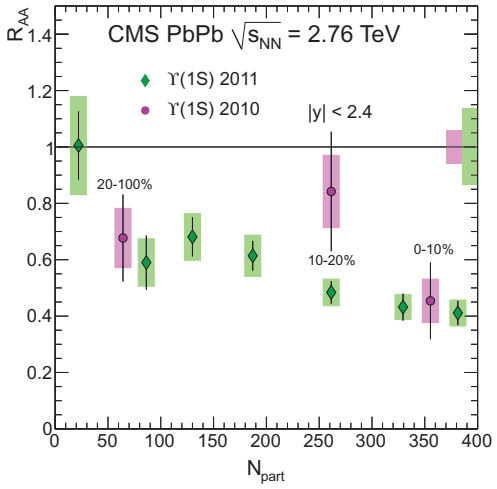

(c) Comparison of the Υ(1S) nuclear modification factor R_{AA} centrality dependence result with the 2010 Υ(1S) R_{AA}.

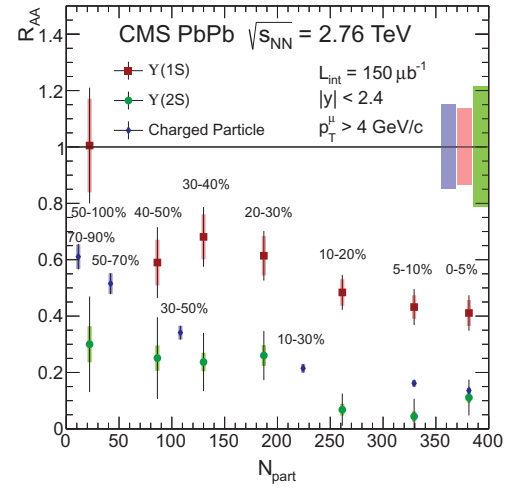

(d) Comparison with the 2010 charged particle R_{AA}

Figure 11.21: Comparison Υ(1S) and Υ(2S) R_{AA} with the 2010 Υ(1S), 2010 prompt J/ψ, 2011 prompt J/ψ, and 2010 charged particle R_{AA}.

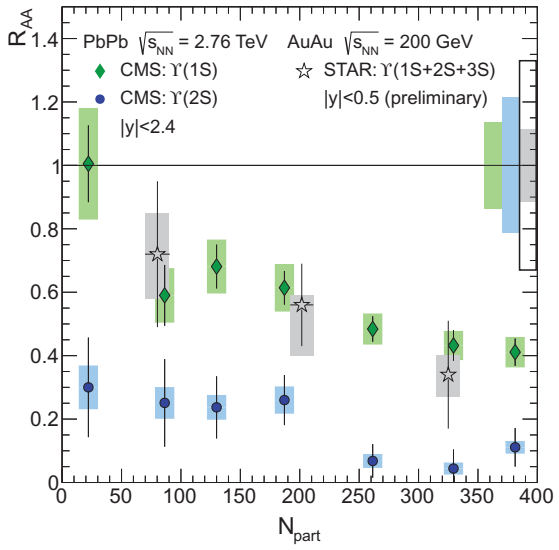

(a) Comparison of the Υ(1S) and Υ(2S) nuclear modification factor R_{AA} centrality dependence result to the Υ (nS) R_{AA} measurent by STAR.

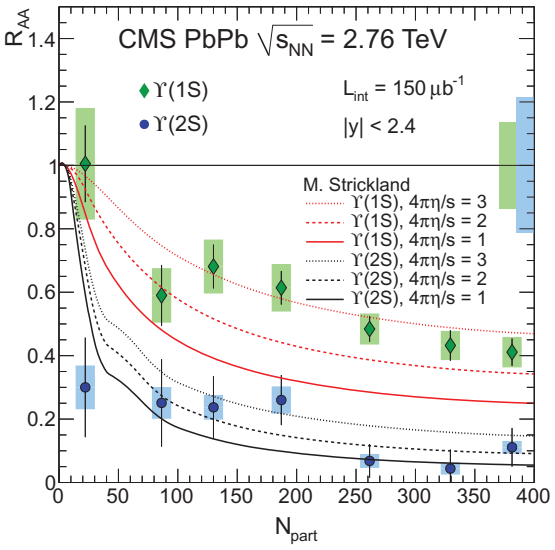

(b) Comparison of the Υ(1S) and Υ(2S) nuclear modification factor R_{AA} centrality dependence result to theory prediction M. Strickland [50].

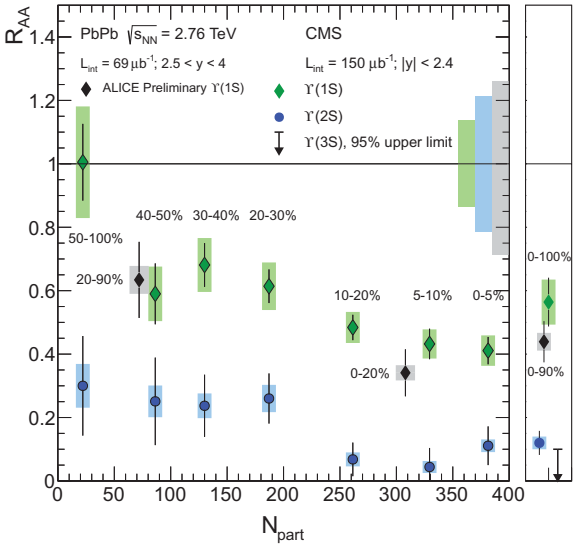

(c) Comparison of the Υ(1S) and Υ(2S) nuclear modification factor R_{AA} as a function of centrality to the ALICE results.

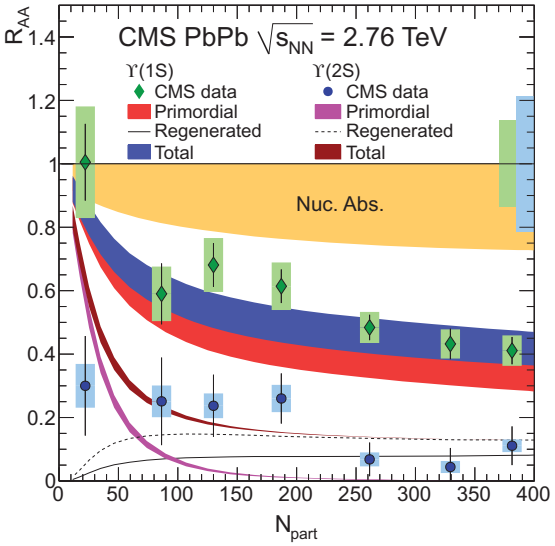

(d) Strong-binding scenario (SBS) prediction, produced using the calculations performed in the paper Eur. Phys. J. A48 (2012) 72 by Rapp et al. Ref. [48].

Figure 11.22: Comparison of the Υ(1S) R_{AA} results with the STAR and ALICE experiments and model predictions.

The nuclear modification factors are compared to prediction model for inclusive Υ(1S) and Υ(2S) suppression in Fig. 11.22 (upper right). The underlying calculations for this model employed a complex-valued potential which incorporates both screening and in-medium dissociation of the states under consideration. The model uses the resulting real and imaginary parts of the binding energy of the Υ(1S) and Υ(2S) states and folds this information together with the real-time evolution of both the typical momentum of the plasma particles ($p_{\rm hard}$) and their momentum-space anisotropy (ξ). The resulting inclusive suppression is in good agreement with the available data.

11.5.5 Υ(3S) R_{AA} upper limit

Once the R_{AA} for the Υ(3S) signal is extracted from the simultaneous maximum likelihood (ML) fit, we employ the Feldman-Cousins (FC) prescription to set a limit at 95% confidence level [38]. While the expected limit on the nuclear modification factor is close to a non-physical (≤ 0) result, the FC prescription guarantees a physically meaningful result and tells us how to smoothly transition from a one-sided to a two-sided limit. It uses a likelihood ratio as an ordering principle for selecting the acceptance region and creating confidence bands. The likelihood ratio is defined as:

$$Q(x) = \frac{P(x|R_{AA}(\Upsilon(3S))_0)}{P(x|R_{AA}(\Upsilon(3S))_{\rm max})}\,, \tag{11.9}$$

where $Q(x)$ is a likelihood ratio for a given $x = R_{AA}(\Upsilon(3S))$, $R_{AA}(\Upsilon(3S))_0$, and $R_{AA}(\Upsilon(3S))_{\rm max}$ are the $R_{AA}(\Upsilon(3S))$ likelihoods for the null hypoyhesis and maximum likelihood among all possible $R_{AA}(\Upsilon(3S))$ values respectively.

For the centrality-integrated bin (0 -100%) the computed upper limit on the nuclear modification factor, $R_{AA}(\Upsilon(3S))$, using the FC method is about 0.095 (95% CL). This can be seen from Fig. 11.23, when the observed CL_s (red dots) crosses the horizontal threshold (red line). We generate

1000 pseudo experiments at each scanned point to discriminate the null hypothesis (no signal 3S is present) from the alternative (signal plus background) hypothesis.

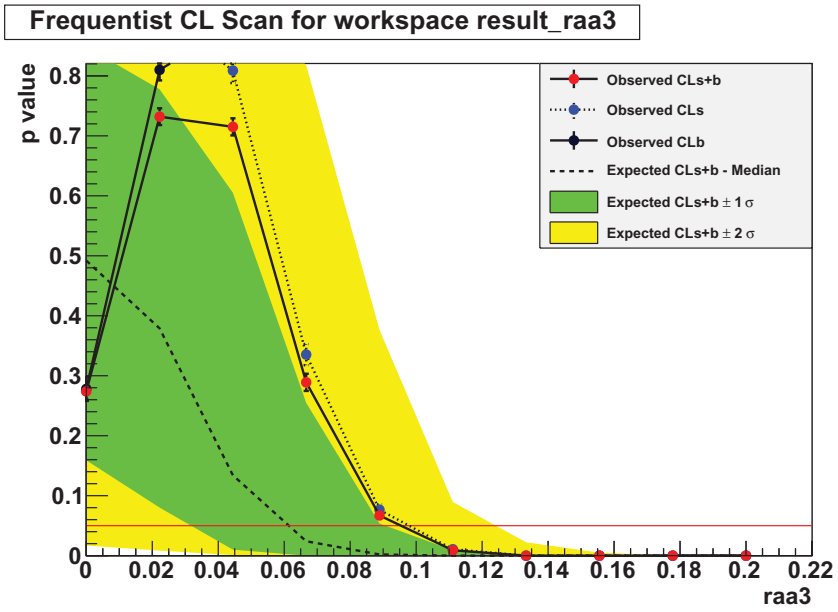

Figure 11.23: p-value scan for $R_{AA}(\Upsilon(3S))$ using the Feldman-Cousins technique.

The systematic uncertainties on the pp luminosity, the nuclear overlap function T_{AA} and the efficiency ratios as well as the uncertainties on the background shape and the signal FSR need to be taken into consideration when setting the upper limit. We fold in these systematics, which were previously specified, via nuisance parameters in the fit.

Figure 11.25 shows cross checks using the profile likelihood ratio implementation, where an $R_{AA}(\Upsilon(3S))$ upper limit of about 0.0952 (95% CL) is obtained. Notice that both results are consistent within uncertainties. The results for the two implementations are summarized in Table 11.14.

Since we are interested in the suppression pattern of the three Υ states and because the errors for the R_{AA} for the $\Upsilon(1S)$ and $\Upsilon(2S)$ have been calculated with a 1 σ error, we also set the upper limits at a 68% confidence level.

In this scenario, the upper limit obtained using the Feldman Cousins technique is

$R_{AA}(\Upsilon(3S)) \leq 0.064 \pm 0.001$ at 68% confidence level.

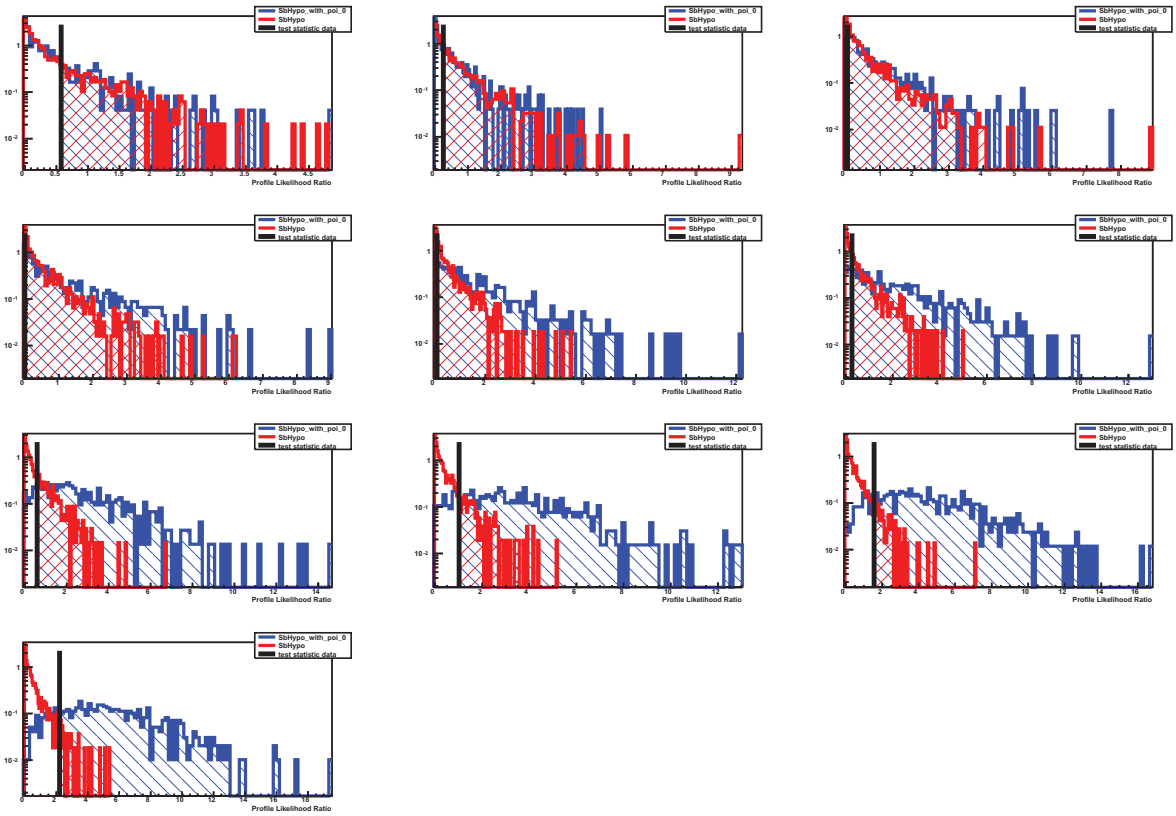

(a) Pseudo-experiments for null and alternative hypotheses and using likelihood ratio test statistics.

Figure 11.24: A thousand pseudo-experiments for each of the ten points in the p-value scan alternative hypothesis H_{sb} (red curve), the null hypothesis H_b (blue curve) and the test statatistic (black line). As we increase our parameter of interest it is easier to differentiate between the two hypotheses and the area under the red curve becomes smaller than the area under the blue curve.

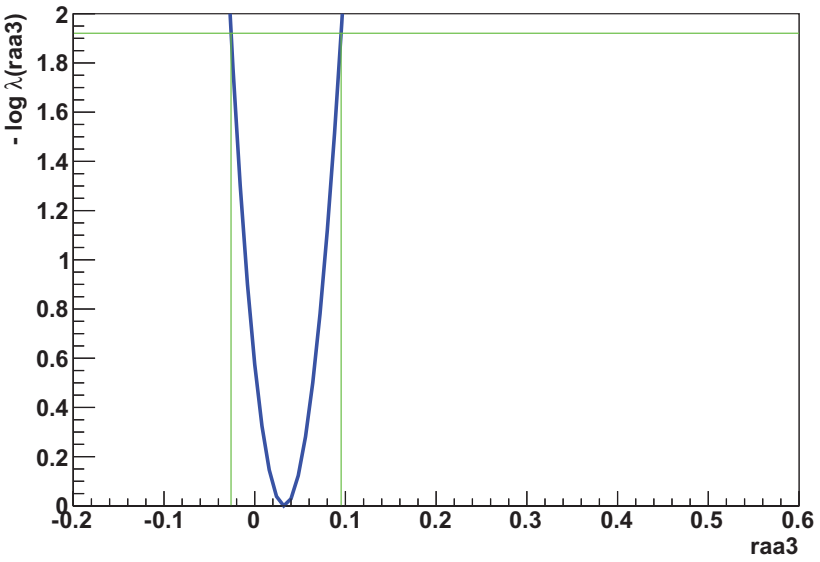

Figure 11.25: Profiled likelihood ratio. It shows the confidence interval at 95% confidence level.

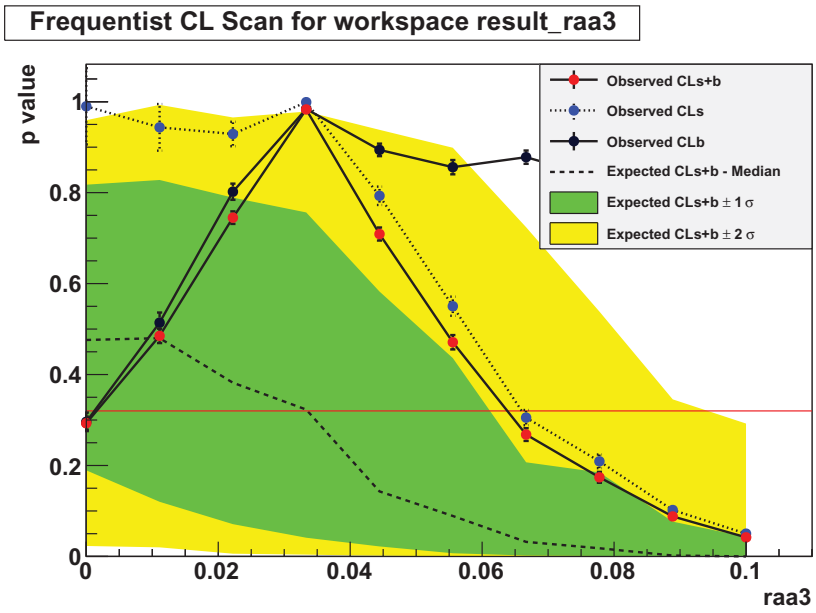

Figure 11.26: p-value scan for $R_{AA}(\Upsilon(3S))$ using the Feldman-Cousins technique at 68% confidence level.

11.6 Sequential suppression

Finally, since we have measured the individual nuclear modification factors for all resonances we can observe the suppression pattern ordered as $\Upsilon(1S) > \Upsilon(2S) > \Upsilon(3S)$, and increases with the centrality of the PbPb collision. If we add measured R_{AA} values for other quarkonia states we could build a hierarchy of a suppression. We notice that this hierarchy is in total agreement with the sequential suppression model we have discussed previously and the order of dissapeareance of the resonances is preserved according to their binding energies at T = 0 as can be seen in Fig. 11.27. The individual $\Upsilon(1S)$, $\Upsilon(2S)$, and $\Upsilon(3S)$ states have been observed to be suppressed by factors of about 2, 8, and larger than 10, respectively.

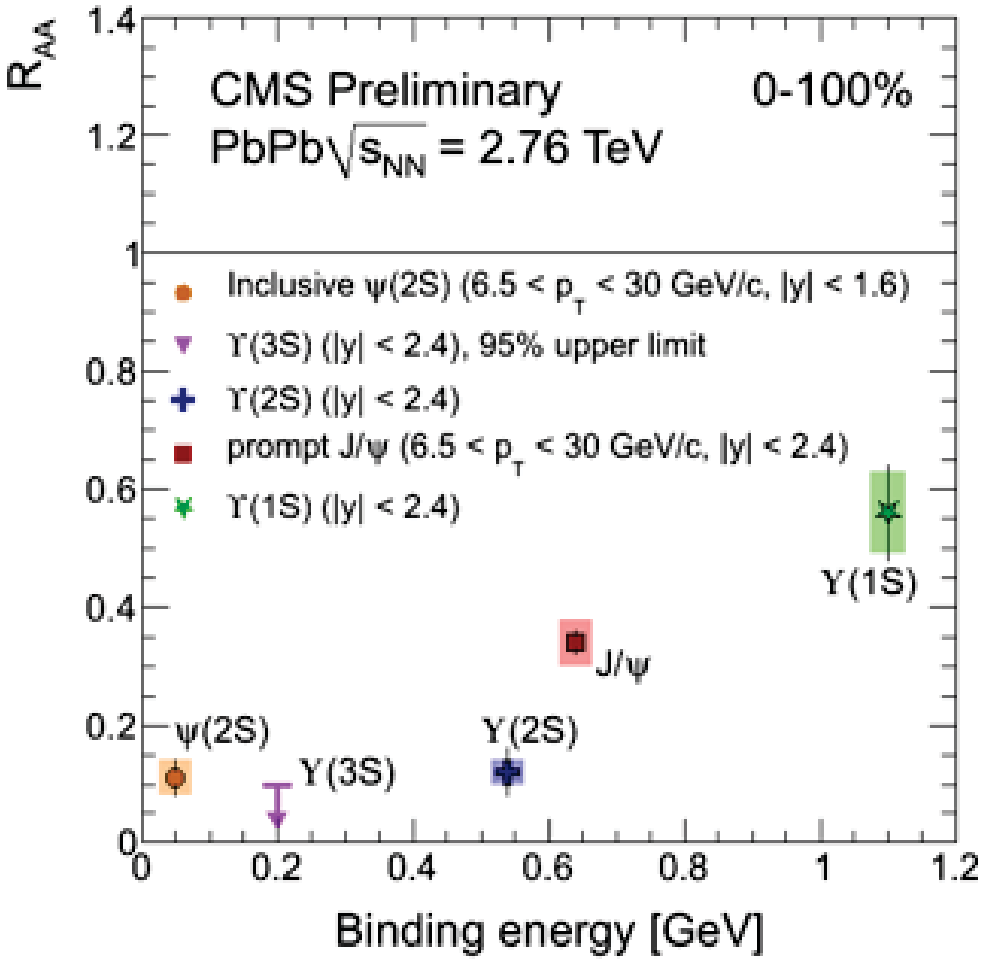

(a) Comparison of the Υ(1S), Υ(2S) and Υ(3S) nuclear modification factor R_{AA} integrated over centrality with other quarkonium states measured with CMS detector. Kinematic regions are not necessarily the same

Figure 11.27: Sequential suppression pattern for different states according to their binding energies.

Table 11.4: Double-ratio results.

		$p_{\mathrm{T}}^{\mu} > 4.0\,\mathrm{GeV}/c$, Cent. 0-100%		
		χ_{23}	χ_2	χ_3
nominal result		0.15 ± 0.05	0.21 ± 0.07	0.06 ± 0.06
signal pdf systematic variations:				
fix CB tail to MC		0.135 ± 0.047	0.200 ± 0.066	0.063 ± 0.054
fix resolution to MC		0.153 ± 0.049	0.217 ± 0.070	0.081 ± 0.063
fix CB and resolution to MC		0.144 ± 0.047	0.207 ± 0.067	0.000 ± 0.000
separated floating CB tail		0.166 ± 0.052	0.226 ± 0.070	0.098 ± 0.058
separated floating resolution		0.149 ± 0.048	0.215 ± 0.070	0.080 ± 0.064
separated CB tail and resolution		0.163 ± 0.048	0.223 ± 0.064	0.098 ± 0.063
shared mean		0.150 ± 0.048	0.219 ± 0.064	0.076 ± 0.062
background pdf systematic variations:				
PbPb model	*pp* model			
LS Erf*Exp + pol.2;	pol.2	0.157 ± 0.047	0.220 ± 0.070	0.075 ± 0.064
LS keys + pol.2;	pol.2	0.161 ± 0.049	0.223 ± 0.071	0.040 ± 0.061
OS TrkRot Erf*Exp + pol.2;	pol.2	0.157 ± 0.047	0.221 ± 0.070	0.094 ± 0.067
OS TrkRot keys + pol.2;	pol.2	0.164 ± 0.050	0.215 ± 0.069	0.070 ± 0.062
LS keys + pol.2;	LS keys + pol.2	0.167 ± 0.053	0.234 ± 0.076	0.042 ± 0.065
LS Erf*Exp + pol.2;	LS Erf*Exp + pol.2	0.158 ± 0.048	0.222 ± 0.071	0.075 ± 0.046
Erf*Exp;	Erf*Exp	0.153 ± 0.050	0.219 ± 0.071	0.079 ± 0.068
Erf*Exp;	Erf*Exp(shared erf)	0.143 ± 0.045	0.216 ± 0.066	0.070 ± 0.062
Erf*Exp;	LS Erf*Exp + pol.2	0.148 ± 0.049	0.215 ± 0.071	0.075 ± 0.046
Erf*Exp;	LS keys + pol.2	0.155 ± 0.043	0.224 ± 0.063	0.081 ± 0.069
Total systematic from fit (RMS of all the fit variations):				
Fit relative systematic		7.6%	4.0%	46.8%
Fit absolute systematic		0.01	0.01	0.03
Total systematic from fit(take the largest one from equivalent variations):				
Fit relative systematic		19.3%	11.7%	100.6%
Fit absolute systematic		0.03	0.02	0.06
systematic from efficiency		1.0%	1.0%	1.0%
Total systematic:				
Total relative systematic		19.3%	11.8%	100.6%
Total absolute systematic		0.03	0.02	0.06
other checks:				
LS TrkRot Erf*Exp + pol.2;	pol.2	0.170 ± 0.049	0.236 ± 0.072	0.061 ± 0.080
LS TrkRot keys + pol.2;	pol.2	0.168 ± 0.048	0.232 ± 0.072	0.088 ± 0.066

Table 11.5: R_{AA} significance computed with profile likelihood ratio

null hypothesis	nominal fit -log(L)	null hypothesis fit -log(L)
$\Upsilon(1S)R_{AA}=1, \Upsilon(2S)R_{AA}=1, \Upsilon(3S)R_{AA}=1$	-79618.2	-79586.2
$\Upsilon(2S)R_{AA}=1, \Upsilon(3S)R_{AA}=1$	-79618.2	-79590.9
$\Upsilon(1S)R_{AA}=1$	-79618.2	-79611.4
$\Upsilon(1S)R_{AA}=1$,centrality$<10\%$	-28215.3	-28204.1
null hypothesis	significance	
$\Upsilon(1S)R_{AA}=1, \Upsilon(2S)R_{AA}=1, \Upsilon(3S)R_{AA}=1$	7.4σ	
$\Upsilon(2S)R_{AA}=1, \Upsilon(3S)R_{AA}=1$	7.1σ	
$\Upsilon(1S)R_{AA}=1$	3.7σ	
$\Upsilon(1S)R_{AA}=1$,centrality$<10\%$	4.7σ	

Table 11.6: Υ(1S), Υ(2S) and Υ(3S) raw yields for the PbPb dataset versus centrality.

centrality	$\Upsilon(1S) \pm$ stat. $\pm$ syst.	$\Upsilon(2S) \pm$ stat. $\pm$ syst.	$\Upsilon(3S) \pm$ stat. $\pm$ syst.
0-5%	$237 \pm 25 \pm 21$	$32.0 \pm 17.6 \pm 4.6$	
5-10%	$199 \pm 22 \pm 12$	$10.1 \pm 14.0 \pm 4.2$	
10-20%	$329 \pm 27 \pm 21$	$22.7 \pm 17.9 \pm 6.9$	
20-30%	$253 \pm 22 \pm 19$	$54.1 \pm 16.4 \pm 6.2$	
30-40%	$169 \pm 17 \pm 11$	$29.1 \pm 12.0 \pm 2.8$	
40-50%	$80 \pm 13 \pm 6$	$16.8 \pm 9.2 \pm 2.2$	
50-100%	$116 \pm 14 \pm 7.5$	$17.6 \pm 9.2 \pm 2.4$	
50-60%	$65 \pm 11 \pm 4$		
60-100%	$51.3 \pm 9.9 \pm 4$		
0-100%	$1317 \pm 73 \pm 85$	$156 \pm 38 \pm 14.5$	$31.5 \pm 33.5 \pm 4.3$

Table 11.7: Υ(1S), Υ(2S) and Υ(3S) raw yields for the *pp* dataset versus centrality.

	$\Upsilon(1S) \pm$ stat. $\pm$ syst.	$\Upsilon(2S) \pm$ stat. $\pm$ syst.	$\Upsilon(3S) \pm$ stat. $\pm$ syst.
pp data	$88 \pm 11 \pm 2$	$49 \pm 10 \pm 2$	$36 \pm 9 \pm 2$

Table 11.8: Υ(1S) and Υ(2S) raw yields versus p_{T} and rapidity. Only statistical uncertainties are shown.

	PbPb Υ(1S)	PbPb Υ(2S)	*pp* Υ(1S)	*pp* Υ(2S)
$0 < p_{\mathrm{T}} < 6.5$	826.5 ± 64.8	86.8 ± 33.7	73.8 ± 10.6	23.1 ± 7.5
$6.5 < p_{\mathrm{T}} < 10$	259.6 ± 37.3	11.9 ± 17.0	14.1 ± 4.7	9.1 ± 4.3
$10 < p_{\mathrm{T}} < 30$	222.6 ± 21.6	24.1 ± 10.6	10.1 ± 3.6	14.2 ± 4.4
$6.5 < p_{\mathrm{T}} < 30$	466.4 ± 37.9	36.5 ± 18.8	24.7 ± 5.7	24.0 ± 6.0
$0 < \lvert y \rvert < 1$	665.1 ± 47.8	65.5 ± 24.3	53.0 ± 8.2	25.2 ± 6.5
$1 < \lvert y \rvert < 2.4$	744.2 ± 72.7	106.7 ± 34.9	49.8 ± 9.5	24.1 ± 8.1

Table 11.9: Systematics of the Υ(1S), Υ(2S) and Υ(3S) nuclear modification factors (in percent).

	MC eff.	TnP	PbPb fit	T_{AA}	*pp* fit	pp luminosity
Υ(1S)	5.36	3	6.5	5.7	2.3	6
Υ(2S)	5.45	3	9.3	5.7	3.3	6
Υ(3S)	5.45	3	13.7	5.7	4.2	6

Table 11.10: Systematics of the Υ(1S) and Υ(2S) nuclear modification factors for centrality bins (in percent).

	Υ(1S)				Υ(2S)			
$N_{\rm part}$ (centrality)	MC eff.	T&P	PbPb fit	T_{AA}	MC eff.	TnP	PbPb fit	T_{AA}
381 (0- 5%)	5.15	3	8.9	4.1	5.68	3	14.4	4.1
329 (5- 10%)	6.64	3	6.0	4.6	5.71	3	41.6	4.6
261 (10- 20%)	4.77	3	6.4	5.2	5.46	3	30.4	5.2
187 (20- 30%)	5.90	3	7.5	6.6	4.98	3	11.5	6.6
130 (30- 40%)	5.36	3	6.5	8.5	5.19	3	9.6	8.5
86 (40- 50%)	5.18	3	7.5	10.9	4.74	3	13.1	10.9
22 (50-100%)	5.26	3	6.5	15.0	4.86	3	14.2	15.0
54 (50- 60%)	5.00	3	6.2	15.0				
14 (60-100%)	5.39	3	7.8	15.0				

Table 11.11: The Υ(1S), Υ(2S) and Υ(3S) nuclear modification factors, R_{AA}, as a function of centrality.

$N_{\rm part}$ (centrality)	Υ(1S) $\pm$ syst. $\pm$ stat.	Υ(2S) $\pm$ syst. $\pm$ stat.	Υ(3S) $\pm$ syst. $\pm$ stat.
381 (0- 5%)	$0.41 \pm 0.05 \pm 0.04$	$0.11 \pm 0.02 \pm 0.06$	
329 (5- 10%)	$0.43 \pm 0.05 \pm 0.05$	$0.04 \pm 0.02 \pm 0.06$	
261 (10- 20%)	$0.48 \pm 0.05 \pm 0.04$	$0.07 \pm 0.02 \pm 0.05$	
187 (20- 30%)	$0.61 \pm 0.08 \pm 0.05$	$0.26 \pm 0.04 \pm 0.08$	
130 (30- 40%)	$0.68 \pm 0.09 \pm 0.07$	$0.24 \pm 0.04 \pm 0.10$	
86 (40- 50%)	$0.59 \pm 0.09 \pm 0.10$	$0.25 \pm 0.05 \pm 0.14$	
22 (50-100%)	$1.01 \pm 0.18 \pm 0.12$	$0.30 \pm 0.07 \pm 0.16$	
54 (50- 60%)	$0.98 \pm 0.17 \pm 0.17$		
14 (60-100%)	$1.05 \pm 0.19 \pm 0.20$		
114 (0-100%)	$0.56 \pm 0.07 \pm 0.08$	$0.12 \pm 0.02 \pm 0.04$	$0.03 \pm 0.01 \pm 0.04$

Table 11.12: The Υ(1S), Υ(2S) and Υ(3S) nuclear modification factors systematic as a function of $p_{\rm T}$ and rapidity (in percent).

	MC eff.	T&P	PbPb fit	T_{AA}	pp fit	pp lumi
Υ(1S), $0 < p_{\rm T} < 6.5$	3.46	3	8.1	5.7	6.7	6
Υ(1S), $6.5 < p_{\rm T} < 30$	6.52	3	6.6	5.7	4.8	6
Υ(1S), $0 < \lvert y \rvert < 1$	3.20	3	7.0	5.7	6.3	6
Υ(1S), $1 < \lvert y \rvert < 2.4$	4.79	3	14.7	5.7	11.5	6
Υ(2S), $0 < p_{\rm T} < 6.5$	4.78	3	38.8	5.7	7.0	6
Υ(2S), $6.5 < p_{\rm T} < 30$	6.71	3	8.3	5.7	4.6	6
Υ(2S), $0 < \lvert y \rvert < 1$	2.71	3	12.9	5.7	7.5	6
Υ(2S), $1 < \lvert y \rvert < 2.4$	4.85	3	27.7	5.7	15.6	6
Υ(3S), $0 < \lvert y \rvert < 2.4$	5.45	3	13.7	5.7	4.2	6

Table 11.13: The Υ(1S) and Υ(2S) nuclear modification factors, R_{AA} as a function of $p_{\rm T}$ and rapidity.

	Υ(1S) $\pm$ stat. $\pm$ syst.	Υ(2S) $\pm$ stat. $\pm$ syst.
$0 < p_{\rm T} < 6.5$	$0.41 \pm 0.07 \pm 0.06$	$0.14 \pm 0.07 \pm 0.06$
$6.5 < p_{\rm T} < 10$	0.70 ± 0.25	0.05 ± 0.07
$10 < p_{\rm T} < 30$	0.85 ± 0.32	0.06 ± 0.03
$6.5 < p_{\rm T} < 30$	$0.71 \pm 0.17 \pm 0.10$	$0.06 \pm 0.03 \pm 0.01$
$0 < \lvert y \rvert < 1$	$0.47 \pm 0.08 \pm 0.06$	$0.10 \pm 0.05 \pm 0.02$
$1 < \lvert y \rvert < 2.4$	$0.56 \pm 0.12 \pm 0.12$	$0.16 \pm 0.08 \pm 0.06$

Table 11.14: $R_{AA}(\Upsilon(3S))$ upper limits.

		95% C.L upper limit	
centrality	best fit value	Feldman-Cousins	profile likelihood ratio
0 - 100%	0.032 ± 0.031	0.09506 ± 0.00130	0.0952

Chapter 12

Initial Central Temperatures

Given our results for the ratio of the Υ(1S) nuclear modification factor we can extract the intial temperature of the plasma. The Υ(1S) binding (disassociation) energy at $T = 0$ is on the order of 1 GeV.

Since the R_{AA} for the Υ(1S) is inclusive we can extract an "average" temperature of the plasma.

To connect to the initial temperature we use ideal hydrodynamics with a Gaussian overlap profile in the case of central collisions and ignore transverse expansion. Then we average over the transverse direction analytically and over proper-time to compute the average temperature as a function of the initial central temperature.

First, we extract the central temperature using a parameterization of the R_{AA} as a function of T from model predictions [50]. Here we describe the hydro model used by Strickland. The uncertainties in the model come from variations of the parameter η/s which gives upper and lower bounds in the values of the nuclear modification factor. The function used to parameterize the data can not be negative at large "T". Since we wish to extrapolate far beyond the fit region to "T" $\sim$ 1 GeV we use Eq. (12.1). We also expect that the curve has an inflection point so that it goes to zero smoothly. Instead of a polynomial fit the function is defined as:

$$R_{AA} = \alpha \exp \beta \left(\frac{T}{T_c} \right)^{\gamma} \tag{12.1}$$

Notice at $T = 0$ the nuclear modification factor is $R_{AA}^{\Upsilon(1S)} = 1$. From the parameterization and using the measured R_{AA} in most central collisions $R_{AA}^{central} = 0.41$, we extract a value of $T = 0.54\,\mathrm{GeV}$.

Since we have extracted an "average" temperature for the plasma we can calculate the binding or disassociation energy for the $\Upsilon(1S)$ using simulated data from Ref [50]. We fit the model using:

$$R_{AA} = V_0 \exp \left(-\lambda \frac{T}{T_c} \right) + \delta \tag{12.2}$$

where V_0 is the binding energy at $T = 0$, for $\Upsilon(1S)$ $T \sim 1.1\,\mathrm{GeV}$ and λ is the exponential decal. The exponential decay is well motivated by the form of the screening potential in quenched QCD lattice studies. Fiting the simulated data points in the region of interest and extrapolating to $T = 0$ we find the dissoaciation potential (binding energy) of the $V_0 = 1.13\,\mathrm{GeV}$

Finally we can encapsulate both results into one single figure, Fig. 12.4.

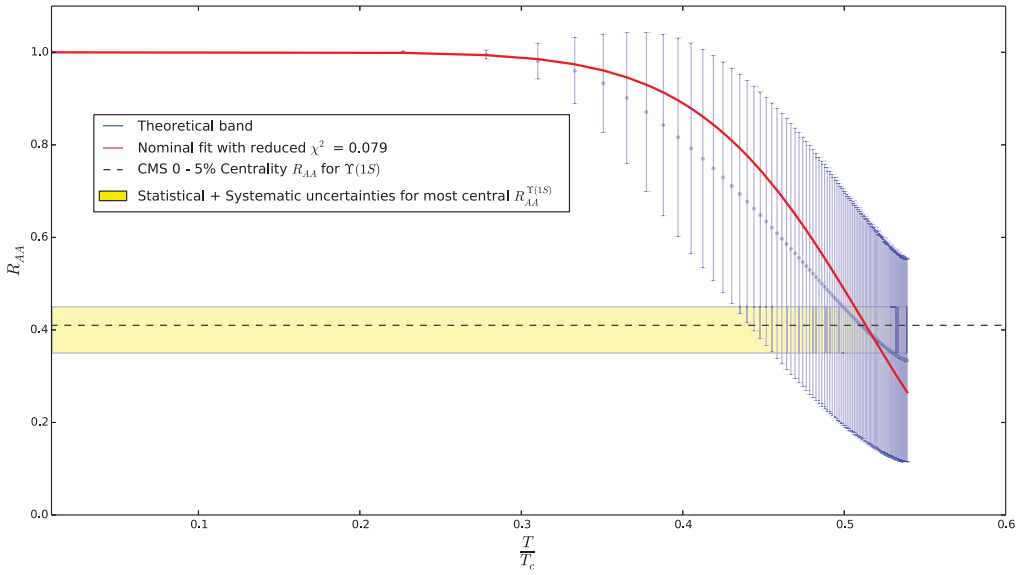

(a) Exponential fit.

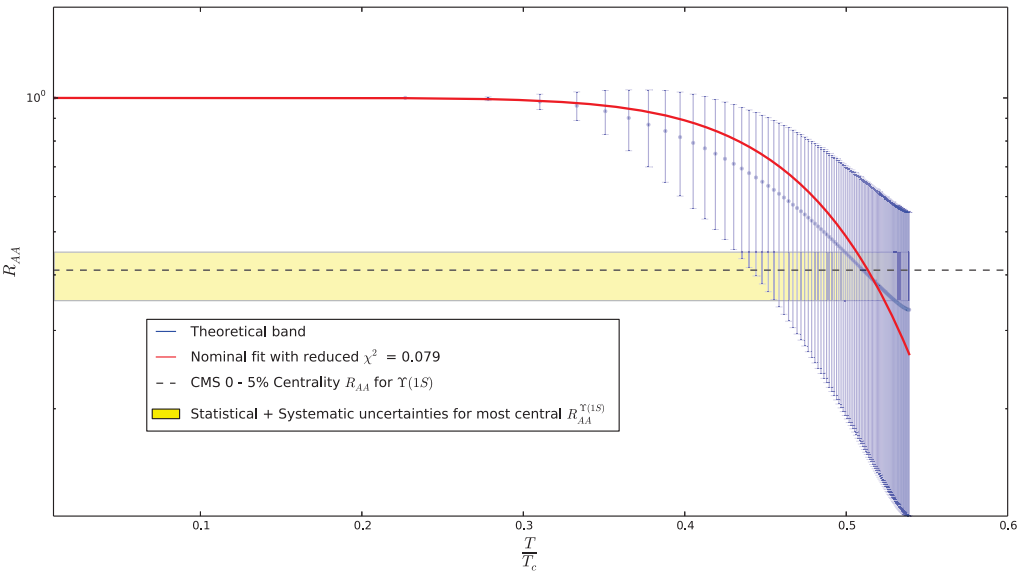

(b) Exponential fit in log scale.

Figure 12.1: Fit to the Dissociation energy vs T/T_c. The parameters $B_0, \lambda,$ and δ are free.

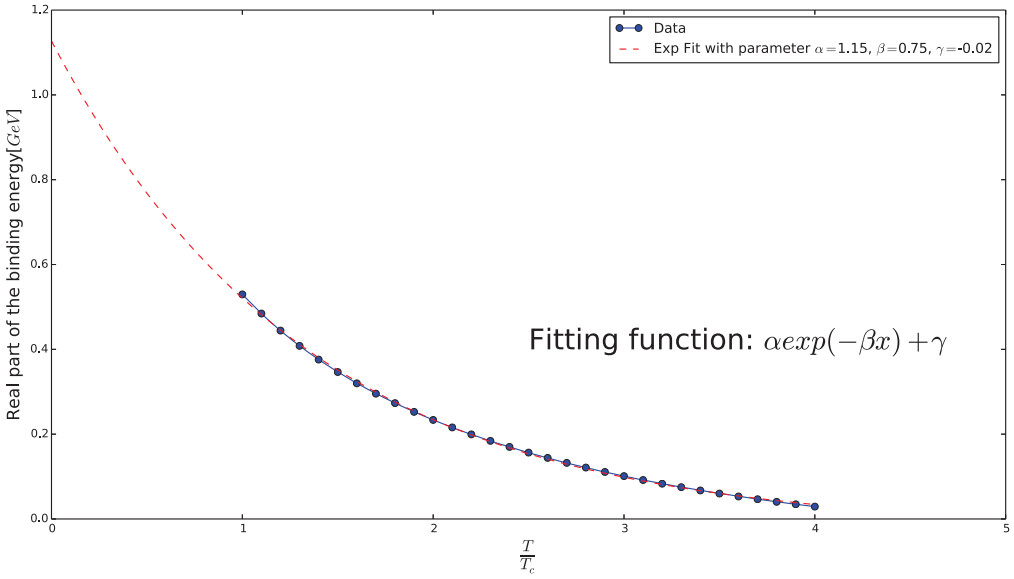

(a) Exponential fit.

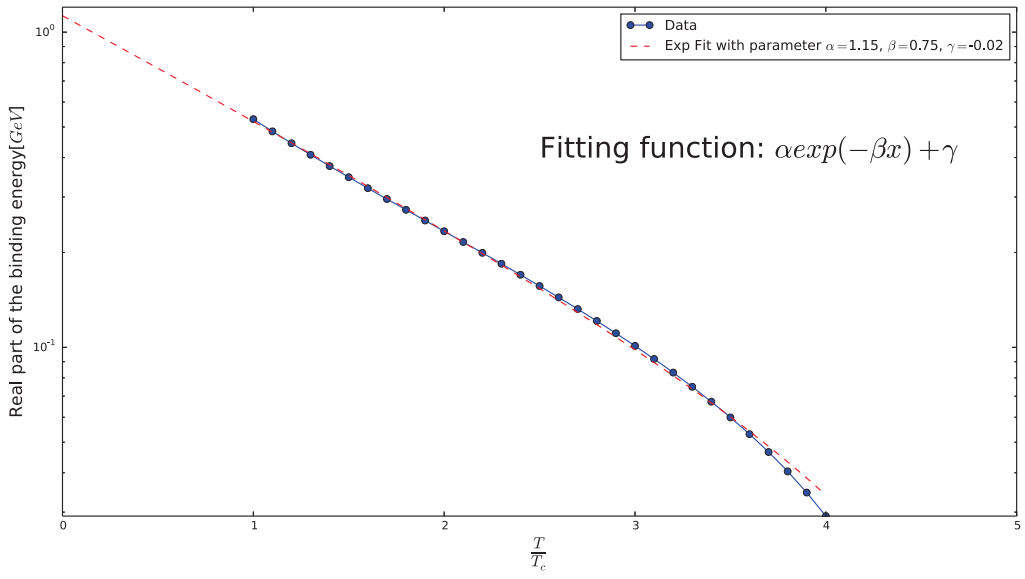

(b) Exponential fit in log scale.

Figure 12.2: Fit to the R_{AA} vs T/T_c. The parameters $\alpha, \beta,$ and γ are free

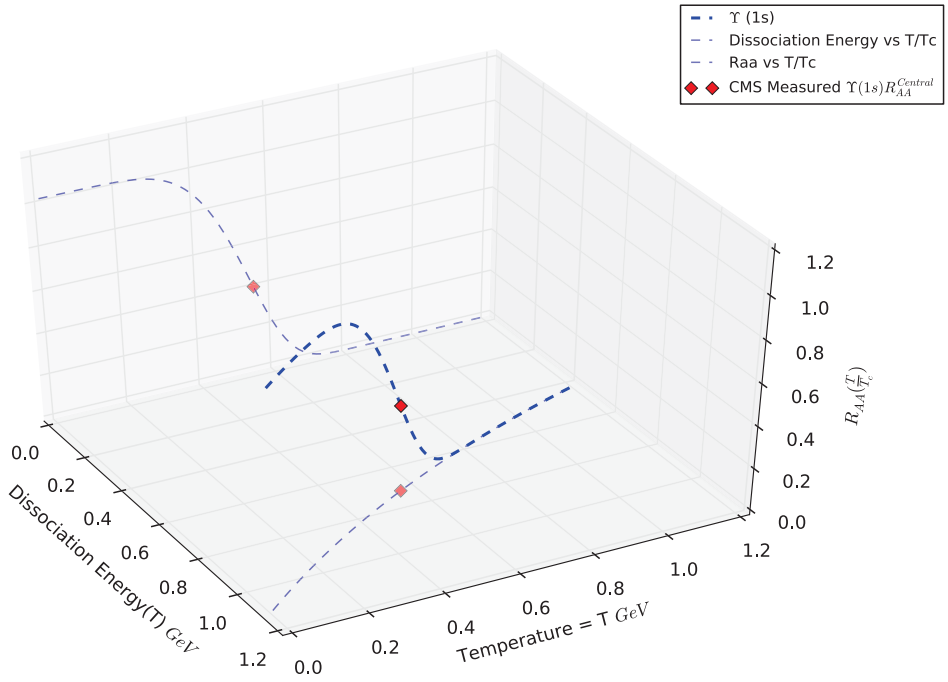

Figure 12.3: R_{AA} and dissociation energy as a function of and . The measured R_{AA} of the Υ(1S) yields an "average" central temperature of 0.54 GeV.

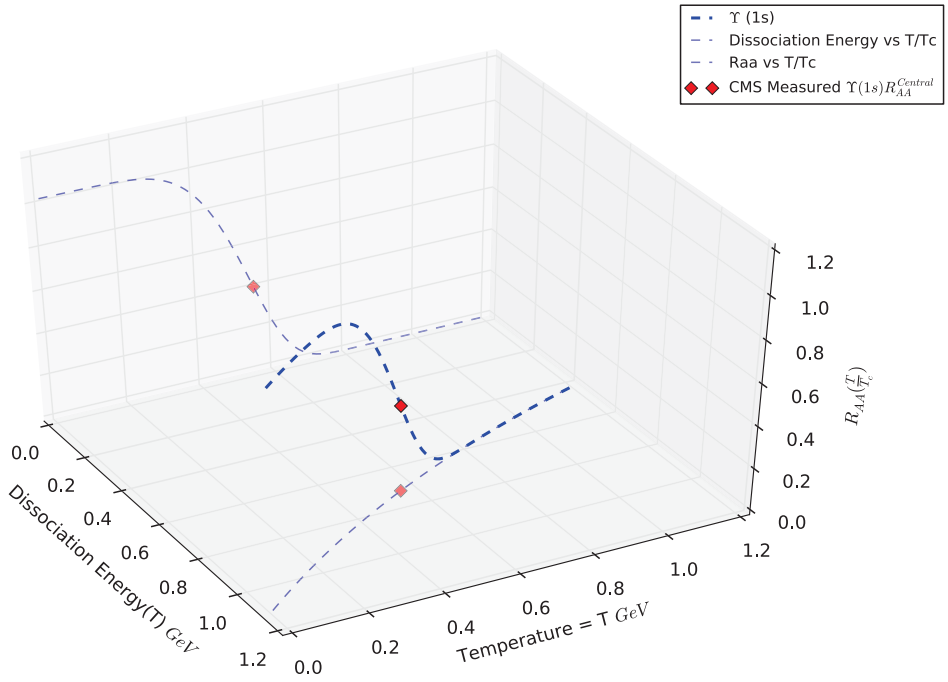

Figure 12.4: R_{AA} and dissociation energy as a function of T/T_c. The measured R_{AA} of the Υ(1S) yields an "average" central temperature of 0.54 GeV.

Chapter 13

Conclusions

The relative suppression of the Υ excited states has been measured, based on the first 150 μb^{-1} of the 2011 PbPb dataset. The observed results ($\chi_2 \equiv 2S/1S = 0.21 \pm 0.07 \pm 0.02$ and $\chi_{23} \equiv (2S + 3S)/1S = 0.15 \pm 0.05 \pm 0.02$) are considerably more precise than, and compatible with, the published measurements based on the 2010 PbPb dataset. Profile-likelihood based estimations show the significance of the relative excited-to-ground state suppression is larger than $5\,\sigma$. The larger luminosity of the PbPb dataset further allows us to carry out the measurement in bins of the dimuon kinematics and the collision centrality. No definitive trend is identified with the current precision. A clear dependence on the collision centrality is observed for the nuclear modification factors for the individual $\Upsilon(1S)$. The $\Upsilon(3S)$ state is not prominent in the PbPb data, consistent with being fully suppressed. Upper limits on its double ratio and its nuclear modification factor were extracted. The upper limits on the 3S/1S double ratio and nuclear modification factor were set at 95% Confidence Level.

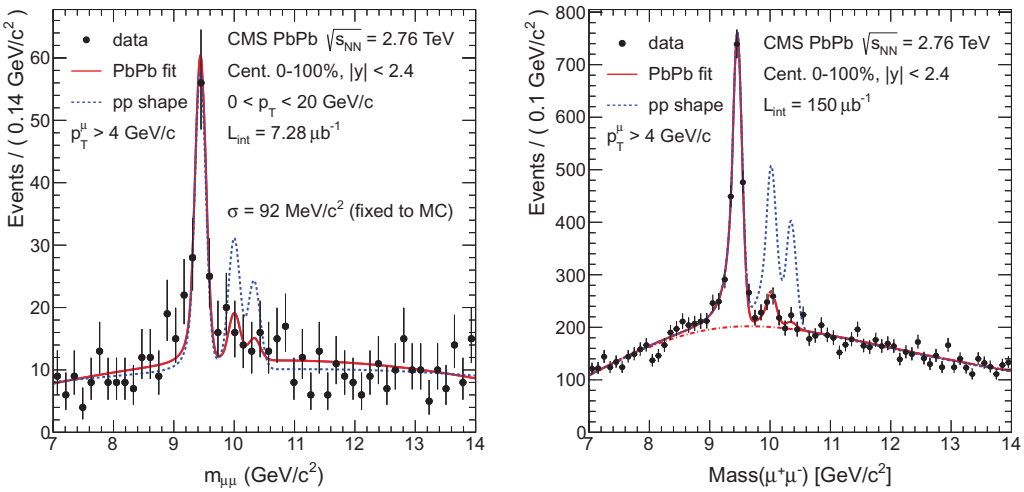

(a) 2010 (b) 2011

Figure 13.1: Illustration of the excited to ground states relative Υ suppression in PbPb compared to *pp*, and comparison of the effect observed using the 2010 *(left)* and 2011 *(right)* PbPb datasets. The fit to the PbPb data, shown by the continuous line, is overlaid with the result of the *pp* fit, represented by the dashed line (shown on top of a common PbPb background shape, for comparison). For a better comparison, the background shape, background yield, mass peak width, mass peak tail shape and the Υ(1S) yields in the red line are fixed to the PbPb fit, while the Υ(2S) /Υ(1S) and Υ(3S) /Υ(1S) ratios are fixed to the *pp* fit values. These plots are provided for illustration, and do not reflect the analysis details.

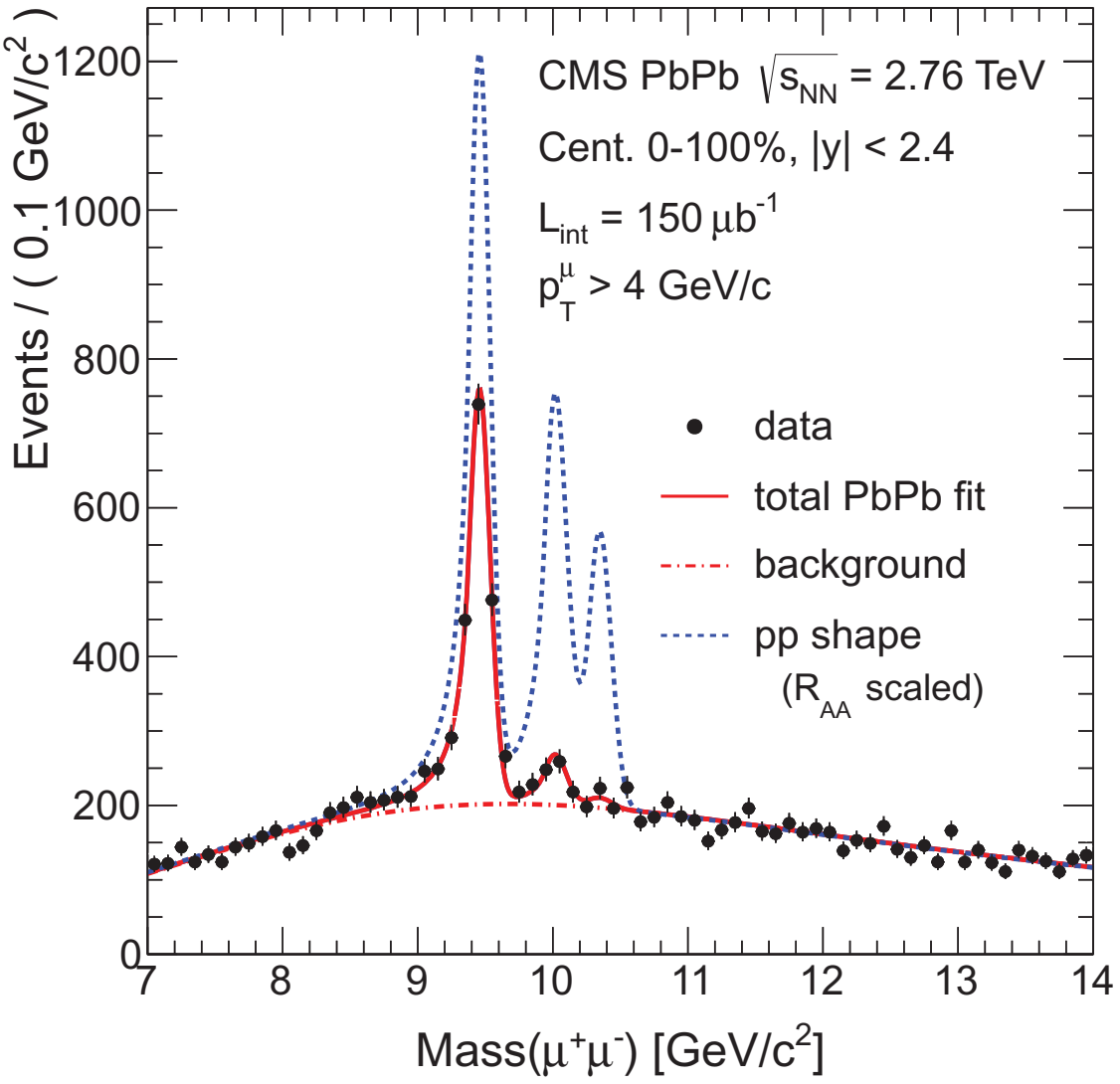

Figure 13.2: Dimuon invariant-mass distribution from the PbPb data, with the fit results shown in the solid (data + background) curves while the dot-dashed lines represents the background-only fit. The dashed curve illustrates the corresponding signals in *pp* data, scaled by the R_{AA} values. The same reconstruction algorithm and analysis criteria are applied to the PbPb and *pp* datasets, including single muon $p_{\mathrm{T}} > 4\,\mathrm{GeV}/c$ requirement.

Bibliography

[1] C. DeTar and U. M. Heller, Eur. Phys. J. A **41** (2009) 405, http://arxiv.org/abs/0905.2949arXiv:0905.2949 [hep-lat]

[2] Y. Aoki, Z. Fodor, S. D. Katz, and K. K. Szabo, Phys. Lett. B **643** (2006) 46, http://arxiv.org/abs/hep-lat/0609068arXiv:hep-lat/0609068

[3] M. Cheng *et al.*, Phys. Rev. D **77** (2008) 014511, http://arxiv.org/abs/0710.0354arXiv:0710.0354 [hep-lat]

[4] Y. Aoki, S. Borsanyi, S. Durr, Z. Fodor, S. D. Katz, S. Krieg, and K. K. Szabo, JHEP **0906** (2009) 088, http://arxiv.org/abs/0903.4155arXiv:0903.4155 [hep-lat]

[5] A. Bazavov *et al.*, Phys. Rev. D **80** (2009) 014504, http://arxiv.org/abs/0903.4379arXiv:0903.4379 [hep-lat]

[6] M. Cheng *et al.*, Phys. Rev. D **81** (2010) 054504, http://arxiv.org/abs/0911.2215arXiv:0911.2215 [hep-lat]

[7] A. Bazavov and P. Petreczky, PoS **LAT2009** (2009) 163, http://arxiv.org/abs/0912.5421arXiv:0912.5421 [hep-lat]

[8] A. Bazavov and P. Petreczky (HotQCD Collaboration), J. Phys. Conf. Ser. **230**, 012014 (2010), http://arxiv.org/abs/1005.1131arXiv:1005.1131 [hep-lat]

[9] A. Bazavov and P. Petreczky, http://arxiv.org/abs/1009.4914arXiv:1009.4914 [hep-lat]

[10] S. Borsanyi (Wuppertal-Budapest Collaboration), JHEP **1009**, 073 (2010), http://arxiv.org/abs/1005.3508arXiv:1005.3508 [hep-lat]

[11] S. Borsanyi *et al.*, JHEP **1011** (2010) 077, http://arxiv.org/abs/1007.2580arXiv:1007.2580 [hep-lat]

[12] T. Matsui and H. Satz. J/ψ suppression by quark-gluon plasma formation. *Phys. Lett.*, B178:416, 1986.

[13] P. Petreczky, J. Phys. G **37** (2010) 094009, http://arxiv.org/abs/1001.5284arXiv:1001.5284 [hep-ph]

[14] P. Petreczky, http://arxiv.org/abs/0906.0502arXiv:0906.0502 [nucl-th]

[15] A. Bazavov, P. Petreczky, and A. Velytsky, http://arxiv.org/abs/0904.1748arXiv:0904.1748 [hep-ph]

[16] P. Petreczky, Eur. Phys. J. C **43** (2005) 51, http://arxiv.org/abs/hep-lat/0502008arXiv:hep-lat/0502008

[17] O. Kaczmarek, F. Karsch, P. Petreczky, and F. Zantow, Phys. Lett. B **543**, 41 (2002), http://arxiv.org/abs/hep-lat/0207002arXiv:hep-lat/0207002

[18] S. Digal, S. Fortunato, and P. Petreczky, Phys. Rev. D **68**, 034008 (2003), http://arxiv.org/abs/hep-lat/0304017arXiv:hep-lat/0304017

[19] P. Petreczky and K. Petrov, Phys. Rev. D **70** (2004) 054503, http://arxiv.org/abs/hep-lat/0405009arXiv:hep-lat/0405009

[20] O. Kaczmarek and F. Zantow, Phys. Rev. D **71** (2005) 114510, http://arxiv.org/abs/hep-lat/0503017arXiv:hep-lat/0503017

[21] O. Kaczmarek, PoS C **POD07** (2007) 043, http://arxiv.org/abs/0710.0498arXiv:0710.0498 [hep-lat]

[22] P. Petreczky, J. Phys. G **37** (2010) 094009, http://arxiv.org/abs/1001.5284arXiv:1001.5284 [hep-ph]

[23] P. Faccioli, C. Lourenço, J. Seixas, and H. K. Woehri, JHEP **0810** (2008) 004, http://arxiv.org/abs/0809.2153arXiv:0809.2153 [hep-ph]

[24] R. Vogt, Nucl. Phys. A **700** (2002) 539, http://arxiv.org/abs/hep-ph/0107045arXiv:hep-ph/0107045

[25] K. J. Eskola, H. Paukkunen, and C. A. Salgado, JHEP **0904** (2009) 065, http://arxiv.org/abs/0902.4154arXiv:0902.4154 [hep-ph]

[26] A. D. Frawley, T. Ullrich, and R. Vogt, Phys. Rept. **462** (2008) 125, http://arxiv.org/abs/0806.1013arXiv:0806.1013 [nucl-ex]

[27] Á. Mócsy and P. Petreczky, Phys. Rev. D **77** (2008) 014501, http://arxiv.org/abs/0705.2559arXiv:0705.2559 [hep-ph]

[28] Á. Mócsy and P. Petreczky, Phys. Rev. Lett. **99** (2007) 211602, http://arxiv.org/abs/0706.2183arXiv:0706.2183 [hep-ph]

[29] A. Mocsy, Eur. Phys. J. C **61** (2009) 705, http://arxiv.org/abs/0811.0337arXiv:0811.0337 [hep-ph]

[30] Karsch F, Mehr M T and Satz H 1988 *Z. Phys.* **C37** 617

[31] Rakotozafindrabe A, Ferreiro E G, Fleuret F, Lansberg J P and Matagne N 2012 *PoS* **QNP2012** 159 (*Preprint*)

[32] Emerick A, Zhao X and Rapp R 2012 *Eur.Phys.J.* **A48** 72 (*Preprint*)

[33] Dumitru A, Guo Y and Strickland M 2009 *Phys.Rev.* **D79** 114003 (*Preprint*)

[34] Laine M, Philipsen O, Romatschke P and Tassler M 2007 *JHEP* **03** 054 (*Preprint*)

[35] A. Beraudo, J. -P. Blaizot and C. Ratti, Nucl. Phys. A **806**, 312 (2008) [arXiv:0712.4394 [nucl-th]].

[36] Brambilla N, Ghiglieri J, Vairo A and Petreczky P 2008 *Phys. Rev.* **D78** 014017 (*Preprint*)

[37] Upsilon suppression fitting results: background sculpting with p_{T}. Technical report, 2012.

[38] B. A.Berg. Introduction to Markov Chain Monte Carlo Simulations and their Statistical Analysis. *In Markov Chain Monte Carlo, W.S. Kendall et al. Editors, Lecture Notes Series, Institute for Mathematical Sciences, National University of Singapore, World Scientific*, 7:p.1 ff, 2005.

[39] S. Chatrchyan et al. Indications of suppression of excited Υ states in PbPb collisions at $\sqrt{S_{NN}} =$ 2.76 TeV. *Phys.Rev.Lett.*, 107:052302, 2011.

[40] CMS Collaboration. Quarkonium production in pbpb collisions. CMS Note CMS-PAS-HIN-10-006, 2011.

[41] CMS Collaboration. Quarkonium production in pbpb collisions. CMS Note AN 2011/062, 2011.

[42] T. Sjöstrand, S. Mrenna and P. Skands. PYTHIA 6.4 physics and manual. JHEP 026, 2006, hep-ph/0603175.

[43] HYDJET. I.P. Lokhtin, A.M. Snigirev Eur. Phys. J. C 46 (2006) 211.

[44] K. S. Cranmer. Kernel estimation in high-energy physics. *Comput.Phys.Commun.*, 136:198–207, 2001.

[45] Z. Hu. Bottomonium production measured in PbPb and pp collisions by CMS. *J.Phys.G:Nucl.Part.Phys.*, 38:124071, 2011.

[46] I. Shipsey, N. Leonardo et al (for the Upsilon team). Measurement of the inclusive upsilon production cross section in *pp* collisions at $\sqrt{s} = 7\,\text{TeV}$. CMS Note 2010/040, 2010.

[47] P. J. Neyman. Reprinted in *A Selection of Early Statistical Papers on J. Neyman* (University of California Press, Berkeley, 1967). *Trans. Royal Soc. London, Series A*, pages pp. 250–289. See in particular pp. 250–252, 261–268, 285–286, of the reprint. Unfortunately, the quantity which Neyman calls α is precisely what is called $(1 - -\alpha)$ in modern references. We use the adjectives "classical" and "frequentist" synonymously to refer to the theory of these confidence intervals., 1937.

[48] R. Rapp. Medium Modications and Production of Charmonia at LHC. *Nucl. Phys. A 859 (2011) 114, doi:10.1016/j.nuclphysa.2011.05.001.*

[49] A. Read. Presentation of search results: the CLs technique. *Journal of Physics G: Nucl. Part. Phys.*, 28, 2002.

[50] M. Strickland. Thermal Υ and χ_{b1} Suppression at $\sqrt{S_{NN}} = 2.76$ Pb-Pb Collisions at the LHC. *Phys.Rev.Lett.*, 107:132301, 2011.